Universidade de São Paulo
Instituto de Física

Transporte em nanoestruturas: fenômenos quânticos em poços duplos e triplos

Zahra Sadre Momtaz

Orientador: Prof. Dr. Gennady Gusev

Tese de doutorado apresentada ao Instituto de Física para a obtenção do título de Doutor em Ciências

Banca Examinadora:

Prof. Dr. Gennady Gusev (IFUSP) -Presidente
Prof. Dr. Valmir Antonio Chitta (IFUSP)
Prof. Dr. José Fernando Diniz Chubaci (IFUSP)
Profa. Dra. Ana Maria Melva C. Farfán (UFABC)
Prof. Dr. Marcelo Marques (ITA)

São Paulo
2016

FICHA CATALOGRÁFICA
Preparada pelo Serviço de Biblioteca e Informação do Instituto de Física da Universidade de São Paulo

Momtaz, Zahra Sadre

Transporte em nanoestruturas: fenômenos quânticos em poços duplos e triplos. São Paulo, 2016.

Tese (Doutorado) – Universidade de São Paulo. Instituto de Física. Depto. de Física dos Materiais e Mecânica

Orientador: Prof. Dr. Gennady Gusev

Área de Concentração: Transporte Quântico.

Unitermos: 1. Materiais nanoestruturados; 2. Sistemas multicamadas de elétrons; 3. Magnetotransporte; 4. Oscilações de resistência induzida por micro-ondas; 5. Estados de resistência zero; 6. Oscilações magneto-termoelétricas.

USP/IF/SBI-015/2016

dedicate to my love Behrouz

Acknowledgments

First and foremost I would like to thank Prof. Gennady Gusev for giving me the opportunity to work in his group. I thank him for creating a unique lab in which surprises never end. I thank him for teaching me the meaning of being an experimentalist! I admire him for his willingness to share and inspire with his unending enthusiasm for physics.

I wish to thank Prof. Alexander Levin, for all scientific discussions during the experiments in Laboratory of new semiconductor material of University of São Paulo. Thanks for sharing your time and knowledge to teach me how to be a good experimental physicist; I can say that I have benefited greatly from your advice. Also unforgettable were the times you were with me in clean room to show me the details of sample preparation step by step. Sasha, thank you so much for all!

The present work would not have been possible without a close collaboration to Oleg Raichev, theoretical physicist at Institute of Semiconductor Physics, NAS of Ukraine, due to a continuous exchange between experimental results, theoretical models and data analysis. Thank you very much Oleg for all these exchanges during my PhD. Your input enabled me to connect all experimental results to theory and I am sure that readers will benefit from it.

Also, I wish to thanks Askhat Bakarov from Institute of Semiconductor Physics in Novosibirsk Russia, for doing an excellent job in preparing high quality samples for us.

I am grateful to Prof. Antonio Seabra from Department of polytechnic of University of São Paulo for letting me work in his clean room and providing me all necessary materials to process the samples.

I am also very thankful to Ricardo Rangle for all his kind help and useful information provide me during working in clean room. I am also thankful for Dr. Mariana Pojar and Nelson Ordonez for their time and help during sample process in clean room.

I also wish to thank the referees of my PhD qualification exam Prof.Valmir Antonio Chitta and Prof. Felix Hernandez. I am also thankful to Prof.Alain Quivy for his time and his help during my PhD studies.

I also thankful to Dr. Steffen Wiedmann for his time and discussions during my PhD.

My special words of thanks should also go to my colleagues and friends during my PhD studies. Your presence make this environment more pleasant for me. Thanks you Diana, for your great heart. I also would like to thank my friends and colleague, Dr. Abdur-rahim, Fernando Aliaga, Natalia Ballaminut, Saeed, Reynaldo Santos, Maria Del valle.

I am also very thankful to Francisco de Paula Oliveira (Paulinho), the grandpa of our lab for preparing the lab for measurements. Thank you for all the days you be there early in the morning to prepare the system for our measurements.

My special regards to my teachers at different stages of education especially which makes it possible for me to see this day. It was because of their kindness that I have reached a stage where I could write this thesis.

I feel a deep sense of gratitude for my grand parents "Aghajoon", "Mamanjoon", "khanum kia" for all supports and love they have given me in whole my life. Love you for ever and I am very happy to have you to see me in this stage of my life. I also remind my grandpa "Hajibaba" with all good memories he left for me and although he is not among us I am sure that he would proud of me for what I have achieved.

My whole heart and love goes to my unique parents, Dr. Nasser Sadr Momtaz and Shahnaz Seraj for all love and support in every moments of my life no matter if were close or far. Their infallible love and support has always been my strength. Their patience and sacrifice will remain my inspiration throughout my life.

A love with special thanks to my younger brother Amir and our lovely bride, Elham for all the love and positive energy they bring to me these days with starting a new life together. I wish you all the best and happiness for your new born life together.

I am also very much grateful to all my family members, aunts and uncle for their constant

inspiration and encouragement.
My heart felt regard goes to my father in law, Rahim , mother in law, Fatemeh for their love and kindness to me. I am also thankful to my sister in laws and my brother in law for their love and moral support.
Last but not least, I dedicate this dissertation to my husband, Behrouz, the most special person in my life. Thank you for your love, support and understanding during my Ph.D.

Resumo

Nesta tese apresentamos os estudos de magnetotransporte em poços quânticos largos, estreitos e triplos das amostras de $GaAs$ em campos magnéticos baixos. Dependendo dos estudos desejados, me-
dimos a magnetoresistência em regime linear e não linear e sob a aplicação de corrente AC, irradiação de microondas e em gradiente de temperatura ao longo das amostras.

Relatamos a observação de efeitos não lineares de corrente alternada em oscilações magneto-inter-sub-bandas (MIS) de poços quânticos triplos. A oscilação MIS em sistemas de poços quânticos individuais e duplos e também os efeitos não lineares devido à corrente contínua foram estudados antes nestes sistemas. Nossos resultados são explicados de acordo com um modelo generalizado baseado na parte de não equilíbrio da função de distribuição de elétrons.

A magnetorresistência não local sob irradiação de microondas é também estudada nesta tese. Os resultados obtidos proporcionam evidências para uma corrente de estado de borda estabilizada por irradiação de microondas, devido às ressonâncias não lineares e foram descritas por um modelo baseado em dinâmica não linear e mapa padrão de Chirikov.

Finalmente, observamos uma correlação estreita entre as oscilações de resistência e oscilações de tensão de arraste do fônon induzidas por irradiação de microondas em um sistema bidimensional de eletrons sob campo magnético perpendicular. A influência da resistividade de dissipação modificada por microondas na tensão de arraste do fônon perpendicular ao fluxo de fônons pode explicar nossas observações. Além disso, características nítidas observadas na tensão de arraste do fônon sugerem que os domínios de corrente associados a estes estados podem existir na ausência de condução DC externa.

Palavra-chave: sistemas multicamadas de elétrons, magnetotransporte, oscilações de resistência induzida por microondas, estados de resistência zero, oscilações magnetotermelétricas.

Abstract

In this thesis, we present the studies of magneto-transport in narrow , wide and triple quantum wells of $GaAs$ samples in low magnetic fields. Depending on the desired studies, we have measured the magneto-resistance both in linear and nonlinear regimes and under the application of AC current, microwave irradiation and temperature gradient along the samples.

We have reported the observation of nonlinear effects of AC current on magneto-inter-subband oscillations (MIS) of triple quantum wells (TQWs). The MIS oscillations in single and double quantum well system and also nonlinear effects due to DC current have been studied before in these systems. Our results are explained according to a generalized model based on non-equilibrium part of electron distribution function.

The nonlocal magneto-resistance under microwave irradiation is also studied within this thesis. The obtained results provide evidence for an edge-state current stabilized by microwave irradiation due to nonlinear resonances and have been described by a model based on the nonlinear dynamics and Chirikov standard map.

Finally, we have observed the phonon-drag voltage oscillations correlating with the resistance oscillations under microwave irradiation in a two-dimensional electron gas in perpendicular magnetic field. The influence of dissipative resistivity modified by microwave on phonon-drag voltage perpendicular to the phonon flux can explain our observations. Moreover, sharp features observed in phonon drag voltage suggest the current domains associated with these states can exist in the absence of external DC driving.

Key words: multilayer electron systems, magneto-transport, microwave-induced resistance oscillations, zero-resistance states, magneto-thermopower oscillations.

Contents

List of Figures

List of Tables

Chapter 1

What is this thesis about?

SEMICONDUCTOR technology forms the basis of microelectronic devices and information technology. Among these materials low-dimensional electronic systems, in which one or more spatial dimensions are small enough to restrict the quantum mechanical wave function of electrons contained inside, exhibit some of the most diverse and intriguing physical phenomena seen in all of condensed matter physics. The development of growth techniques like Molecular Beam Epitaxy (MBE) enabled scientists, to create and define low-dimensional structures in semiconductor materials.

Low dimensional systems of multilayer electrons are of particular interests. Due to additional degree of freedom provided by inter-layer tunnel coupling, they allow the observation of interesting phenomena which are absent in conventional single layer 2D electron systems. Effects like electron tunneling and electron correlations in different layers are important in these systems. Progress in modern semiconductor growth makes the fabrication of high quality multiple 2D layers possible.

The research studies are carried out on materials based on Gallium Arsenide ($GaAs$) sandwiched by Aluminum Gallium Arsenide ($AlGaAs$) forming a quantum well structure, which is one possible realization of a 2D electron system. Multilayer systems are formed by separating the quantum wells by Aluminum Gallium Arsenide ($Al_xGa_{1-x}As$) barriers. The thickness of the barrier and also Al concentration strongly alter the electron coupling between different layers.

The objective of this thesis is to obtain new fundamental knowledge of the influence of quantum degree of freedom produced by tunnel coupling in magneto transport phenomena.

In this way, we have carried out studies on quantum transport phenomena including measurements of new oscillations like magneto inter sub-band resonance oscillations and magneto phonon oscillations due to interaction of electrons with acoustic phonons in bilayer and trilayer electron systems of $GaAs$.

It is known that the longitudinal resistance of a sufficiently high mobility 2D electron system in low magnetic fields and under microwave irradiation exhibit giant oscillations termed Microwave Induced Resistance Oscillations (MIRO) (Zudov et al., 1997, 2001). Moreover, experiments by Mani et al. (2002) and Zudov et al. (2003) revealed that the lower order minima of MIROs extend all the way to zero and forming Zero Resistance States (ZRS), whereas the transverse Hall resistance remains essentially unaffected. Occurrence of zero resistance is rare in condensed-matter physics and usually associate to a novel state of matter such as superconductivity (Kamerlingh Onnes, 1911a,b) and Quantum Hall effect (Klitzing, Dorda and Pepper, 1980; Tsui et al. , 1982). ZRS can span ranges corresponding to several tens in magnetic field depending on the radiation intensity, temperature and quality of samples.

This phenomena, which has attracted much theoretical interest, is assumed to be related to the bulk properties of a 2D electron systems and several microscopic mechanisms are presented. Displacement mechanism proposed by Ryzhii (Ryzhii, 1970; Ryzhii et al., 1986; Durst et al., 2003) and inelastic mechanism (Dorozhkin, 2003; Dmitriev et al., 2005) are the dominant ones widely discussed in literature.

In scientific community, there is a controversy on the origin of microwave induced phenomena and ZRS that if these phenomena are related to the bulk like (Ryzhii, 1970; Ryzhii et al., 1986; Durst et al., 2003; Dorozhkin, 2003; Dmitriev et al., 2005) or near contact effects (Mikhailov and Savostianova , 2006; Andreev, 2008) . Within the framework of this thesis, we will demonstrate that MIRO and ZRS result from a combination of both bulk and edge-state contributions. We have also suggested the observation of thermo-induced voltage proportional to the resistance when a temperature gradient exists along the sample and demonstrate that these oscillations closely resemble a MIRO signal.

The main idea of Chapter one is to provide fundamentals of a 2D electron system and basic properties of magneto-transport in bilayer electron system. Bilayer electron systems can be formed by either two quantum wells separated by a narrow barrier or high-density wide single quantum wells owing to charge redistribution, where the two wells near the interface are separated by an electrostatic potential barrier. Hence, two sub-bands appear due to tunnel coupling of 2D electron states. The magneto-resistance in a bilayer system exhibits magneto-intersubband oscillations due to the alignment of Landau levels from both wells at the Fermi level with increasing perpendicular magnetic field (Mamani et al., 2008).

Chapter 3 introduces basics of sample preparation and the cryogenic systems which have been used during this thesis. Moreover, detailed information about the experimental methods for microwave experiments are also provided.

The experimental results of magneto-resistance in bilayer and trilayer electron systems are presented in Chapters 4- 6. Owing to a close and successful collaboration with Oleg Raichev, theoretical physicist from the Institute of Semiconductor Physics in Kiev (NAS of Ukraine), during this project, we were able to analyze and discuss the obtained experimental results within a theoretical framework.

The nonlocal response of two dimensional electron system to microwave excitation is the topic of Chapter 5. Our measurements provide evidence for microwave induced edge-state transport in the low magnetic field regime and imply that the dissipationless edge-state transport persists over macroscopic distances. We will show that the observed effect can be understood within a common framework based on modern nonlinear dynamics through a nonlinear resonance well described by the standard map, known as the Chirikov standard map (Chirikov, 1979).

Although there are lots of attention to the MIRO and ZRS phenomena, most of the experimental studies are based on the measurements of electrical resistance or conductance under DC driving. In Chapter 6, we suggest for the first time the MW-induced magneto-oscillations of the phonon-drag voltage in GaAs quantum wells, correlating with the behavior of electrical resistance. The effect is described according to a theory developed by Prof. Raichev, in terms of the sensitivity of transverse drag voltage to the dissipative resistivity modified by microwaves zero resistance regime which can be viewed as a signature of current domain states. We also believe that Such MW-induced thermo-electric phenomena may show up in other 2D systems.

Finally, the conclusions and outlook of this thesis is presented in Chapter 7.

Chapter 2

Fundamental concepts of magneto-transport in 2D electron gases

Contents

DURING the last decades two dimensional electron systems at low temperature and in the presence of magnetic field have been studied extensively and significant effects like Integer quantum hall effect (IQHE) (Klitzing, Dorda and Pepper, 1980) and Fractional quantum hall effect (FQHE) (Tsui et al., 1983) have been discovered in these systems. Physics of 2D electron systems in the presence of applied perpendicular magnetic field becomes interesting when the electron motion is quantized and the energy levels become discrete. The quantization in energy manifests itself in magneto-resistance measurements with quantized Hall resistance accompanied by oscillations in longitudinal resistance.

Beyond pure 2D electron systems, where electron motion occurs in a single layer, bilayer and trilayer electron systems formed in double (DQW) and triple (TQW) quantum wells or high electron density wide quantum wells (WQW) are of great interest. The quantum mechanical penetration of electron wave-functions through the thin barriers in these systems, lead them to be viewed as two or three 2D electron layers coupled by tunneling. Due to the existence of this extra degree of freedom, magneto-resistance oscillations of double and triple quantum wells exhibit additional oscillations beyond Shubnikov de Haas oscillations. These oscillations in magneto-resistance, called Magneto Inter-subband oscillations (MIS), play an important role in description of non-linearity in magneto-resistance and photo-resistance of these systems.

This chapter provides a general introduction to all basic concepts in two dimensional electron systems and their transport properties necessary for better understanding of the measurements carried out in this thesis. First of all two dimensional electron systems and transport properties are described following with a brief introduction to multi-layer electron systems and the extra features in magneto-resistance of these systems.

Transport measurements in the presence of microwave irradiation and related concepts are also provided in this chapter. Finally basics of thermo-electric power measurement and magneto-phonon oscillations in two dimensional electron systems are discussed.

2.1 What we want to know

- How 2D electron gas can be formed in $GaAs/Al_xGa_{1-x}As$ heterostructures and what are its basic properties?
- What are the properties of magneto-transport in two dimensional electron systems at low temperatures and perpendicular magnetic field?
- How does the magneto-transport behave for bilayer systems? What are the additional features comparing to single layer electron systems?
- What are microwave induced oscillations and related phenomena? What are the relevant mechanisms describing them?
- How can the electron-phonon interactions be described in 2D electron systems and what are the relevant formalisms?

2.2 Fundamentals of 2D electron gases in $GaAs/Al_xGa_{1-x}As$

Depending on the number of geometric confined dimensions, semiconductor materials are termed quantum wells (QWs), quantum wires (QWRs) and quantum dots (QDs), for 1D, 2D and 3D quantum confinement, respectively. Effect of quantum confinement on electronic and optical properties of semiconductors becomes important when the de Broglie wavelength of electron or holes is comparable to the physical size of confining potential. Considering the thermal motion of a particle of mass m along a single direction in a crystal with lattice temperature T, then the de Broglie wavelength is given by

$$\lambda_{deB} = \frac{h}{\sqrt{mk_B T}}, \tag{2.1}$$

with k_B and h the Boltzmann and Planck constant respectively (Fox, 2010). In case of $GaAs$ at room temperature (T=300 K), electron de Broglie wavelength is $\lambda_{deB} = 42\ nm$. Hence, quantum size effects will be important for nano-structures with spatial dimensions of tens nm (achievable by epitaxy techniques) in the range of room temperature to liquid helium temperatures.

One dimensional spatial confinement creates the two dimensional electron gas which can be viewed as a type of metal in which electrons are confined to move within a two dimensional plane at the interface between two semiconductors. The motion of electrons along the confinement direction will be quantized and provides a series of discrete energy levels. The first observation of two dimensional electron gas at semiconductor- semiconductor interface was done by Stormer et al. (1979) at Bell laboratories where the GaAs/AlGaAs was grown by molecular beam epitaxy (MBE) on an insulating (Cr-doped) $< 100 > -GaAs$ substrate (Stormer et al., 1979).
Two dimensional electron gas in real samples is located in the inversion layer formed at the interface between semiconductor-insulator as in Si-MOSFET or at the semiconductor-semiconductor interface like the $GaAs/AlGaAs$ heterostructures. The inversion layer reverse the usual order of conduction and valence band and forms when the bottom of conduction band is below the top of the valence band. Since the width of this layer is smaller than the de Broglie wavelength, the motion along growth direction is quantized and the 2DEG is formed in this layer(Fig. 2.1).

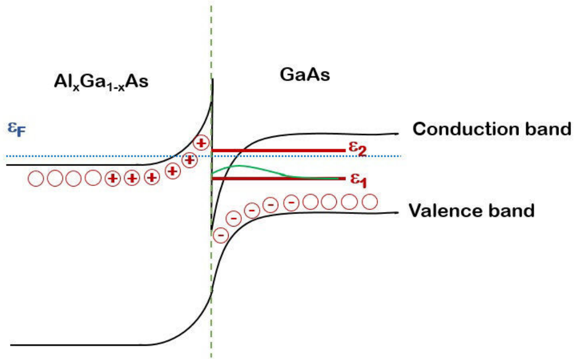

Figure 2.1: Schematic of formation of inversion layer in $GaAs/AlGaAs$ heterostructure

The two dimensional electron systems in $GaAs/AlGaAs$ interface due to near-perfect crystalline layers of extreme purity with nearly atomically sharp transitions between layers, provide very fruitful system for studying quantum mechanical effects such as Integer (IQHE) and Fractional quantum Hall (FQHE) effects. In Fig. 2.2, a $GaAs/AlGaAs$ hetero-structure and its effective electrostatic potential for electrons in the conduction band is schematically depicted. The z axis with its origin at $GaAs/AlGaAs$ interface, is chosen normal to the interface and along the direction of the growth of the structure. The metal gate which is deposited on top of the $GaAs$ cap layer, is not shown in the figure.

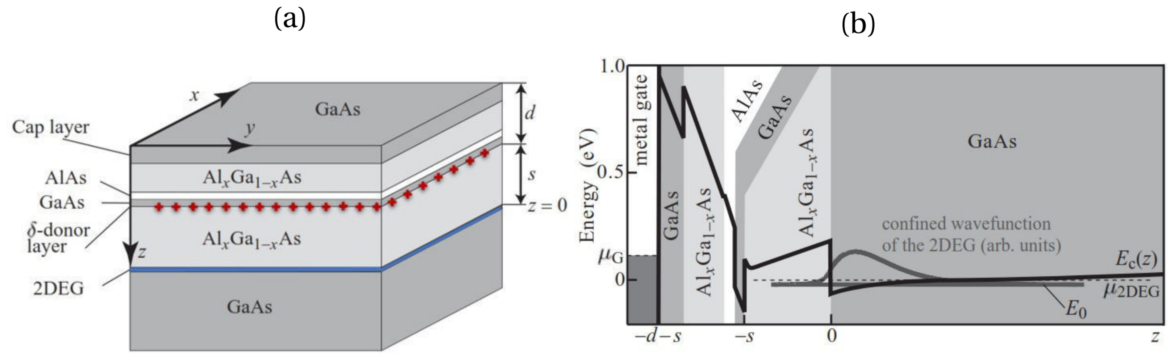

Figure 2.2: (a) Layer sequence in a typical $GaAs/AlGaAs$ hetero-structure with remote doping, (b) Effective potential for electrons in the conduction band in a typical $GaAs/AlGaAs$ hetero-structure with remote doping (Figure adapted from (Ihn, 2010))

Considering electrostatics within the jellium model, the effective potential for electrons in conduction band in the hetero-structure can be achieved. For simplicity the relative dielectric constants of $GaAs$ and $AlGaAs$ is assumed to be identical which is a reasonable assumption.

For $z \gg 0$ the conduction band is flat since there is no electric field in the sample. We can find electric field in the spacer layer ($Al_xGa_{1-x}As$) by applying Gauss's law and using a cylindrical closed surface with one end face in the $z \gg 0$ and the other end in the $-s < z < 0$.

Then, for electric field in spacer layer we have:

$$E = |e| n_s / \varepsilon \varepsilon_0, \tag{2.2}$$

where in this relation e , n_s, ε and ε_0 are electron charge, surface density of electrons , relative permittivity of spacer layer and vacuum permittivity, respectively. The equivalent electrostatic potential in the region $-s < z < 0$ is

$$\phi(z) = -\frac{|e| n_s}{\varepsilon \varepsilon_0} z, \tag{2.3}$$

By applying the same method we can find the electric field in the δ- doping layer

$$E = |e|(n_s - N_d) / \varepsilon \varepsilon_0, \tag{2.4}$$

and its corresponding potential for $-s - d < z < -s$

$$\phi(z) = \frac{|e| n_s}{\varepsilon \varepsilon_0} s - \frac{|e|(n_s - N_d)}{\varepsilon \varepsilon_0} (z + s), \tag{2.5}$$

at the semiconductor/metal interface the potential is given by

$$\phi(-s - d) = \frac{|e| n_s}{\varepsilon \varepsilon_0} s + \frac{|e|(n_s - N_d)}{\varepsilon \varepsilon_0} d, \tag{2.6}$$

where in the preceding expressions, N_d is the doping density and s and d are as shown in the Fig. 2.2(b).

From Eqs. 2.2 to 2.6, one can find the effective potential energy for electrons in conduction band exploiting $E_c(z) = -|e|\phi(z)$ and get the energy profile of the Fig. 2.2(b). Note that here, it is considered $E_c(z) = 0$ in $GaAs$ and the conduction band offset $\triangle E_c$ in $AlGaAs$.

Basic properties of 2DEG

In 2DEGs the electrons along the direction of growth are confined while they can move freely in two other directions. If we consider the direction of growth along z then in $x-y$ plane electrons move freely. Considering single electron picture, the *Schrödinger* equation can be written as

$$[-\frac{\hbar^2}{2m^*}\nabla^2 + V(z)]\psi(x,y,z) = E\psi(x,y,z), \tag{2.7}$$

where m^* is the electron effective mass in conduction band (for $GaAs/Al_xGa_{1-x}As, m^* = 0.067m_e$), $V(z)$ is the confining potential along z direction and $\psi(x,y,z)$ is the electron wave function.

Since the bounding potential depends on the z direction, the electron states along z direction are quantized while they have free motion in $x-y$ plane. Separating the *Schrödinger* equation, the ansatz could be made for electron wave function , $\psi(x,y,z) = \phi_n(z)\ exp[ik_xx + ik_yy]$ and then the electron total energy is given by

$$E_n(k_x,k_y) = \varepsilon_n + \frac{\hbar^2}{2m^*}(k_x^2 + k_y^2),\ n = 0,1,2,3,... \tag{2.8}$$

where ε_n is the energy along the direction of confinement ($n = 0$ is the lowest sub-band) and k_i is the electron wave vector along i direction. As it is clear from Eq. 2.8 the total energy consists of parabolas along x and y direction which are separated by the quantized energy, ε_n.

For a given n, each of these parabola are called a sub-band and the lowest sub-bands are given for $\vec{k} = 0$ in which $E_n(k_x = 0, k_y = 0) = \varepsilon_n$. At low temperatures when $k_BT \ll \triangle\varepsilon$, all electron will be confined to the lowest sub-band ε_0.

The integrated density of states for energies lower than E is given by

$$N(E) = \frac{g_sg_v}{A}\sum_{k,E_n(k)<E} 1 = \frac{g_sg_v}{(2\pi)^2}\int d^2k = \frac{g_sg_vm*}{\pi\hbar^2}\int_0^E dE' = \frac{g_sg_vm*}{\pi\hbar^2}E, \tag{2.9}$$

The density of states is therefore

$$D(E) = \frac{dN(E)}{dE} = \frac{g_s g_v m*}{2\pi\hbar^2}, \tag{2.10}$$

where g_s and g_v spin and valley degeneracy respectively. For $GaAs$, $g_s = 2$ and $g_v = 1$. As we can see the density of states is constant for each sub-band for 2D systems.

If several sub-bands are taken into account, then the total density of states would be a number of steps which is given by

$$D(E) = \frac{g_s g_v m*}{2\pi\hbar^2} \sum_n \Theta(E - \varepsilon_n), \tag{2.11}$$

where Θ is the Heaviside step function.

The density of states determines the available energy levels of the system. The next step is to make these levels filled up with electrons. In equilibrium, the average number of electrons that occupy a state depends on the energy of that state and also the occupation function. For electrons this occupation function is Fermi-Dirac distribution function that in thermodynamic equilibrium is expressed as

$$f(E) = \frac{1}{\exp(\frac{E-\mu_f(T)}{k_B T}) + 1}, \tag{2.12}$$

where k_B is the Boltzmann constant and μ_f is the chemical potential of the system that varies with the temperature, T. The chemical potential at zero temperature is called the Fermi energy, ε_F.

At $T = 0$ and according to Pauli exclusion principle, $f(E)$ takes values between zero and one and it can be interpreted as the probability that an state with energy E be occupied by an electron at temperature T. This implies that, at $T = 0$, where $f(E) = \Theta(\varepsilon_F^0 - E)$, the probability of finding electron with $E < \varepsilon_F$, is one and there is no electron in $E > \varepsilon_F$. For $T \neq 0$, electrons can occupy states with $E > \varepsilon_F$, and these are the electrons that are responsible for the transport properties.

The electron density is then given by

$$n_s = \int_{-\infty}^{+\infty} D(E) f(E) dE, \tag{2.13}$$

For 2DEG with $D(E) = \frac{m^*}{\pi\hbar^2}$, it would be

$$n_s = \frac{m^* k_B T}{\pi\hbar^2} \ln(1 + \exp(\frac{\varepsilon_F}{k_B T})), \tag{2.14}$$

and for constant density of states the Fermi energy can be expressed as:

$$\varepsilon_f = \frac{\pi\hbar^2}{m*} n_s, \tag{2.15}$$

2.2.1 Two dimensional electron gas (2DEG) in a perpendicular magnetic field

In a uniform magnetic field , classical electrons form confined circular orbits in the plane perpendicular to the magnetic field, with constant angular frequency $\omega_c = \frac{eB}{m^*}$ known as cyclotron frequency. Accordingly, eigenstates of electrons in a uniform magnetic filed are localized in transverse plane and are labeled by two quantum numbers. These quantum states and corresponding energy levels, which are referred to as Landau states and Landau levels, were described by Fock 1928, Landau 1930 and Darwin 1931 in the early days of quantum theory.

Landau eigenstates play an important role in different solid-state phenomena, such as quantum Hall effect, Shubnikov de Haas and De Haas–van Alphen effects (Kittel, 1987; Marder, 2010; Yoshioka, 2002). In quantum Hall effect these levels reveal themselves as plateaus in conductance.

The Hamiltonian of a charged particle in an external magnetic field is described by

$$\mathscr{H} = \frac{1}{2m^*}(\overrightarrow{P} - \frac{e}{c}\overrightarrow{A})^2, \tag{2.16}$$

in which $\overrightarrow{A}$ is a vector potential such that $\vec{B} = \overrightarrow{\nabla} \times \overrightarrow{A}$ and $\overrightarrow{P}$ represents generalized momentum given by $\overrightarrow{P} = -i\hbar\overrightarrow{\nabla}$. The spin of the particle is ignored here.

The *Schrödinger* equation then can be written as

$$[\frac{1}{2m^*}(\overrightarrow{P} - \frac{e}{c}\overrightarrow{A})^2 + V(z)]\Psi(x, y, z) = E\Psi(x, y, z) \tag{2.17}$$

Considering the magnetic field in z direction, $\overrightarrow{B} = B_0\hat{z}$, the electron motion would be in $x - y$ plane. Using Landau gauge the vector potential can be written as $\overrightarrow{A} = -yB_0\hat{x}$, so the electron moves freely along x direction and has harmonic oscillating motion along y direction. Note that in equation 2.17, $V(z)$ is the potential of the 2DEG perpendicular to the boundary layer in the direction of growth of the structure (e.g., heterostructures , quantum wells, etc.). The total energy of the system is then expressed as

$$E_{i,n} = \varepsilon_i + (n + \frac{1}{2})\hbar\omega_c, \ i, n = 0, 1, 2, ... \tag{2.18}$$

and the density of states, DOS, in $x - y$ plane obeys additional quantization, results in a series of δ like energy levels for an ideal system, in which electron scattering due to other electrons , impurities , phonons and suchlike are ignored. It is given by

$$D(E) = \frac{g_s}{2\pi l_B^2}\sum_{i,n}\delta(E - E_{i,n}), \ i, n = 0, 1, 2, ... \tag{2.19}$$

where δ is Delta Dirac function, ε_i is sub-band energy and $(n + \frac{1}{2})\hbar\omega_c$ is Landau level energy, with i and n, respectively, sub-band level and Landau quantum number. In more realistic way, one should assume that electron can survive only for a finite time τ_q between scattering events. Consequently, Landau levels get the width Γ, which is $\Gamma = \frac{\hbar}{\tau_q}$ and can be defined precisely as the standard deviation or full width at half maximum (FWHM). One must keep in mind that τ_q is the quantum lifetime or single particle lifetime of electron and is different from the transport lifetime, τ_{tr} , which appears in the mobility and will discuss later. Gaussian or Lorentzian profiles are assumed as the precise shape of Landau levels, however the precise shape of Landau levels are still eristic . When separation of Landau levels, $\hbar\omega_c$ exceeds their width Γ ($\hbar\omega_c > \Gamma$ or equivalent $\omega_c\tau_q > 1$), strong changes in density of states (DOS) would be expected, otherwise one would not expect to see strong changes in DOS.

The magnetic length $l_B = \sqrt{\frac{\hbar}{eB}}$ represents the characteristic length scale of the cyclotron motion at a given magnetic field and is independent of material parameters. At $B = 1$ T, $l_B \approx 26$ nm.

The wave functions of electron motion in $x - y$ plane is

$$\varphi_{n,k}(x,y) \propto H_{n-1}(\frac{y-y_k}{l_B})\exp(-\frac{(y-y_k)^2}{2l_B^2})\exp(ik_x x),\;\; n = 1,2,3,... \tag{2.20}$$

with $y_k = -\frac{\hbar k_x}{eB}$, the centers of wave functions.

The degeneracy of a Landau level which is defined as the allowed number of states in each Landau level per unit area, can be calculated as the number of flux quanta per unit area:

$$n_L = \frac{eB}{h} = \frac{1}{2\pi l_B^2}, \tag{2.21}$$

and the filling factor which is defined as the number of fully occupied Landau levels is given by the ratio of total electron density to the degeneracy of Landau levels:

$$\nu = \frac{n_s}{n_L} = \frac{hn_s}{eB}. \tag{2.22}$$

The occupation of Landau levels in a magnetic field for different values of field is shown in Fig. 2.3. As the magnetic field changes the Fermi level moves to maintain a constant density of electrons.

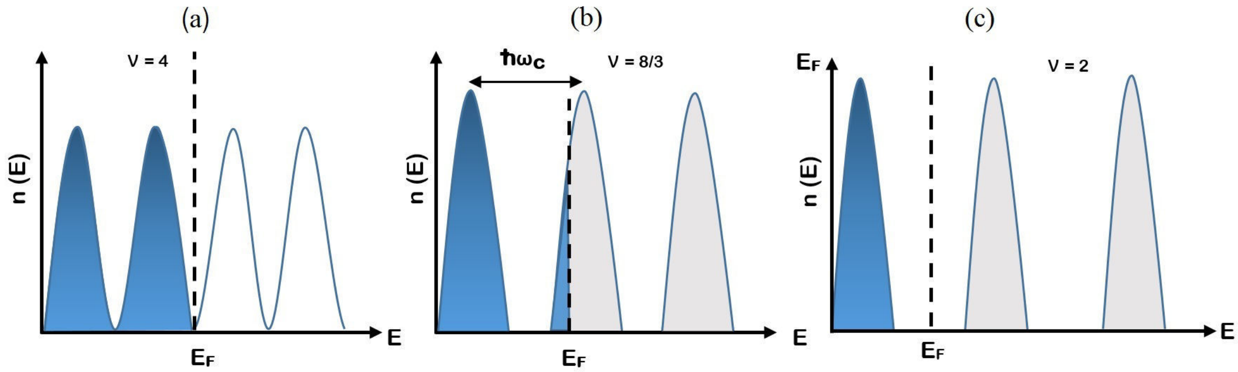

Figure 2.3: Occupation of Landau levels in a magnetic field for different value of applied magnetic field. The field are in the ratio of 2:3:4 for (a) to (c) respectively (Figure adapted from (Davies, 1998))

2.3 Magneto-transport theories in two dimensional electron systems

2.3.1 Classical approach: Drude model

Charge transport in 2D electron systems can be described by Drude model (Drude, 1900) in which electrons are considered as classical particles. It provides a simple way to describe transport through such systems and is valid for small magnetic fields, $\omega_c\tau \ll 1$ where electrons can not complete cyclotron orbits without being scattered and Landau levels are overlapped. At higher magnetic fields, this model will break down and one must consider quantum mechanics to properly describe transport in 2D electron systems.

The motion of electrons in an external electric and magnetic field is described according to

$$m^* \frac{d\vec{v_D}}{dt} + m^* \frac{\vec{v_D}}{\tau_{tr}} = e(\vec{E} + \vec{v_D} \times \vec{B}), \tag{2.23}$$

with $\vec{v_D}$, the drift velocity of electrons, τ_{tr} transport relaxation time which describes the time an electron can move without being scattered in a certain direction and it does not depend on magnetic field.

It is different from elastic scattering time which will be introduced later and describes the time an electron can move without changes in its energy. During transport relaxation time of τ_{tr}, electrons move with Fermi velocity v_F that gives the mean free path of electronic system with density of n_s as:

$$\ell = \tau_{tr} v_F = \frac{\hbar\mu}{e}\sqrt{2\pi n_s}, \tag{2.24}$$

Considering Eq. 2.23 in static case, the drift velocity is given by:

$$\vec{v_D} = \frac{e\tau_{tr}\vec{E}}{m^*} = \mu\vec{E}, \tag{2.25}$$

where $\mu = \frac{e\tau_{tr}}{m^*}$ defines the mobility of the electronic system that is a representative of the purity of the system. Moreover, the current density of the system, considering ohmic law would be $\vec{j} = en_s\vec{v_D}$. The Current density, $\vec{j}$, and driving electric field, $\vec{E}$, in linear regime are connected with the conductivity tensor $\overleftrightarrow{\sigma}$ as follows:

$$\vec{j} = \overleftrightarrow{\sigma}\vec{E}, \tag{2.26}$$

which in 2D systems leads to:

$$\begin{pmatrix} j_x \\ j_y \end{pmatrix} = \begin{pmatrix} \sigma_{xx} & \sigma_{xy} \\ \sigma_{yx} & \sigma_{yy} \end{pmatrix} \begin{pmatrix} E_x \\ E_y \end{pmatrix}, \tag{2.27}$$

For isotropic systems, the components of conductivity tensor are symmetric, so that $\sigma_{xx} = \sigma_{yy}$ and $\sigma_{xy} = -\sigma_{yx}$ and $\overleftrightarrow{\sigma} = \overleftrightarrow{\rho}^{-1}$. The components of resistivity tensor, thus, are given by:

$$\begin{aligned} \rho_{xx} &= \frac{\sigma_{xx}}{\sigma_{xx}^2 + \sigma_{xy}^2} = \frac{1}{en_s\mu}, \\ \rho_{xy} &= \frac{\sigma_{xy}}{\sigma_{xx}^2 + \sigma_{xy}^2} = \frac{1}{en_s}B, \end{aligned} \tag{2.28}$$

If one does measurements on a Hall bar structure similar to what is shown in Fig. 2.4 with width of W and length of L, then the preceding formulas must be written as:

$$\begin{aligned} \rho_{xx} &= R_{xx}\frac{W}{L}, \\ \rho_{xy} &= R_{xy}. \end{aligned} \tag{2.29}$$

In Van der Pauw geometry, the longitudinal resistance must be multiplied by $\frac{\pi}{\ln 2} = 4.5$, because in this case it is given by

$$\rho_{xx} = \frac{\pi}{\ln 2} R_{xx}\frac{W}{L}, \tag{2.30}$$

while transverse resistance is $\rho_{xy} = R_{xy}$.

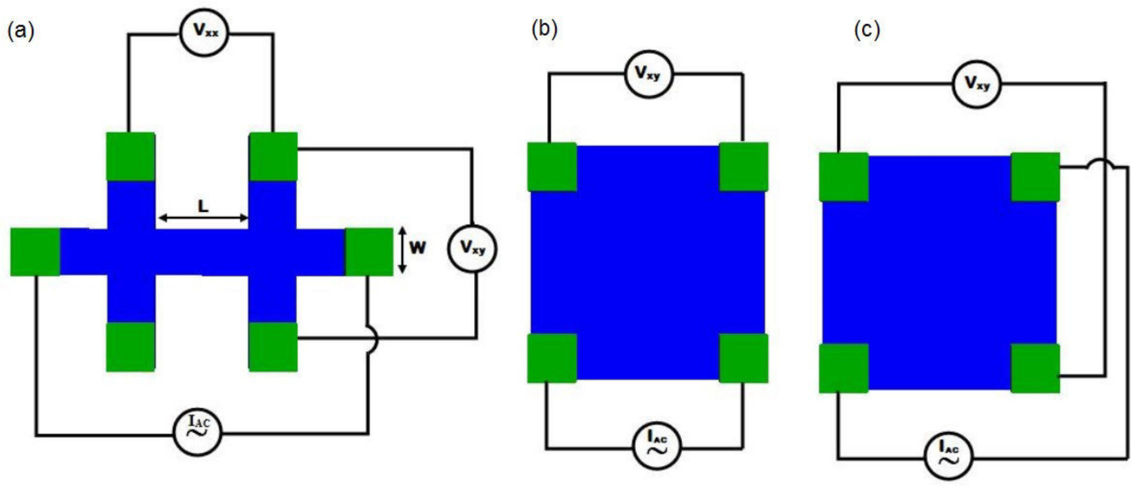

Figure 2.4: Schematic picture of a) Longitudinal and Hall resistance measurements in a Hall bar geometry, b) Longitudinal resistance and c) Transverse resistance in Van der Pauw geometry.

2.3.2 Quasi classical approach: Boltzmann transport theory

To understand transport properties in electronic systems containing scattering centers, Boltzmann equation can be used to describe the dynamic of the system by considering a balance between acceleration due to Lorentz force and deceleration owing to collision with the scattering centers.

In equilibrium states when there is no electric or magnetic fields, electron distribution in the system is given by Fermi- Dirac distribution function:

$$f^0(k) \;=\; \frac{1}{1+\exp(\frac{\epsilon_k-\mu}{k_B T})}. \tag{2.31}$$

In this case, since there is no net momentum, the net current is zero.

Switching on the electric and magnetic fields, electrons in k states accelerate by Lorentz force:

$$\frac{d\vec{v}_k}{dt} \;=\; \frac{\hbar dk}{m^* dt} = -\frac{e}{m^*}(\vec{E}+\vec{v_k}\times\vec{B}), \tag{2.32}$$

and this cause an evolution in distribution function of electrons in time so that $f \to f(\vec{r},\vec{k},t)$, which implies that:

$$f(r,k,t) = f(r+dr, k+\dot{k}dt, t+dt). \tag{2.33}$$

Since there are compensating factors like scattering from impurities at low temperatures, phonon scattering at higher temperatures and electron-electron collisions in the system versus accelerating forces, we can assume changes in f as a small perturbation on f^0 and that the application of small electric and magnetic fields will not shifted the spectrum of 2D system significantly. Furthermore, we would expect that if we turn the fields off, the excess distribution, $f(k,t)-f^0$ decay away through collision process during τ_k relaxation time. The last assumption, called Relaxation Time Approximation (RTA), is a good approximation for isotropic and elastic scattering at low fields.

Taylor expansion of Eq. 2.33 and considering assumptions above, the nonlinear Boltzmann equation can be written as:

$$\nabla_k(g+f^0).\frac{e}{\hbar}(\vec{E}+\vec{v_k}\times\vec{B}) = \frac{g}{\tau_k}, \tag{2.34}$$

with $g(k,t) = f^0(k,t) - f(k)$ refer to excess distribution of the electronic system.

The linear Boltzmann equation then would be:

$$\nabla_k g.\frac{e}{\hbar}(\vec{v}_k \times \vec{B}) + \nabla_k f^0.\frac{e}{\hbar}\vec{E} = \frac{g}{\tau_k}, \tag{2.35}$$

which is valid for small excess distribution. In case of zero magnetic field $g = \nabla_k f^0.\frac{e\tau_k}{\hbar}\vec{E}$ and the current density and conductivity tensor thus would be:

$$j = \frac{2e^2}{2\pi^2}\int d^2k(-\frac{\partial f^0}{\partial \epsilon})\tau v_k(v_k.E), \tag{2.36}$$

and

$$\sigma = \frac{2e^2}{2\pi^2}\int d^2k(-\frac{\partial f^0}{\partial \epsilon})\tau v_k \otimes v_k, \tag{2.37}$$

where $\otimes$ represents the outer product of two vectors and in 2D , $v_k \otimes v_k$ is a 2×2 matrix.

From Eqs. 2.36 and 2.37, it is clear that although all electrons have the same drift velocity but only electrons near the Fermi surface are contributed to the conductivity.

2.3.3 Shubnikov de Haas oscillations (SdH)

The Shubnikov de Haas oscillations which were discovered by Shubnikov and de Haas (1930) are oscillations of the longitudinal magneto-resistance in a quantizing magnetic field due to modulation of the DOS. These oscillations are periodic in $1/B$ and make the determination of the properties of a 2D system like period, effective mass, Dingle Temperature T_D , shape of the Fermi surface and the electronic energy spectrum possible. Hence, it is a premium technique to study 2D systems. The occurrence of these oscillations can be explained as follows.

The electrons in the bulk regions of 2DEG perform circular motion caused by applying perpendicular magnetic field, while they can not do full circular motion in the border region

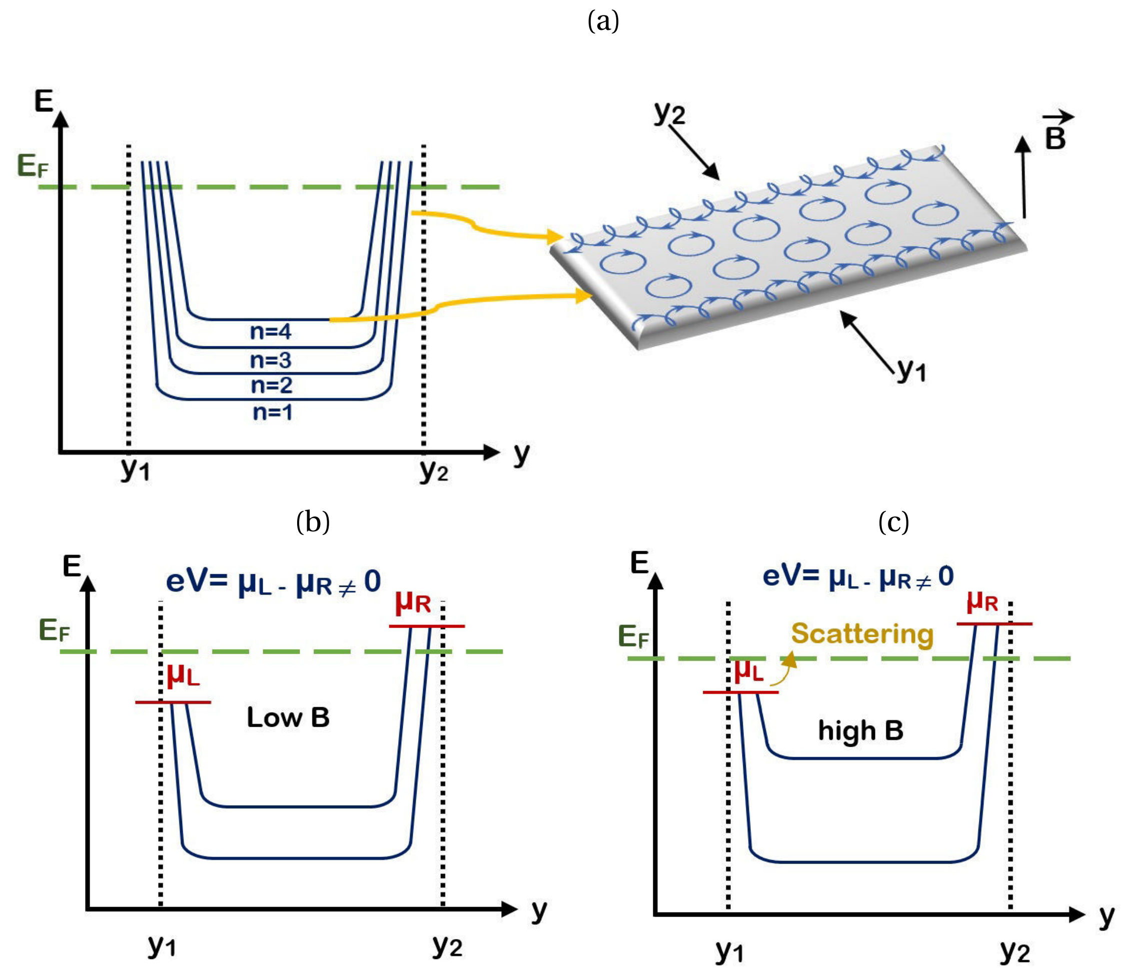

Figure 2.5: a) The resulting Landau-levels after applying a magnetic field, b) highest Landau-level far away from Fermi-energy (no scattering), c) highest Landau-level near the Fermi-energy (with scattering).

due to back-scattering processes from interfaces. The back-scattering events promote the energy of electrons. As discussed before the gap between two landau level is $\propto \hbar\omega_c$, therefore increasing the magnetic field makes the gap bigger. When the highest Landau level is far from Fermi energy, there is no states available for electrons to scatter in and the longitudinal resistivity would be zero while the transverse one will remain constant . The peaks of oscillations appear when there are available states for scattering in the bulk regime. This scenario is shown for different applied magnetic field in Fig. 2.5. Note that $\mu_{L/R}$ are chemical potentials of left and right contacts along x direction.

In order to observe SdH oscillations in 2DES, it is necessary to have $\Gamma \ll \hbar\omega_c$ or equivalently

$\omega_c \tau_q \gg 1$, which means that the broadening of Landau levels Γ does not exceed the separation between adjacent ones, $\hbar\omega_c$.

Moreover, thermal broadening of Fermi energy must be smaller than LLs separations and the latest must be smaller than Fermi energy , so that $k_B T \ll \hbar\omega_c < \varepsilon_F$. If the preceding condition satisfies for 2D system then one can observe oscillations like what is shown in Fig. 2.6.

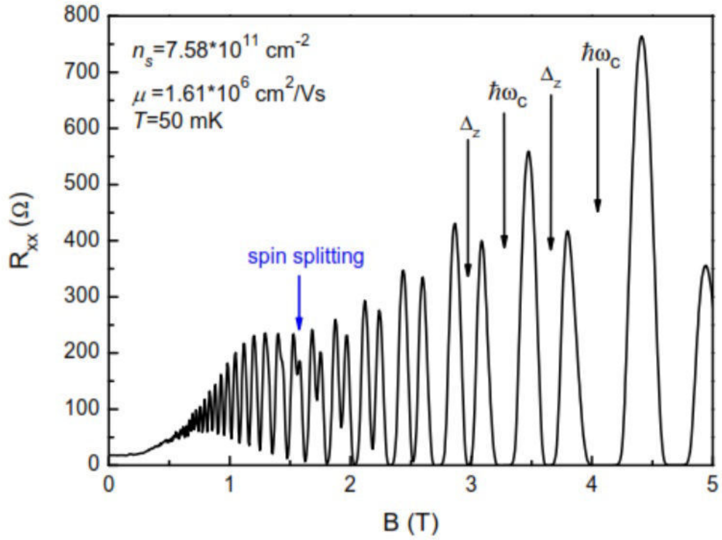

Figure 2.6: Longitudinal resistance of a quantum well in magnetic field up to 5 T at T=50 mK. SdH oscillations are visible which are starting from 0.5 T. Spin splitting starts at B=1.5 T (see blue arrow). For $B > 3$ T, one can see Zeeman splitting $\triangle_Z$ and Landau energy separation $\hbar\omega_c$. (Figure is adapted from (Wiedmann, 2010)).

According to Fig. 2.6, the onset of SdH oscillations (for this particular sample) is $B = 0.5$ T. Further increasing in magnetic field results in Spin and Zeeman splitting which are shown by Blue arrow and $\triangle_Z$ respectively.

The amplitude of SdH oscillations is given by the Lifshits-Kosevich formula (Lifshits and Kosevich, 1956)

$$\triangle R_{xx} = R_{xx}(B=0)4\mathscr{T}\exp(-\frac{\pi}{\omega_c\tau_q})\cos(\frac{2\pi\varepsilon_F}{\hbar\omega_c}), \tag{2.38}$$

where $R_{xx}(B=0)$ is zero field resistance (Drude resistance), $\mathscr{T} = \frac{X}{\sinh X}$ is the temperature damping factor with $X = \frac{2\pi^2 T_e}{\hbar\omega_c}$ (T_e is electron temperature) and $d = \exp(-\frac{\pi}{\omega_c\tau_q})$ is Dingle factor which determines disorder effects in 2DES. As the temperature increases amplitude of SdH oscillations strongly damped because of the thermal broadening of Fermi distribution which exceeds the cyclotron energy. The temperature dependence of SdH oscillations are shown in Fig. 2.7 for four different temperatures.

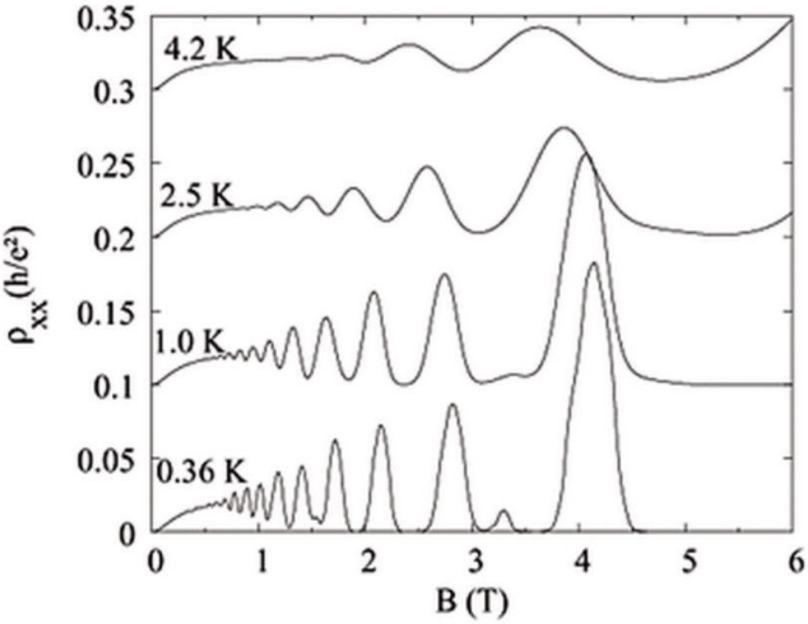

Figure 2.7: Temperature dependance of Shubnikov de Haas oscillations in longitudinal resistivity (Figure adapted from (Freire and Egues, 2004)).

2.3.4 Integer Quantum Hall effect (IQHE)

The birthday of Integer Quantum Hall Effect (IQHE) was the night of 5th of February 1980, in an experiment by Klaus von Klitzing (Klitzing, Dorda and Pepper, 1980), in which two dimensional electron gas at the surface of a single crystal silicon was exploited for measurements. The experiment resulted in resistivity tensor ρ_{xy} given by:

$$\rho_{xy} = \frac{h}{\nu e^2}, \tag{2.39}$$

with h Plank constant, e elementary charge and ν filling factor which represents the number of fully occupied Landau levels below the Fermi energy which in case of integer QHE, it would take integer values. The fascinating part of this discovery is related to the so-called Klitzing constant $R_K = \frac{h}{e^2} = 25,812.807449(86)\ \Omega$, that is proportional to the inverse of fine structure constant, $\alpha^{-1} = \frac{h}{e^2}\frac{2}{\mu_0 c} = 137$. The constants of μ_0 and c are the magnetic permeability of free space and the speed of light in vacuum, respectively. Therefore utilizing QHE, one can determine the fine structure constant. Moreover, the Hall resistance measurements are proved to be independent of the material and geometry of the semiconductors which are used and have been verified in devices made from Si , $GaAs$ and other semiconductors.

In real samples electrons move in lattice with defects and impurities which act as scattering centers for electrons and add up to phonon scatterings. However, at low temperature, in which QHE is observed, the impurity scattering is dominant. The presence of impurities has two consequences. First, it lifts the degeneracy of the Landau levels and broadens the δ like density of states. Second, it creates two different kinds of electronic states called *extended* and *localized* states in which electrons are mobile and immobile, respectively. According to the experiments, between two adjacent Landau levels, the Hall resistance has fixed values and the corresponding longitudinal resistance R_{xx} vanishes at the same time which means that the electrons are localized in this region. Localization is a key point to interpret IQHE. Based on Laughlin 1981 and Halperin 1982 explanations, the extended states exist at the core of Landau levels and localized states exist out of the core. The sketch is shown in Fig. 2.8.

Increasing the magnetic field leads to sequential passage of Landau levels from Fermi energy. Depending on the position of the Fermi energy with respect to the extended and localized states, Hall resistance shows plateaus with corresponding vanishing longitudinal resistance and phase transitions between adjacent plateaus, respectively. The experimental data of Quantum Hall effect is shown in Fig. 2.9.

Increasing electron density n_s or equivalently shifting the Fermi energy ε_F through the density of states, leads to gradual occupation of electronic states. When ε_F moves in localized stats the Hall resistance does not change and gives rise to plateau because the occupation of the extended states does not change in this case and the longitudinal resistance vanishes simultaneously. As soon as ε_F approaches the next landau level, the Hall resistance makes

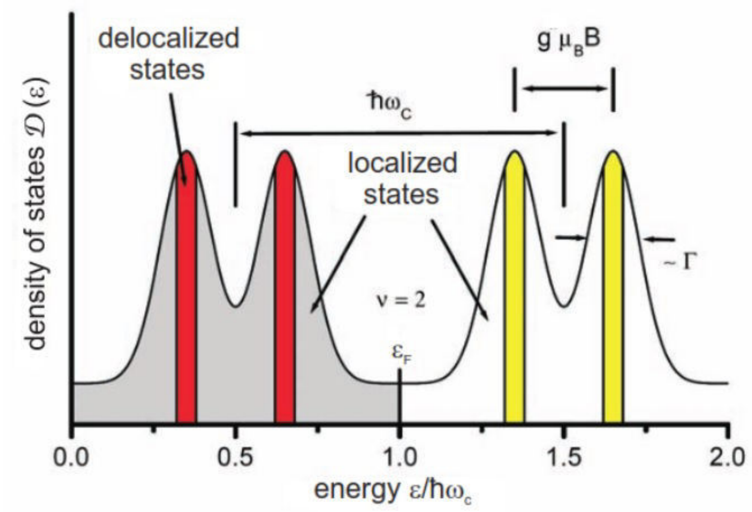

Figure 2.8: Sketch of the DOS for a 2D system in a magnetic field where the position of the Fermi energy corresponds to the filling factor, $\nu = 2$. Localized and delocalized states are shown in the center and lateral part of levels respectively (Figure adapted from (Wiedmann et al., 2010)).

transition to the next plateau. Therefore, the QHE can be realized as transitions between localized -delocalized states as the Fermi energy, ε_F, moves across the density of states.

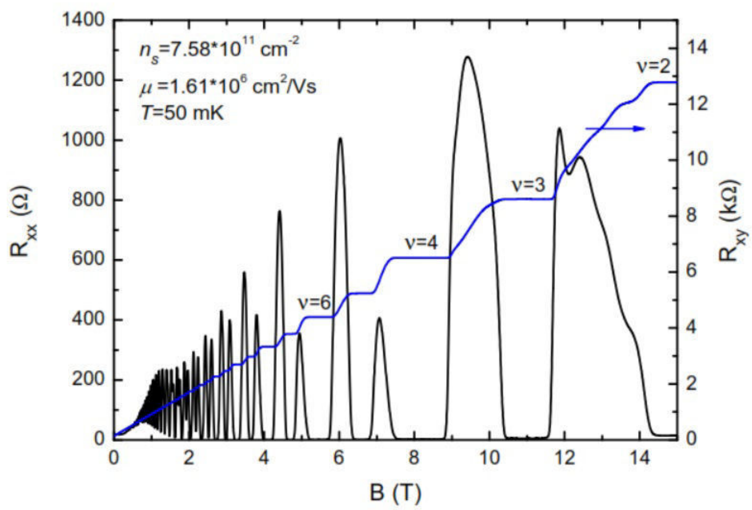

Figure 2.9: Longitudinal and Hall (transverse) resistance in a single layer system formed by a quantum well (Figure adapted from (Wiedmann et al., 2010)).

For explanation of Quantum Hall effect several arguments have been proposed including theories based on gauge invariance to some stands on edge state transport. In this part the latter will be discussed briefly. The description is based on the theory by Landauer-Buttiker (Buttiker, 1988) in which the propagation of edge states along the boundary of structure is used. The approach makes advantage of the transmission and reflection at the contacts to describe the electrical transport. Edge states come to appear due to the existence of boundary in real samples and since the electron density in these boundaries goes to zero, the potential will increase and the Landau levels bend upward near the edge as shown in Fig. 2.10.

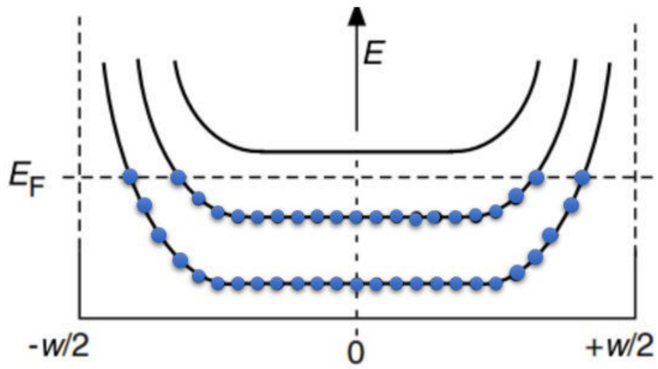

Figure 2.10: Energy spectrum of a 2DEG in a magnetic field with an infinite confining potential at the edges of the sample. States below the Fermi energy are occupied (full circle). The edge channels are located at the intersection of the Landau levels with the Fermi energy (Figure adapted from (Jeckelmann and Jeanneret, 2001)).

In this case the whole Landau levels below Fermi energy are occupied and have occupied edge states likewise. Consequently, one dimensional edge channel is formed for each Landau level traversing the Fermi energy. Therefore, edge states exist at the Fermi energy near the sample boundaries.

These edge states along the boundaries are like metallic wires, running along the sample boundary so contributed to electrical transport. Then, the current which goes to the jth contact in a sample with several contacts is given by:

$$I_j = \frac{e}{h}(N - R_j).\mu_j - \sum_k T_{jk}\mu_k, \tag{2.40}$$

where N is the number of channels, R_j is the reflection coefficient at contact j and T_{ji} is the sum of transmission coefficients from contact i to the contact j and μ represents the chemical potential.

The electron screening effect that takes place near the boundary is not considered in this formalism. This formalism is easy to handle and can be applied to many geometries. The edge state picture does not account for electrostatic screening effects of a 2DEG. At high magnetic fields, channels are forced into compressible strips separated by incompressible regions and latest scanning force microscopes reveal convincing evidences for the existence of these stripes in the depletion region at the sample edges. These experiments have shown that compressible and incompressible stripes also exist at the border between ohmic contacts and the 2DES (Chklovskii and Shklovskii, 1992; Klitzing, 2004).

2.4 Magneto-transport in bilayer electron systems

The bilayer electron systems which are realized in wide single quantum wells and in double quantum wells (DQW) are introduced in this section. Double quantum wells (DQW) form by two simple quantum wells, separated by a potential barrier. In a wide quantum well (WQW), electrons due to repulsion forces form a stable configuration in which 2DEG are formed at the side walls of the well.

The main advantage of bi-layers formed in a wide quantum well over conventional DQW can be explained according to the scattering effects in the middle barrier. In conventional DQW, the barrier between the wells is made of an alloy such as $Al_xGa_{1-x}As$ for $GaAs$ while in wide quantum wells the barrier is consists of $GaAs$ which makes the scattering due to alloy minimized in WQW (Suen et al., 1991).

The presence of the barrier in WQW or DQW opens new opportunities for studying such systems in the presence and absence of tunneling between electronic layers of each well. The extra degree of freedom due to tunneling leads to novel, different transport properties from simple single layer quantum wells. In the following, first, general properties of DQWs are introduced and then we focus on new magneto-resistance oscillations due to the possibility of intersubband transitions of electrons in such systems which is known as Magneto Inter-sub-band (MIS) Oscillations.

2.4.1 Fundamentals of Double Quantum Wells (DQWs)

Double quantum wells of $GaAs/Al_xGa_{1-x}As$ samples, consist of two simple wells of $GaAs$ separated by a potential barrier of $Al_xGa_{1-x}As$. The wave functions of electrons tunnel through the potential barrier and the system can be viewed as two parallel 2D electronic layers coupled together via tunneling which introduces a new degree of freedom and appearance of some interesting phenomena different from simple quantum wells.
If a coupled quantum well wave function ,ψ , be considered as a linear combination of wave functions, ψ_1 and ψ_2, of each well , so that $\psi_{AS/S} = a\psi_1 + b\psi_2$. Solving the *Schrödinger* equation for ψ leads to a symmetric-antisymmetric energy gap of $\triangle_{SAS} = \varepsilon_{AS} - \varepsilon_S$, where ε_{AS} and ε_S are energy of antisymmetric and symmetric combination of ψ_1 and ψ_2, respectively. This separation, strongly depends on the width and height of the potential barrier. For small thickness of barrier the separation will increase. Moreover, the symmetric DQWs is called balanced when the electron densities are equal in two wells. The conduction band edge and the two lowest energies and wave functions of a symmetric double quantum well of $Al_xGa_{1-x}As/GaAS/Al_xGa_{1-x}As$ are demonstrated in Fig. 2.11. For comparison between WQW and DQW the same information for WQW is also presented in Fig. 2.11.

In DQWs at high magnetic fields in addition to cyclotron energy gap $\hbar\omega_c$ and Zeeman gap due to spin splitting $\triangle_Z$, another energy gap exists due to the symmetric and antisymmetric hybridization of wave functions of each well which is shown by $\triangle_{SAS}$ and this energy gap determines the coupling strength of two quantum wells. According to the coupling between the quantum wells, it is possible to define three regimes in DQWs. First, is the "No coupling" regime where there is no overlap between electronic wave functions of each wells and also there is no coulomb interaction between them. Second regime is the case with coulomb

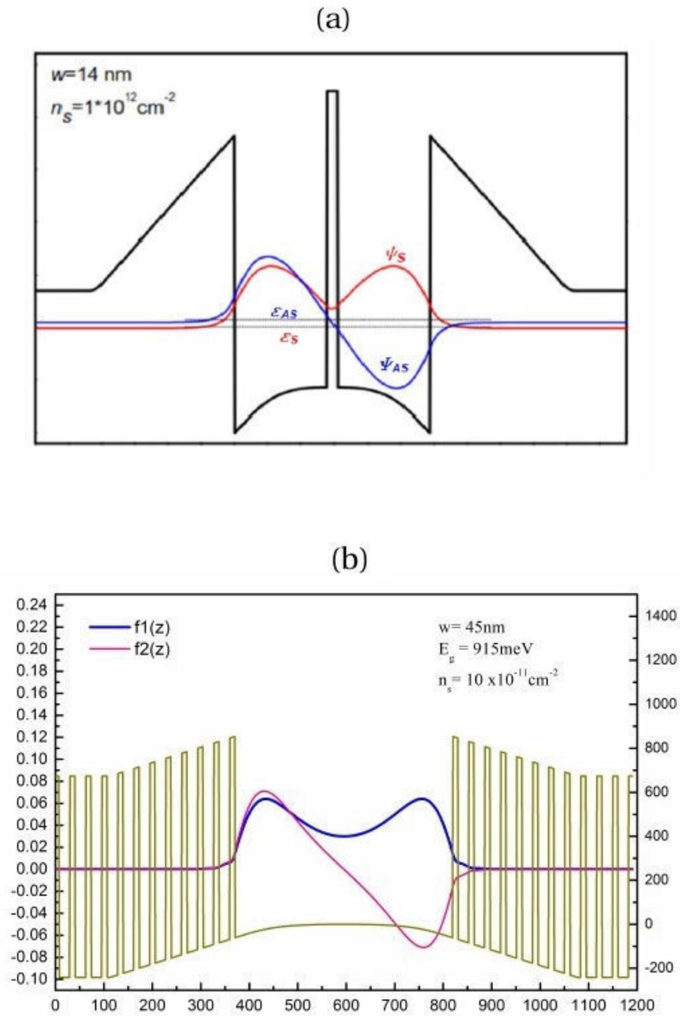

Figure 2.11: (a) Schematic of band structure of DQW derived from Hartree-Fock calculation with symmetric and antisymmetric wave function for the lowest occupied subbands and corresponding energies. (b) Symmetric and anti-symmetric wave functions in WQW.(Figure is adapted from (Wiedmann et al., 2010)).

interaction present while there is no tunneling between quantum wells and can be considered as "Coulomb coupling" regime. The last regime is the case with tunneling present between the wells and depending on the strength of tunneling can be classified as "weak or strong coupling" regime. The energy and Landau fan diagram for two set of spin split Landau levels separated by $\triangle_{SAS}$ of DQW system is shown in Fig. 2.12.

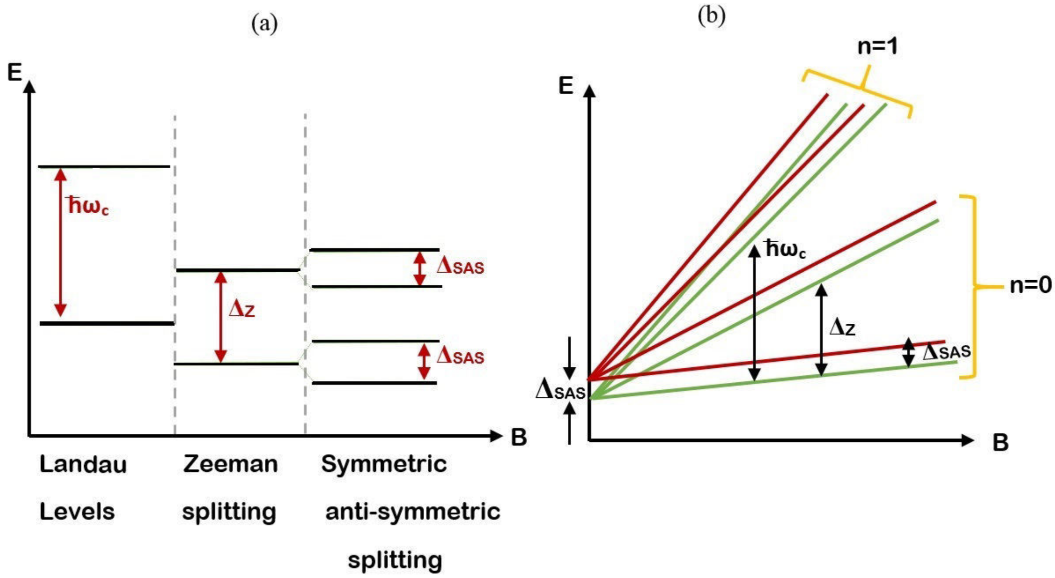

Figure 2.12: (a) Energy diagram with the cyclotron energy ($\hbar\omega_c$), Zeeman energy ($\triangle_Z = \mu g^* B$) and symmetric-antisymmetric energy ($\triangle_{SAS}$). (b) Landau fan diagram for a DQW.

2.4.2 Magneto intersubband oscillations (MIS)

There are another kind of magneto-resistance oscillations that exist in quantum wells with at least two sub-band occupied. The origin of these kind of oscillations is the periodic modulation of the probability of intersubband transitions between different Landau levels with magnetic field and called magneto intersubband oscillations (MIS). Unlike SdH oscillations

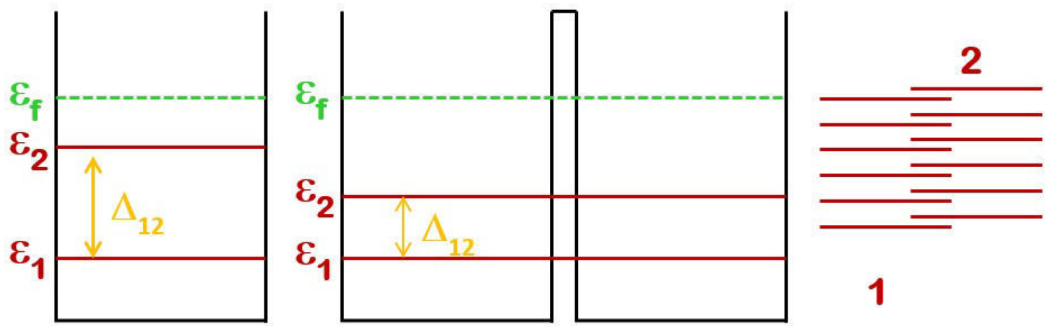

Figure 2.13: (a) QW with two occupied 2D subbands and (b) DQW-system with two occupied 2D subbands with energies ε_1 and ε_2 and staircase of Landau levels giving rise to MIS oscillations (Figure adapted from Wiedmann (2010)).

which are originating from sequential passage of Landau levels through the Fermi level, MIS oscillations are more robust to temperature, since their origin has nothing to do with the Fermi energy. In case of SdH oscillations broadening of Fermi distribution that exceeds cyclotron energy $\hbar\omega_c$ leads to considerable suppression of SdH oscillations while MIS oscillations can persist in higher temperature in comparison with SdH and provides a tool for studying system in the regions of temperature where SdH is no more exist.

The maximum of MIS oscillations appears when sub-band separation meet the condition of $\triangle = n\hbar\omega_c$ (n is an integer), that corresponds to the maximum elastic scattering of electrons between different Landau levels (Wiedmann et al., 2009).

In the following, the theoretical description of low field magneto-resistance oscillations is provided. In high filling factors which corresponds to weak magnetic fields, the resistivity can be extended up to second order in Dingle factors:

$$\rho_d = \rho_d^{(0)} + \rho_d^{(1)} + \rho_d^{(2)}, \tag{2.41}$$

with $\rho_d^{(0)}$ the classical resistivity, $\rho_d^{(1)}$ the first order term in Dingle factor which describes the SdH oscillations in quantum contribution to the resistivity and finally $\rho_d^{(2)}$ the second order term in Dingle factor taking into account other quantum contributions specifically MIS oscillations in our DQW system and this is the term which survives at higher temperatures unlike second term which contains SdH oscillations. According to Zaremba 1992 and Raichev 2008 that describe the classical and quantum contributions to the resistivity respectively, it is possible to write these contributions as follow:

$$\rho_d^{(0)} = \frac{m}{e^2 n_s} \frac{\omega_c \nu_s + \nu_0 \nu_r^2}{\omega_c^2 + \nu_r^2}, \tag{2.42}$$

and the first order quantum contribution describing SdH oscillation would be:

$$\rho_d^{(1)} = -\mathcal{T} \frac{2m}{e^2 n_s} \sum_{j=1,2} [\frac{2n_{sj}}{n_s} \nu_{jj}^{tr} + \nu_{12}^{tr}] \exp(-\frac{\pi \nu_j}{\omega_c}) \cos(\frac{2\pi(\varepsilon_F - \varepsilon)}{\hbar\omega_c}), \tag{2.43}$$

and the last term describing the second order contribution is given by:

$$\rho_d^{(2)} = (\frac{2m}{e^2 n_s})[\frac{n_1}{n_2}\nu_{11}^{tr}\exp(-2\frac{\pi\nu_1}{\omega_c}) + \frac{n_2}{n_s}\nu_{22}^{tr}\exp(-2\frac{\pi\nu_2}{\omega_c}) + \nu_{12}^{tr}\exp(-\frac{\pi\nu_1}{\omega_c} - \frac{\pi\nu_2}{\omega_c})\cos(\frac{2\pi\triangle_{12}}{\hbar\omega_c})]. \tag{2.44}$$

In these equations n_s is the total density of electrons attained from adding electron densities of each sub-band n_1 and n_2, so that $n_s = n_1 + n_2$. The elastic quantum scattering rate and transport scattering rate at the Fermi surface are $\nu_{jj'}$ and $\nu_{jj'}^{tr}$ respectively which leads to definition of some characteristics rates of ν_0 , ν_s, ν_r presented as:

$$\begin{aligned}
\nu_0 &= D/\nu_r \\
D &= (\nu_{11}^{tr} + \nu_{12})(\nu_{22}^{tr} + \nu_{12}) - (\nu_{12} - \nu_{12}^{tr})^2 n_s^2/4n_1 n_2 \\
\nu_r &= (\frac{n_2}{n_s})\nu_{11}^{tr} + (\frac{n_1}{n_2})\nu_{22}^{tr} + 2\nu_{12} - \nu_{12}{}^{tr} \\
\nu_s &= (\frac{n_1}{n_2})\nu_{11}^{tr} + (\frac{n_2}{n_s})\nu_{22}^{tr} + \nu_{12}^{tr},
\end{aligned} \tag{2.45}$$

while the sub-band dependent quantum relaxation rates and transport scattering rates are defined as

$$\begin{aligned}
\nu_j &= \sum_{j'=1,2} \nu_{jj'}, \\
\nu_j^{tr} &= \sum_{j'=1,2} \frac{n_j + n_{j'}}{n_s}\nu_{jj'}^{tr},
\end{aligned} \tag{2.46}$$

with

$$\begin{aligned}
\left.\begin{matrix}\nu_{jj'} \\ \nu_{jj'}^{tr}\end{matrix}\right\} &= \frac{1}{2\pi}\int_0^{2\pi} d\theta\, \nu_{jj'}(\theta) \times \left\{\begin{matrix}1 \\ F_{jj'}(\theta)\end{matrix}\right. \\
\nu_{jj'}(\theta) &= \frac{m}{\hbar^3} w_{jj'}(\sqrt{(k_j^2 + k_{j'}^2)F_{jj'}(\theta)}),
\end{aligned} \tag{2.47}$$

where $w_{jj'}$ are the Fourier transforms of the correlators of the scattering potential, $F_{jj'} = 1 - 2k_j k_{j'} \cos\theta/(k_j^2 + k_{j'}^2)$, θ is the scattering angle and the Fermi wavenumber for sub-band j is $k_j = \sqrt{2\pi n_j}$. Considering the following approximations the general expression for DQW is considerably simplified as

$$\frac{\rho_d}{\rho_0} \simeq 1 - 2d\mathcal{T} \sum_{j=1,2} \cos\frac{2\pi(\varepsilon_F - \varepsilon_j)}{\hbar\omega_c} + d^2[1 + \cos\frac{2\pi\Delta_{12}}{\hbar\omega_c}], \tag{2.48}$$

where it is approximated that $n_1 \simeq n_2 \simeq n_s/2$, $\nu_{11} \simeq \nu_{22}$, $\nu_{11}^{tr} \simeq \nu_{22}^{tr}$ and $\nu_{11}^* \simeq \nu_{22}^*$, which also leads to $\nu_1 \simeq \nu_2$, $d_1 \simeq d_2$, $\nu_1^{tr} \simeq \nu_2^{tr} \simeq \tau_{tr}^{-1}$ and $\nu_1^* \simeq \nu_2^* \simeq \tau_*^{-1}$. Moreover, $\nu_{12}^{tr} \simeq \nu_{jj}^{tr}$ and $\nu_{12}^* \simeq \nu_{jj}^*$ is also valid for balanced DQW used in this thesis.

2.5 Microwave induced resistance oscillations (MIRO)

2.5.1 Experimental discovery and basic properties

The electrodynamics response of a quantum Hall systems is one the main issues in physics of correlated systems. Therefore, non-equilibrium magneto-transport phenomena in two dimensional electron systems under Microwave (MW) irradiation are of great interests.

The experimental observation of microwave-induced resistance oscillations (MIROs) in longitudinal resistance is possible for samples with a sufficiently high-mobility 2DEG, subjected to a weak perpendicular magnetic field and illuminated by microwave radiation (Zudov et al., 1997, 2001). Under these conditions magneto-resistivity, $\rho(B)$ exhibits giant oscillations periodic in the inverse magnetic field, 1/B, and satisfy a resonance condition in which cyclotron energy is an integer multiple of the radiation energy, $\hbar\omega = n\hbar\omega_c$ with n ($n = 1, 2, 3, ...$), the difference between the indices of participating Landau levels. Moreover, in the experiments on microwave irradiation of very high mobility ($\mu \geq 10^7\ cm^2/Vs$) 2DEG samples, Mani et al. (2002) and Zudov et al. (2003) observed that (see Fig. 2.14) in appropriate microwave intensity and temperature the lower order minima of MIRO can extend all the way to zero forming zero resistance states(ZRS).

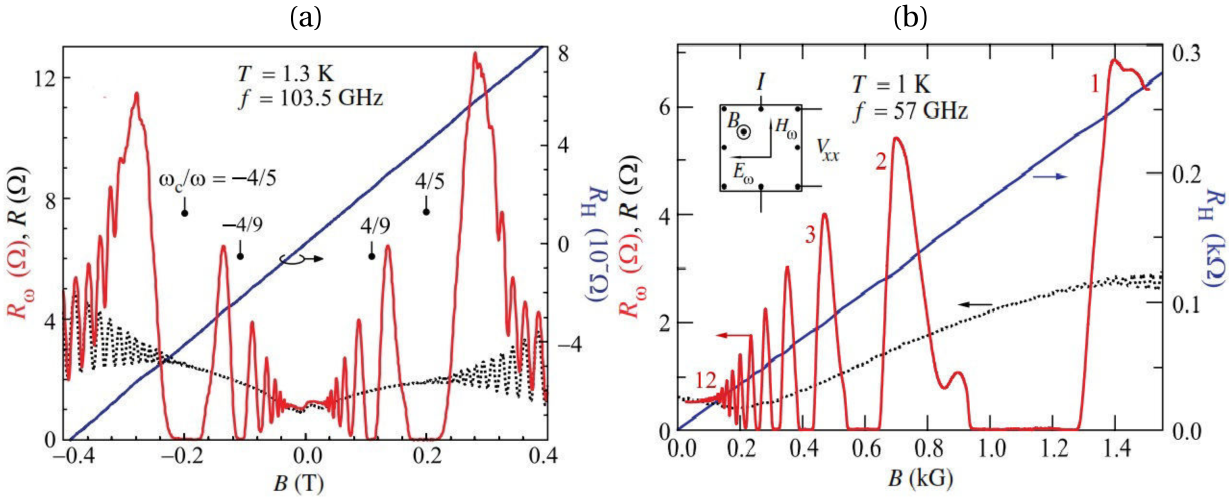

Figure 2.14: Longitudinal (left axis), $R_{\omega}(B)$ and Hall $R_H(B)$ (right axis) magneto-resistance under microwave irradiation. Longitudinal magneto-resistance $R(B)$ without irradiation is also shown. Parameters (a) microwave frequency $f = 103.5$ GHz, temperature $T = 1.3$ K, electron density $n_e \simeq 3 \times 10^{11}\ cm^{-2}$ and mobility $\mu \simeq 1.5 \times 10^{7}\ cm^{2}/Vs$ (Figure adapted from (Mani et al., 2002)), (b) $f = 103.5$ GHz, $T \simeq 1.0$ K, $n_e \simeq 3.5 \times 10^{11}\ cm^{-2}$ and $\mu \simeq 2.5 \times 10^{7}\ cm^{2}/Vs$ (Figure adapted from (Zudov et al., 2003)).

ZRS can span magnetic-field ranges corresponding to several tens in filling factors. However, unlike the quantum Hall effect, vanishing of diagonal resistance in microwave irradiated 2DEG is not accompanied by Hall quantization. The observation of ZRS is of great interest because it is a rare occurrence in condensed-matter physics, usually signaling a novel state of matter, such as superconductivity and QH effects and is often an indication that some interesting physics is afoot.

Since the electrical resistance of most materials can be associated to the inhibition of the electron flow by scattering from impurities, defects and excited modes of the system. One of the possibilities to explain the microwave induced zero resistance state is based on a new collective state induced by microwave irradiation.

2.5.2 MIRO mechanisms

The microwave irradiation can affect the transport properties. The combined effect of Landau quantization and external magnetic fields either on the momentum relaxation or on the energy distribution of electrons within disorder-broadened LLs can be exploited in explanation of experimental findings concerning MIRO via two important mechanisms. The first considerations lead to *displacement* mechanism, proposed by Durst et al. (2003) and involves simultaneous photo excitation and disorder scattering of electrons while the second one is called *inelastic* mechanism, associated with non equilibrium oscillatory component of the distribution function of electrons under microwave irradiation, introduced by Dorozhkin (2003) and Dmitriev et al. (2005). The latter is likely to be the dominant mechanism in studied experimental systems.

Comparing microwave induced magneto-resistance with corresponding dark values of diagonal conductivity, the mentioned mechanisms lead to the reduction of conductivity and for radiation of sufficient intensity it pass through zero resistance and even negative values, $\sigma_{xx} < 0$ result. Since the system is injected with energy in the form of microwave, we deal with a non-equilibrium phenomena which negative resistance is reasonable for the systems.

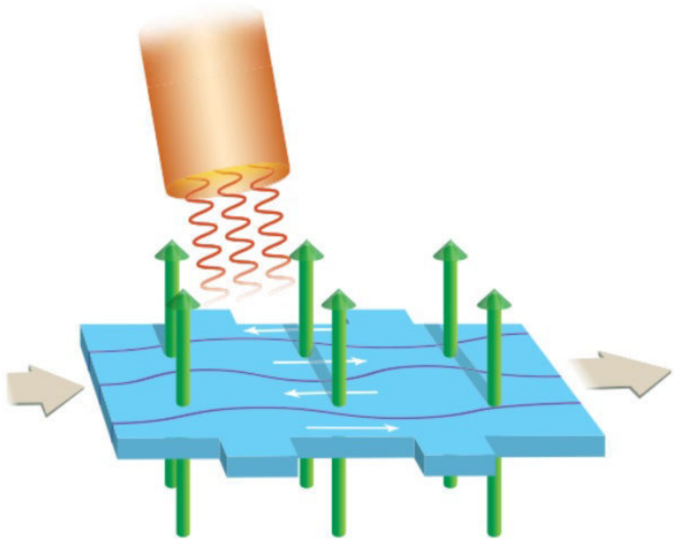

Figure 2.15: Schematic picture of 2DEG in an applied perpendicular magnetic field (green arrows) irradiate by microwave (red). Domain walls which separate the current regions (purple) of larg counter flowing current density. Net current to the right side shown by larg gray arrow (Figure adapted from (Durst and Girvin, 2004)).

Andreev , Aleiner and Millis (2003) provides explanation for observed zero resistance and it is shown that since the negative resistance states make the homogeneous current distribution electrodynamically unstable, the system can spontaneously rearrange itself into an intricate current pattern , as is shown in Fig. 2.15, which consists of domain walls separating large local current density regions with zero resistance (Durst and Girvin, 2004).

In the following sections, displacement and inelastic mechanisms will be introduced. In the theoretical part, $\hbar = k_B = 1$ is considered.

Displacement mechanism (DP)

This mechanism explains microwave induced magneto-resistance oscillations using disordered assisted absorption and emission of microwave by electrons which results in an alteration of electrons momentum and consequently introduces a supplementary current in the system. This photo-current can become negative and even leads to the negative diagonal resistivity, passing the dark current. The formulation of this mechanism was done long time ago by Ryzhii (1970); Ryzhii et al. (1986) in the context of a strong DC electric field. The schematic model in Fig. 2.16 gives the basic idea of the DP mechanism.

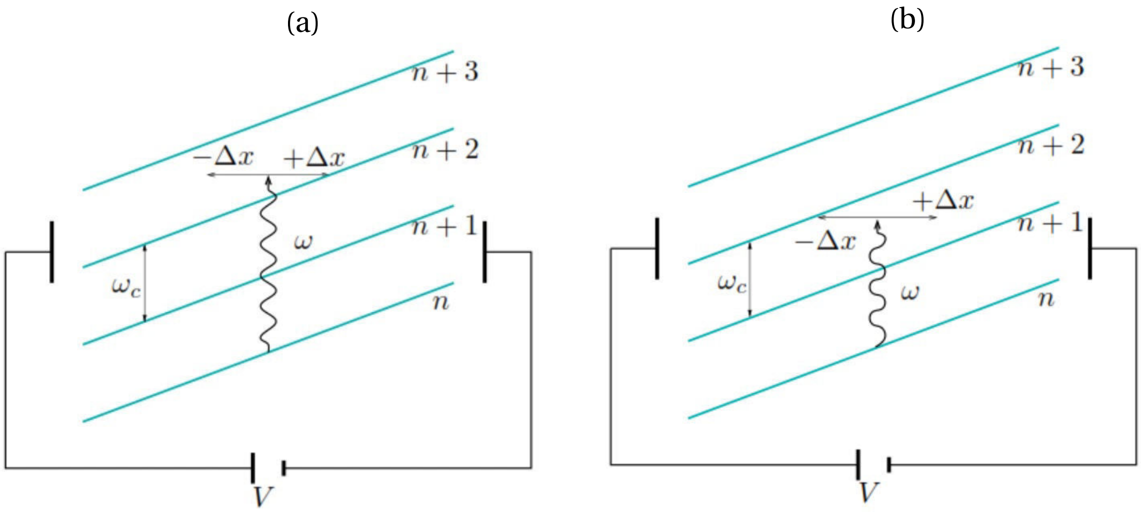

Figure 2.16: Sketch of displacement mechanism. (a) For $\omega > 2\omega_c$, which electron is disorder scattered into the (n+2)nd Landau level to the right and results in decreasing current. (b) For $\omega < 2\omega_c$ that the electron is excited below the (n+2)nd Landau level, so that it scatteres to the left and leads to the augmentation of the total current (Figure adapted from (Durst et al., 2003)).

When an external electric field, E_{dc}, is applied in x direction the Landau levels, which are separate by ω_c, are tilted as

$$\varepsilon_n \simeq n\hbar\omega_c + eE_{dc}x, \tag{2.49}$$

The broadening of Landau levels due to disorders are ignored for simplicity. When a photon with frequency of ω is absorbed by electron, it would be excited by $\hbar\omega$ and scattered to the left or right, $\pm\triangle x$, with the same probability, depending on the energy they absorb due to microwave irradiation.

If the electron energy is a bit more than the separation between Landau levels, $\hbar\omega > n\hbar\omega_c$, then the electron scatters in the opposite direction of applied electric field and the conductivity decreases, otherwise ($\hbar\omega < n\hbar\omega_c$) it scatters along applied electric field and the conductivity increases.

It is possible to calculate the position dependent rate of scattered electrons exploiting a generalization of Fermi's golden rule and average over disorder (for details see (Durst and Girvin, 2004)) which results in the following equation for the density of states

$$D(\varepsilon) = D_0 + D_1 \cos\frac{2\pi\varepsilon}{\hbar\omega_c}, \tag{2.50}$$

with D_i averaged local density of states.Then the excess conductivity is given by

$$\triangle\sigma_{xx} \propto \frac{\partial D(\varepsilon)}{\partial\varepsilon}|_{\varepsilon=\hbar\omega} \propto -\sin\frac{2\pi\omega}{\omega_c}. \tag{2.51}$$

The displacement mechanism describes the periodicity and phase of MIRO and leads to a locally negative conductivity which appears to be truncated at zero and consequently ZRS in conductivity oscillations.

Inelastic mechanism

The theory of Inelastic mechanism which was developed by Dorozhkin (2003) and Dmitriev et al. (2005), provides an explanation for resistance oscillations arise under microwave irradiation based on an oscillatory part of the electron distribution function. The approach is based on the Quantum Boltzmann equation (QBE) for a semi-classical distribution function of electrons at higher Landau levels which exploits to describe the kinetics of a 2DEG subjected to MW and magnetic field. When microwave irradiation is introduced to the 2D electron system, it drives the distribution function of electrons out of equilibrium and leads to a population inversion which could be responsible for negative resistivity due to the appearance of a negative photo current. The simple sketch shown in Fig. 2.17 , demonstrate the occurring of population inversion in higher and lower Landau levels according to the applied microwave frequency.

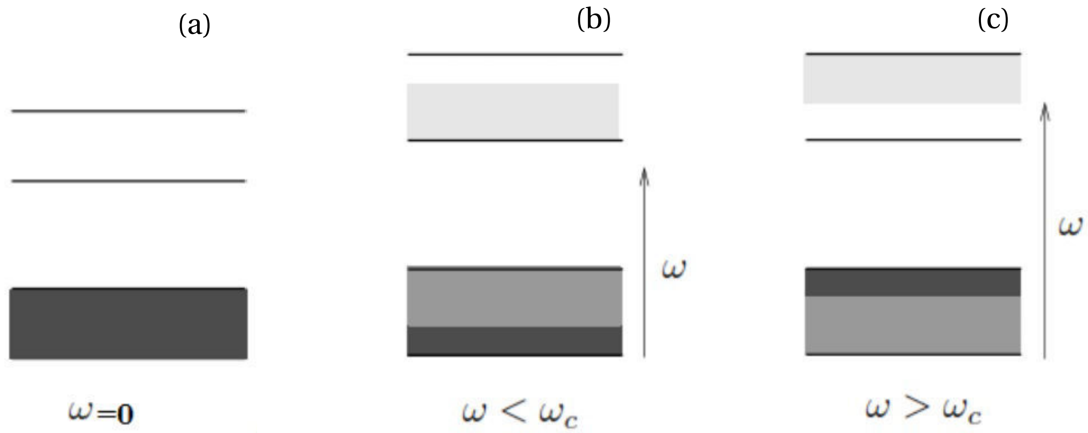

Figure 2.17: Sketch of the change in electronic distribution in the presence of a driving microwave field with total occupation normalized to unity. Dark gray shows complete filling states, light gray indicates a small occupation and intermediate gray represents an occupation $(1-\varepsilon)$. (a) The equilibrium situation without microwave irradiation $\omega = 0$, a completely filled and a totally empty (disorder-broadened) Landau band are shown. (b) The occupation of these bands is sketched for $\omega > \omega_c$ and (c) The occupation for $\omega < \omega_c$, the case that Landau bands show a population inversion.

For microwave frequency below cyclotron $\omega < \omega_c$, higher Landau band fills partially, hence there is a positive contribution to the photo-conductivity. However, when the microwave frequency exceeds that of cyclotron $\omega > \omega_c$, the redistribution of electrons in Landau levels leads to a population inversion in both higher and lower Landau levels. The redistribution of electrons in the presence of microwave irradiation, is due to inelastic relaxation which leads electron distribution in dynamical equilibrium.

The total photo-conductivity per spin for a system under microwave irradiation is given by

$$\sigma_{ph} = \int d\varepsilon \sigma_{dc}(\varepsilon)\,[-\partial_\varepsilon f(\varepsilon)], \tag{2.52}$$

where f_ε is non equilibrium distribution function, ∂_ε derivative with respect to energy ε and $\sigma_{dc}(\varepsilon)$ is the contribution of electrons with energy ε to the dissipative transport and is given by

$$\sigma_{dc}(\varepsilon) = \sigma^D_{dc}\tilde{D}^2(\varepsilon) = \frac{e^2 D_0 \upsilon_F^2}{2\omega_c^2\tau_{tr}}.\frac{D(\varepsilon)}{D_0}, \tag{2.53}$$

where υ_F Fermi velocity $D_0 = \frac{m^*}{\pi\hbar^2}$ and $D(\varepsilon)$ are zero field $B = 0$ and oscillatory DOS of electrons respectively, $\tilde{D}(\varepsilon) = \frac{D(\varepsilon)}{D_0}$ dimensionless density of states, and σ^D_{dc} represents Drude conductivity. Using kinetic approach the electron distribution function under microwave irradiation can be computed, which includes collision integrals due to microwave absorption and emission, and a term regarding inelastic relaxation. More details are provided in (Dmitriev et al., 2005). The kinetic equation then can be written as

$$\frac{P_\omega}{4}\sum_{\pm}\tilde{D}(\varepsilon \pm \omega)[f(\varepsilon \pm \omega) - f(\varepsilon)] + \frac{Q_{dc}{\omega_c}^2}{4\pi^2\tilde{D}(\varepsilon)^2}\partial_\varepsilon[\tilde{D}(\varepsilon)^2\partial\varepsilon f(\varepsilon)] = f(\varepsilon) - f_T(\varepsilon), \tag{2.54}$$

with

$$\begin{aligned} P_\omega &= \frac{\tau_{in}}{\tau_{tr}}(\frac{eE_\omega \upsilon_F}{\omega})^2\frac{\omega_c^2+\omega^2}{(\omega^2-\omega_c^2)^2} \\ Q_{dc} &= 2\frac{\tau_{in}}{\tau_{tr}}(\frac{eE_{dc}\upsilon_F}{\omega})^2(\frac{\pi}{\omega_c})^2, \end{aligned} \tag{2.55}$$

which are dimensionless units for strength of microwave E_ω and dc electric field E_{dc}. Solving the kinetic equation to first order in dingle factor, $d = \exp(\frac{-\pi}{\omega_c\tau_q})$, results in

$$
\begin{aligned}
f &= f_0 + f_{Osc} + O(d^2) \\
f_{Osc} &= d\frac{\omega_c}{2\pi}.\frac{\partial f_T}{\partial \varepsilon}.\sin\frac{2\pi\varepsilon}{\omega_c}[\frac{p_\omega \frac{2\pi\omega}{\omega_c} sin\frac{2\pi\omega}{\omega_c} + 4Q_{dc}}{1 + p_\omega \sin^2\frac{2\pi\omega}{\omega_c} + Q_{dc}}]],
\end{aligned}
\tag{2.56}
$$

The oscillatory part of distribution function , which is also shown in Fig. 2.18, results in the oscillatory photo-conductivity in the form of

$$
\sigma_{ph} = \sigma^D_{dc}(1 + 2d^2[1 - \frac{p_\omega \frac{2\pi\omega}{\omega_c}\sin\frac{2\pi\omega}{\omega_c} + 4Q_{dc}}{1 + p_\omega \sin^2\frac{2\pi\omega}{\omega_c} + Q_{dc}}]), \tag{2.57}
$$

which include both dc and microwave field in the case of overlapping Landau levels.

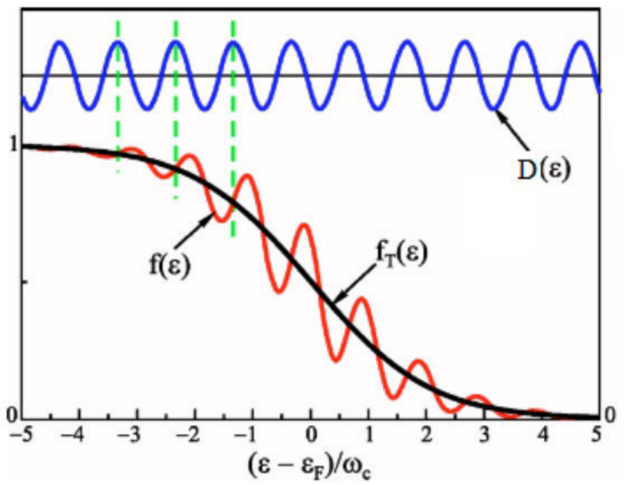

Figure 2.18: Schematic behavior of the oscillatory density of states D(ε) and radiation induced oscillations in the distribution function f(ε)(Figure adapted from (Dmitriev et al., 2005)).

It is also demonstrated in (Dmitriev et al., 2005) that a coincidence of maxima of DOS with regions of inverted population in electron distribution function is required for a negative local resistivity. Therefore, changes in distribution function due to MW irradiation give rise to possible ZRS.

The most important aspect of this mechanism is that MIRO and ZRS temperature dependence is well explained due to temperature dependence of inelastic relaxation time $\tau_{in} \propto T^{-2}$. Then it is necessary to calculate inelastic relaxation time, τ_{in}, which for not too high temperature is mainly due to inelastic scattering in electron-electron collisions. The oscillatory part of distribution function relaxes because of $e-e$ scattering and this relaxation provides a way to determine the temperature dependence of oscillating photo-resistance which in case of overlapping Landau levels is given by

$$\frac{1}{\tau_{in}} = \frac{1}{\tau_{ee}} = \frac{\pi^2 T_e^2 + \varepsilon}{4\pi\varepsilon_F} \ln \frac{\kappa v_F}{\omega_c\sqrt{\omega_c \tau_{tr}}} \simeq \frac{T_e^2}{\varepsilon_F}, \tag{2.58}$$

with $\kappa = \frac{4\pi e^2}{D_0}$, the inverse screening length of dynamically screened coulomb potential. This mechanism seems to play dominant role in experimentally studied systems.

2.6 Thermopower Basics

When a temperature gradient, ∇T , is applied to the two dimensional electron system, a thermally induced electric current, **j** would built up along the temperature gradient. This effect is called *Thermo-electric* effect. Moreover the heat current **Q**, carried by electric current **j**, leads to thermal effects. The phenomenological relations (Zhang et al., 2009) associated to these effects are

$$\begin{aligned} \mathbf{j} &= \hat{\sigma}\ \mathbf{E} - \hat{\beta}\ \nabla T \\ \mathbf{E} &= \hat{\rho}\ \mathbf{j} + \hat{\alpha}\ \nabla T \\ \mathbf{Q} &= \hat{\pi}\ \mathbf{j} - \hat{k}\ \nabla T \end{aligned} \tag{2.59}$$

where thermopower tensor, $\hat{\alpha}$ is $\hat{\alpha} = -\hat{\rho}\ \hat{\beta}$ (α_{xx} and α_{xy} is called thermopower and Nernst Ettingshausen coefficient respectively) and Peltier coefficient π is given by $\pi = \hat{\alpha}\ T$.

In general there are two components contributed to the thermopower (TEP) of a two dimensional electron system .

- Electron diffusion α^d, due to the temperature gradient

- Phonon drag α^g , due to phonon diffusion with dragging electrons along.

Therefore the thermopower can be written as the sum of these two contribution in general, $\alpha = \alpha^d + \alpha^g$. Moreover , the configuration, used for experimental measurements of thermopower is *Open circuit* method in which $j = 0$, so that $\alpha = \frac{E}{\nabla T}$. In the following, we present a brief description on the *diffusive* and *phonon drag* contributions of thermopower.

2.6.1 Diffusive thermopower (α^d)

Diffusion thermopower is a powerful tool in 2DES because it is possible to determine the electron entropy through it and therefore get information about the DOS and its changes when the system undergoes phase transition.

The first theoretical papers on magneto thermo-electric of 2D systems were mostly related to diffusion component of thermopower however it proved that finding experimental data for comparison would be difficult and most measurement dealt with the phonon drag contribution.

In the following the theoretical consideration of diffusion thermopower will be introduced.

We consider a two dimensional degenerate electron gas in a range of temperature where the dominant scattering process is elastic scattering due to impurities. The diffusion thermopower then is given by Mott formula. When electric and magnetic fields with temperature gradient applied on the 2D system, the Boltzmann equation gives rise to the Fermi distribution function of electrons $f(\varepsilon)$, through it the conductivity can be written as

$$\sigma = \int_0^\infty d\varepsilon(-\frac{\partial f(\varepsilon)}{\partial \varepsilon})\sigma(\varepsilon), \tag{2.60}$$

where $\sigma(\varepsilon)$ is the zero temperature conductivity tensor as a function of energy which contains all the dynamical information of electronic systems including scattering of electrons. The diffusion thermo-electric tensor is then given by

$$\alpha^d = -\frac{1}{eT}\int_0^\infty d\varepsilon(-\frac{\partial f(\varepsilon)}{\partial\varepsilon})(\varepsilon-\varepsilon_F)\sigma(\varepsilon), \tag{2.61}$$

Almost all the experimental work has been on samples with degenerate electron or hole gases in a temperature range where carrier scattering by the impurities is dominant. Ignoring quantum oscillations, when the scattering is elastic, the diffusion thermopower is given by the well known Mott result. In Quantum Hall regime, the diffusion oscillations of α_{xx} are similar to ρ_{xx}, with zeros at full Landau levels and peaks at half filling ones. If we ignore the spin splitting then

$$\alpha_{xx} = -\frac{k_B \ln 2}{e(\nu+1/2)}, \tag{2.62}$$

where k_B is Boltzmann constant , ν the filling factors of Landau levels and e is the electronic charge.

For Low magnetic fields the resistivity ρ of 2DEG is described by the following equations (For more details see (Coleridge et al., 1989))

$$\begin{aligned}\tilde{\rho_{xx}} &= 4\bar{\rho}_{xx}D(X)\exp(-\frac{2\pi^2 k_B T_D}{\hbar\omega_c})\cos(\frac{2\pi\varepsilon_F}{\hbar\omega_c}-\pi)\\ \tilde{\rho_{yx}} &= -\frac{2}{\omega_c^2\tau_{tr}^2}\bar{\rho}_{yx}D(X)\exp(-\frac{2\pi^2 k_B T_D}{\hbar\omega_c})\cos(\frac{2\pi\varepsilon_F}{\hbar\omega_c}-\pi),\end{aligned} \tag{2.63}$$

with $\tilde{\rho}$ and $\bar{\rho}$ representing the monotonic and oscillatory part of magneto-resistance, $D(X)$ thermal damping factor which is given by $D(X) = \frac{X}{Sinh(X)}$, with $X = \frac{2\pi^2 k_B T}{\hbar\omega_c}$, τ_{tr} transport relaxation time and T_D Dingle temperature which is related to Landau level broadening Γ by $\Gamma = \pi k_B T_D = \frac{\hbar}{\tau_q}$ with τ_q, the quantum life time.

Note that the equations above are derived for short range scattering case in which τ_{tr} and τ_q are considered indistinguishable and for simplicity these equations are used to derive the components of thermopower. Coleridge et al. (1989) and Laikhtman and Altshuler (1994) extend the method for distinguishable τ_{tr} and τ_q and they confirms the same equations. The components of thermopower (Fletcher et al., 1995) finally can be written as

$$
\begin{aligned}
\tilde{\alpha}_{xx} &= \frac{2}{1+\omega_c^2\tau_{tr}^2}\left(\frac{\pi k_B}{e}\right)D^{'}(X)\exp\left(-\frac{2\pi^2 k_B T_D}{\hbar\omega_c}\right)\sin\left(\frac{2\pi\varepsilon_F}{\hbar\omega_c}-\pi\right) \\
\tilde{\alpha}_{yx} &= \frac{4\omega_c\tau_{tr}}{1+\omega_c^2\tau_{tr}^2}\left(\frac{\pi k_B}{e}\right)D^{'}(X)\exp\left(-\frac{2\pi^2 k_B T_D}{\hbar\omega_c}\right)\sin\left(\frac{2\pi\varepsilon_F}{\hbar\omega_c}-\pi\right),
\end{aligned} \tag{2.64}
$$

where $D^{'}(X)$ is the derivative of thermal damping with respect to X.

2.6.2 Phonon drag thermopower (α^g)

The basic understandings of phonon drag contribution in 2D systems established by Cantrell and Butcher (1986); Smith and Butcher (1989) group. The essence of the problem is that the phonons are not in equilibrium in the substrate, but preferentially flow down the temperature gradient ∇T. Because of the e–p interaction, carriers are dragged towards the colder end of the sample giving an extra contribution to the current and hence to $\hat{\beta}$.

In the presence of temperature gradient ∇T in a sample, phonons flow from hot temperature side to the cold place and this flow produces the heat current, Q, through the sample. The movement of phonons along ∇T leads to a net phonon momentum P in the system, which is transferred to electrons as well result in P_e and causes them to flow along the same direction.

In open circuit condition an electric field is built up and the electric current will cancels out the phonon drag electron flow. Then the macroscopic zero field thermopower due to phonon drag contribution for 3D phonons is given by

$$
\alpha_0^g = -\frac{1}{3e}\frac{C_v}{n_e}\frac{\tau_p}{\tau_{pe}} \propto \frac{T^3}{n_e}, \tag{2.65}
$$

that C_v is specific heat, τ_p phonon relaxation time and τ_{pe} electron relaxation time due to electron phonon interaction. Details of derivation of Eq. 2.65 is provided in (Smith and Butcher, 1989). The temperature dependence in Eq. 2.65 is T^3 while in case of diffusion thermopower and Mott formula the dependency is linear in T. This different temperature dependence can be used to distinguish diffusion contribution from phonon drag one.

As it is apparent the electron relaxation time τ_e does not appear in Eq. 2.65 which means that the impurity scattering of electrons has no contribution in phonon drag thermopower of α^g and only electron phonon interactions matter. Therefore α^g provides an important tool to study electron-phonon interactions at low temperatures. Since the phonon drag contribution is the dominant one in our experiments more details about it is provided in § 6.3.

2.7 What we have learned

In this chapter we have gained information on fundamentals of two dimensional electron systems regarding formation and also magneto transport properties of these systems at low temperature and perpendicular magnetic field. Besides SdH oscillations and integer quantum hall effect for convenient single layer systems, magneto inter sub-band (MIS) oscillations due to periodic modulation of probability of the intersubband transitions by magnetic field as the different Landau levels of the two sub-bands sequentially come in alignment are also discussed.

Moreover, we get familiar to magneto transport phenomena under microwave irradiation like MIRO and ZRS with relevant mechanism describing the phenomena are also provided.

Finally, phonon induced resistance oscillations followed by fundamentals of magneto thermopower measurements in 2D systems have been introduced in order to provide us with the basic knowledge needed for understanding of our studies in Chapter 6.

Chapter 3

Sample preparation and experimental details

Contents

3.1 What we want to know

- How have samples been prepared for experimental measurements?

- What are our measurements methods and which facilities are used in our studies?

3.2 Samples

3.2.1 Structure of Samples

The samples used in our studies are grown by our collaborator in Institute of Semiconductor Physics of Novisibirsk, Russia, by Prof. Dr. A. K. Bakarov. The method exploited for fabrication of two dimensional electron gases (2DEGs) is Molecular Beam epitaxy (MBE) in which crystals are grown one atomic layer at time and it is possible to have control over the composition of each layer. Fig. 3.1, represents a schematic of a MBE system. The structure of our double

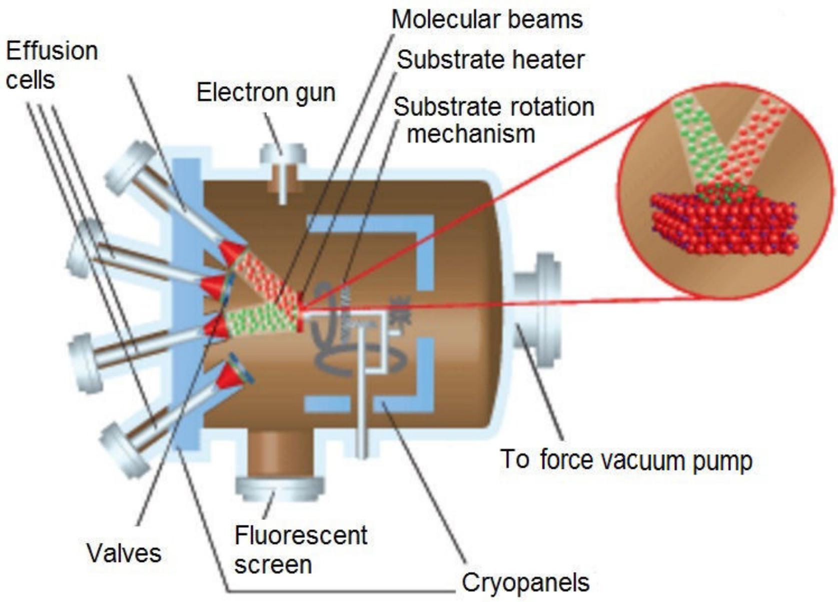

Figure 3.1: Schematic of a different parts of a MBE machine. (Figure adapted from $http://en.rusnano.com$)

quantum well samples, consists of different layers with thickness of each layer shown in Å, is presented in Fig. 3.2. An approximation of conduction band structure of the sample is also presented beside the structure of the sample in the same figure. In the following, a summary

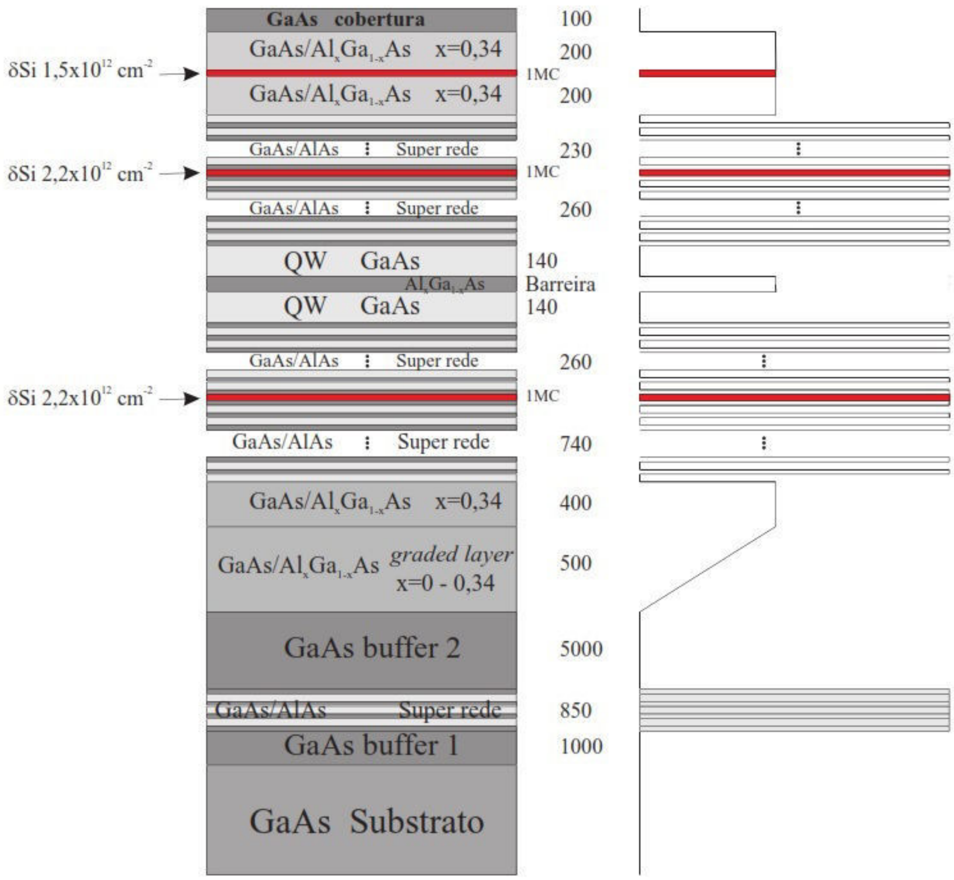

Figure 3.2: Schematic of layer structures of DQWs samples, used in this thesis with different layer thickness shown in Å (left). The approximation of conduction band structure profile of the sample(right)(Figure adapted from (Mamani, 2009)).

of different layers with the reason of their growth, from the substrate to the surface of the samples, is described.

Substrate of $GaAs$ with crystal orientation (100).

A layer of $GaAs$, which is called buffer and is grown in order to obtain more uniform deposition of the following layers and to have smoother surface of the sample.

A superlattice of $GaAs$ and $AlGaAs$ formed a barrier to avoid the migration of impurities of the substrate to our interest layer which in this case is DQW.

A layer of $GaAs$, the second buffer is presented in order to reduce the roughness of the surface and lead to more isolation of the layer of interest.

A layer of $Al_xGa_{1-x}As$, with x linearly varies between $x = 0$ and $x = 0.3$, called graded layer, to avoid the migration of electrons of first silicon δ doped layer to the $GaAs$ layer described above. In this way it is prevented to have electron accumulation in that region, in contrast a conducting channel is formed outside the layer of interest. Moreover, the gradual variation of Al concentration preserves the uniformity of the growing surface. High concentration of Al can produce rougher layers.

A layer consists of $GaAs - AlGaAs$, called the interior barrier, prevents the migration of electrons from the following δ doped silicon layer to the graded layer described above. The layers afterward can be considered to have influence in the structure of the layer of interest which is DQW, in the sample shown in Fig. 3.2.

First δSi doping is done in a mono-layer of $GaAs$ with the aim to use the electrons of Si to fill the quantum wells in the layer of interest.

First superlattice of $GaAs - AlGaAs$ which is called a spacer layer that separates the layer with Si from the first quantum well.

The first quantum well of $GaAs$, which is far from the surface of the sample.

A potential barrier of $Al_xGa_{1-x}As$, that separates the QWs.

The second quantum well of $GaAs$ which is closer to the surface of the sample.

Second superlattice of $GaAs - AlGaAs$, which is called the spacer layer and separates the second layer doped with Si (the following layer) from the second quantum well.

Second δSi doped, equal to the first one, with the main objective of using Si electrons to fill the quantum well in the layer of interest.

A superlattice of $GaAS - AlGaAs$, to prevent the migration of electrons of the second δSi doped layer to the surface.

A layer of $AlGaAs$ which separates the surface from the region of interest and allows the deposition of of another mono-layer of $GaAs$ with Si.

Third mono-layer of $GaAs$ doped with Si. The objective of growing this layer is to saturate the dangling bonds on the surface, called the states of surface.

A layer of $AlGaAs$ that separates the surface of third mono-layer from the $GaAs$ doped layer. This layer acts as a cap which covers the structure.

Finally, a layer of $GaAs$ is grown to prevent the structure from oxidation.

In this thesis, quantum wells including single quantum wells(QW), wide single quantum wells (WQW), triple quantum wells (TQW) and wide triple quantum wells(WTQW) have been used in our measurements, with the characteristics summarized in Table 3.1. The result of self

Sample	well width (Å)	barrier width (Å)	mobility $\times 10^3$ (cm^2/Vs)	total electron density $\times 10^{11}$ (cm^{-2})
NQW	140	-	612	7
WQW	450	-	1900	9
TQW	100-220-100	20	500	8.5
WTQW	100-450-100	14	400	7

Table 3.1: Summary of some main characteristics of the samples used in this thesis.

consistent calculation for some of the samples used in our measurements are provided in Fig. 3.3.

In DQW and TQW, the barriers dividing the wells are thin enough to have a strong tunnel hybridization of electron states in different wells. As a result, there exist two and three sub-bands with different quantization energies ε_j with $(j = 1,2)$ for DQW and $(j = 1,2,3)$for TQW . Due to the high electron density, all sub-bands are occupied by electrons in all investigated samples.

Moreover, as mentioned in §.2.4.1 in coupled quantum wells the linear combination of wave functions in each well leads to a symmetric-antisymmetric energy gap of $\triangle_{SAS} = \varepsilon_{AS} - \varepsilon_S$, which strongly depends on the width and height of the potential barrier. For small thickness of barrier the separation will increase.

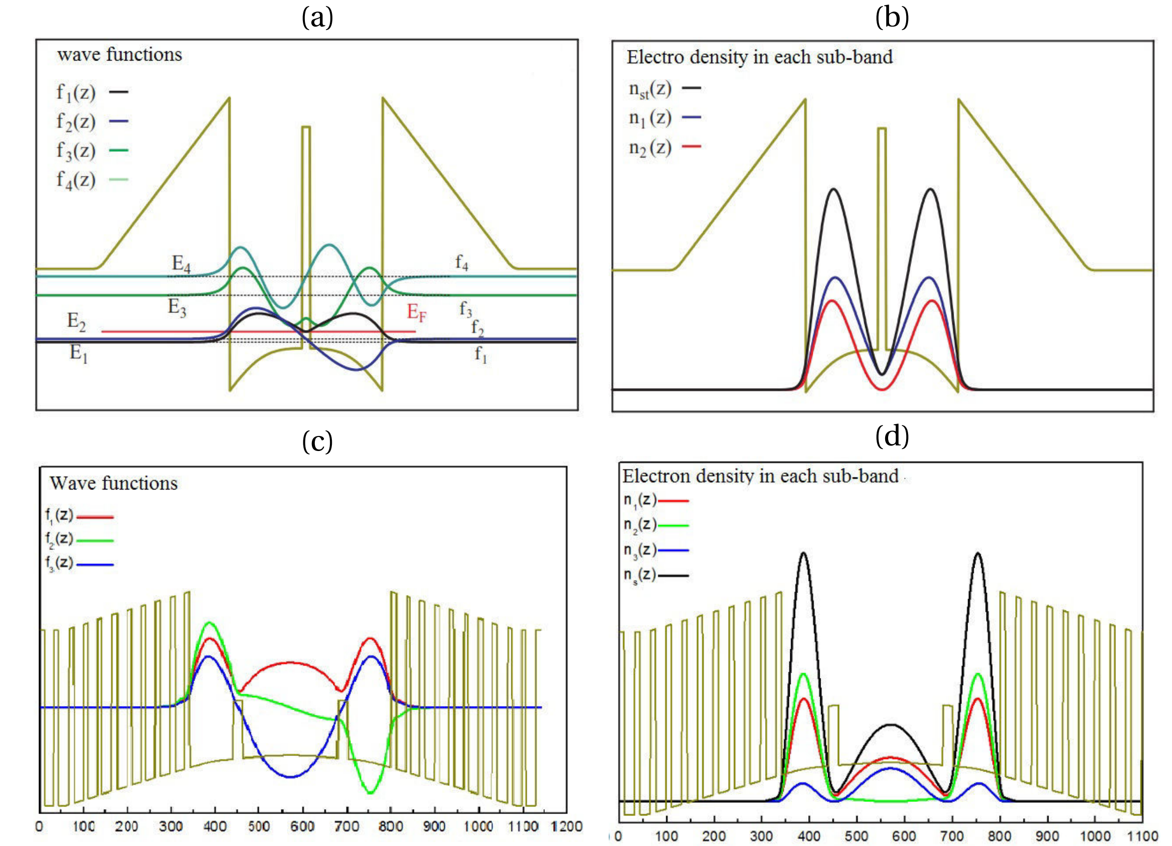

Figure 3.3: The results of self consistent calculations for DQW (first row) with wells width of 140 Å and barrier thickness of 14 Å and TQW (second row) with side wells width of 100 Å, central width of 450 Å and barriers thickness of 14 Å. (Figures adapted from (Mamani, 2009))

Owing to charge redistribution, WQWs with high electron density form a bilayer configuration, i.e. two wells near the interfaces are separated by an electrostatic potential barrier and two sub-bands appear as a result of tunnel hybridization of 2D electron states (symmetric and antisymmetric), which are separated in energy by $\triangle_{SAS}$.

Using the same method, the electronic wave functions in each sub-band and also electron density are calculated for some of our samples. The results of FFT analysis extracted from magneto-resistance oscillations, are presented in Fig. 3.4.

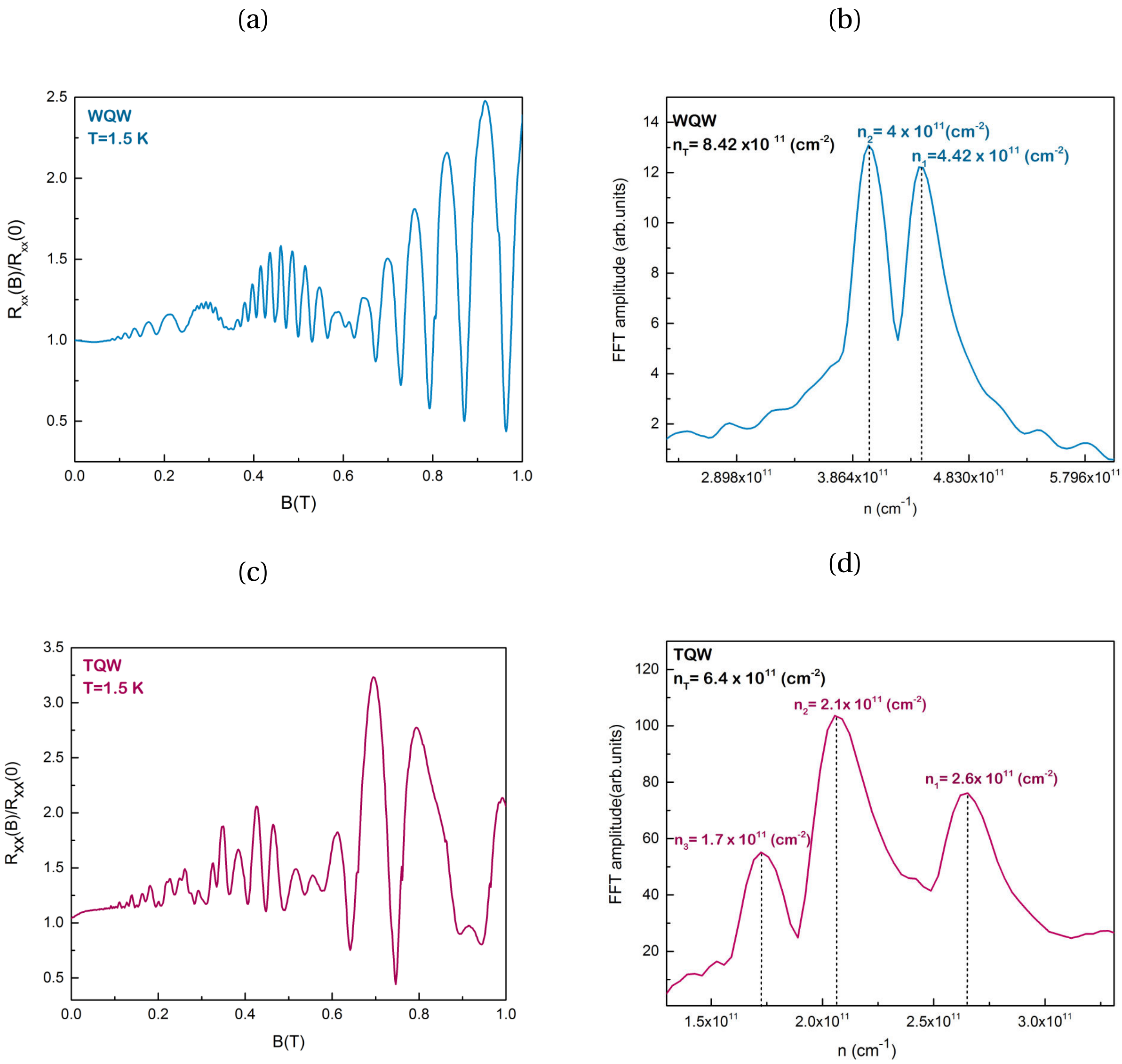

Figure 3.4: Magnetoresistance and FFT analysis for wide quantum well (WQW) sample (a, b) and triple quantum well sample (c,d).

3.2.2 Sample process

In order to carry out the transport measurements on the samples, it is necessary to pass the current through the samples and measure the potential difference in different points of the samples. In this way, one needs to put ohmic contacts on the sample and also introduces a limited region on the sample where the current can pass through it. Therefore, the grown samples are needed to processed and be prepared for transport measurements.

One of the standard procedures to create the appropriate region for current flow is to introduce the Hall bar on the sample via photo-lithography process. The designs of one of the Hall bars, we have created on our samples are shown in Fig. 3.5. The Hall bar shown in Fig. 3.5 has six well defined regions which are indicated as contacts. In usual local measurements, we pass current through the main channel of the Hall bar (Contacts 1 and 2) which are called the current contacts and measure the potential difference between voltage contacts 3 and 4 (or 5 and 6) for longitudinal case and between contacts 3 and 5 (or 4 and 6) for determination of Hall voltage.

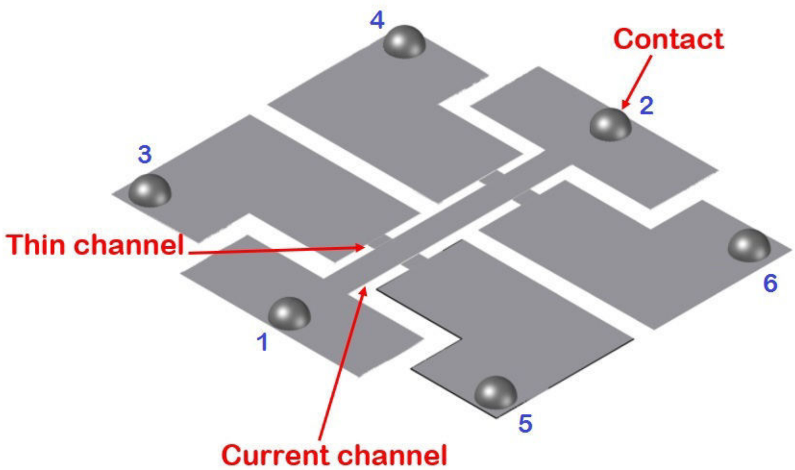

Figure 3.5: Sketch of the Hall bar structure with the contacts 1 to 6 specified. The current channel and also thin channels which connect the main channel to voltage contacs are depicted.

The area of study is the rectangular part in the main channel which is limited by thin channels connecting the current channel to voltage contacts. The process of introducing the Hall bar on the samples are demonstrated in Fig. 3.6.

After growing the samples, first we clean the samples in order to remove all possible impurities from the sample. Then the surface of the samples is covered uniformly by a particular photo-resist. We have used AZ5214 for our samples. Using a mask with the specific Hall bar structure, the desired pattern is introduced on top of the samples covered by the photo-resist via a flux of ultraviolet radiation. One needs to find the optimum exposure time and intensity to have a well defined Hall bar on the samples.

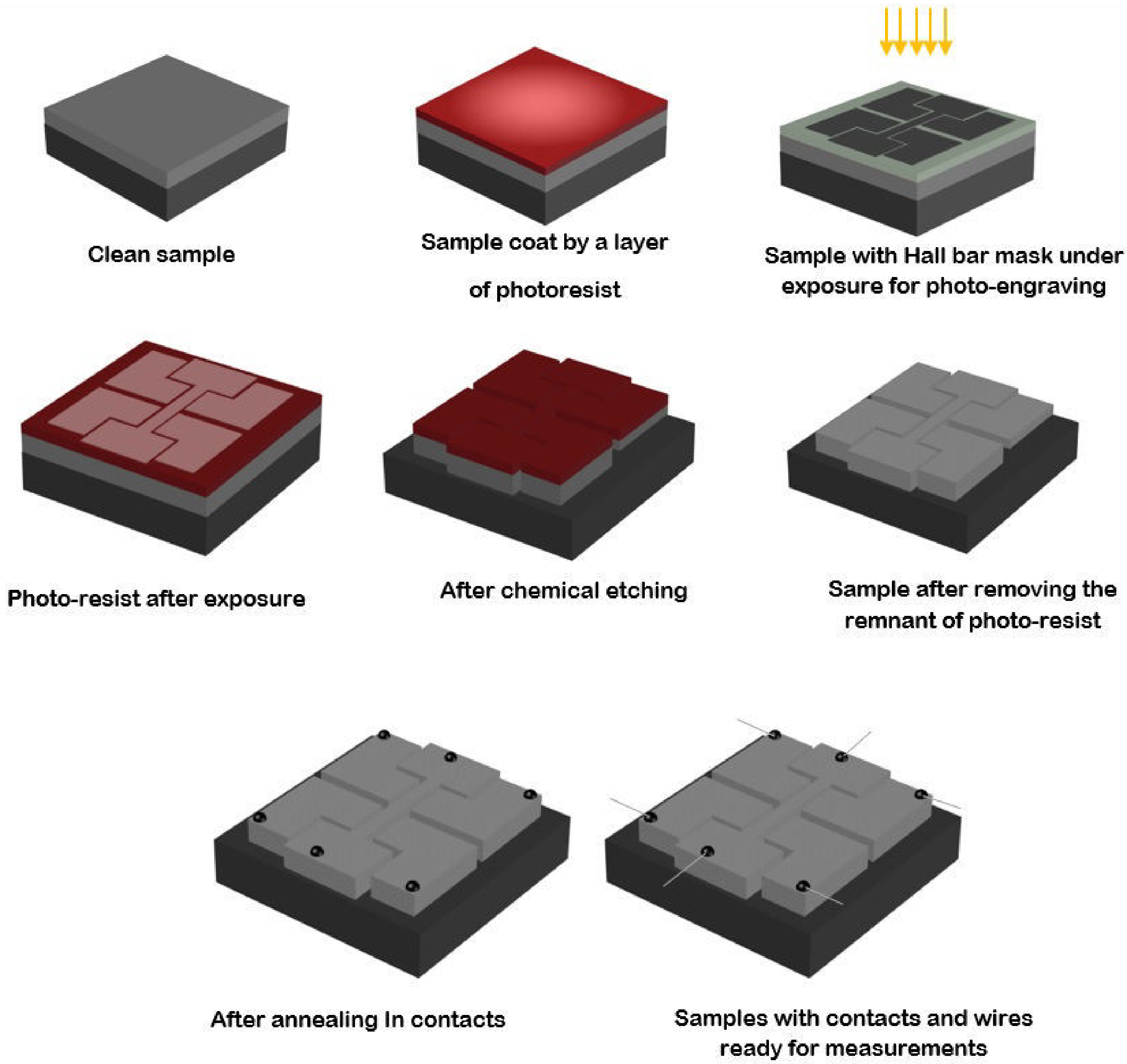

Figure 3.6: Steps of preparing sample for measurements through photo-lithography.

The photo-lithography process followed by wet etching of the samples in appropriate solution, make the samples ready for putting contacts. We have annealed Indium ohmic contacts on our samples at 410 $^{\circ}C$. By attaching the wires to sample and located them in proper probe, sample are ready to be located in magnetic filed for transport measurements. The steps of sample processing from introducing Hall bar to inserting the probe with sample on it are presented in Fig. 3.7.

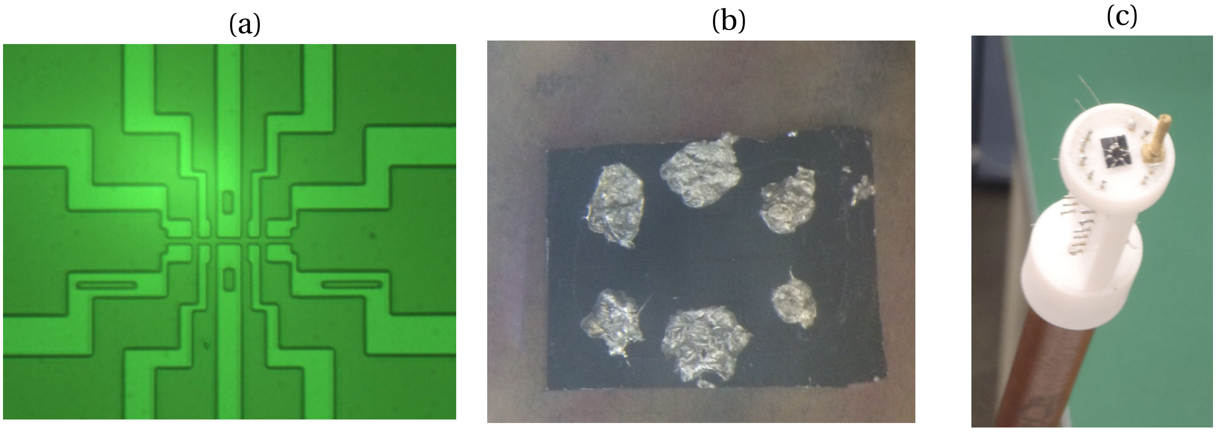

Figure 3.7: The steps of preparing sample for transport measurements (a) Hall bar introduced by phototlithography, (b) Indium contacts annealed on sample with Hall bar structure and (c) sample with wires on the probe ready to insert to crysotat.

3.3 Basic Equipment to study the magneto-transport in low temperatures

3.3.1 Cryogenics

In order to study the quantum transport of electrons, low temperatures and high magnetic fields are the most important factors, needed to be achieved to start the measurements, because it is at these conditions that the observations of quantum effects are possible.

In our group at Laboratory of new semiconductor material (LNMS), we have a cryostat with a superconductor coil to produce magnetic field. The coil is immersed in a bath of ^{4}He. The superior part of the cryostat can be changed which makes it possible that the systems be used as a Variable Temperature Insert (VTI) cryostat. It is also possible to use the ^{3}He as cryogenic in our lab. However, within this thesis, the ^{4}He-cryostat with a top loading VTI which enables measurements between 1.4 K and 300 K up to 17 T, have been used. Fig.3.8 represents the cryostat in our lab along with the schematics of VTI cryostat used for the measurements. The different chambers and needle valve are shown in the figure.

The main chamber which contains liquid ^{4}He has been isolated via a chamber of vacuum , surrounded by a exterior chamber containing liquid N_2 allowed the temperature limit to 77 K and finally the external vacuum chamber which makes the system thermally isolated from the ambient.

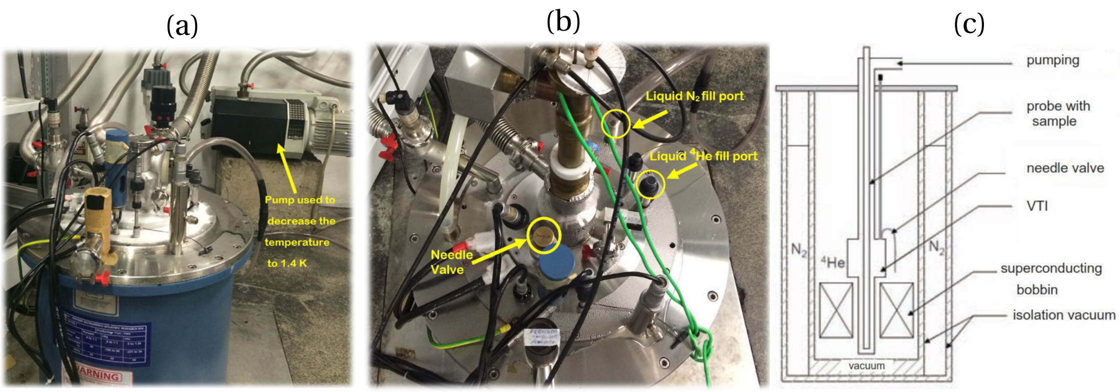

Figure 3.8: The VTI cryostat used in this thesis for the measurements (a), Top view of the cryostat with ^{4}He and N_2 fill port defined (b) and schematic of the VTI cryostat (c).

In ^{4}He bath cryostat with a top loading variable temperature insert (VTI), the properties of temperature and pressure of liquid ^{4}He are used. The samples located in a probe is cooled down by thermal conduction through the ^{4}He exchange gas. A needle valve controls the flow of liquid ^{4}He form the main bath to the VTI. In order to decrease the temperature, the vapor in the VTI is pumped and temperatures down to 1.4 K are possible with our system. Below 2.172 K, ^{4}He becomes super fluid and the effectiveness of pumping decreases rapidly. This is the reason why this system allows not to acquire very low temperatures. More details about low temperature physics and related techniques are provided in Ref.(Enns and Hunklinger, 2005).

3.3.2 Superconducting coil

To create the magnetic field , superconducting coils, located in a chamber with the bath of ^{4}He, are used. In the absence of any pumping system the temperature of the bath is 4.2 K. The superconductivity of the coils make the resistance free current flow without any energy dissipated, possible through the coils and produce a magnetic field. The coils are made of Niobium-Titanium wires wrapped in a copper matrix. The coils of our cryostat are allowed to create the magnetic fields up to 15 T with VTI system and with the normal ^{4}He. However, our coils are always used to produce magnetic fields up to 12 T to avoid the quenching effect in which the superconducting wires transform to normal conductors that lead to the heating via Joule effect. Therefore, the manifestations of the quenching , especially in magnetic systems cooled by liquid ^{4}He, is accompanied by the evaporation of liquid ^{4}He.

3.3.3 Measurement technique

In transport measurements the voltage or resistance is measured as a function of different parameters like magnetic field, temperature, etc. and can be with and without microwave irradiation. The measurements of small signals which is always superimposed on noise, needs the improvement of Signal to noise ratio (SNR). In this way, lock in technique is widely used in transport measurements. This technique makes the measurements of a signal amplitude in a noisy environment possible based on the modulation of the excitation current and a subsequent detection of the voltage drop at the modulation frequency. At low temperatures it must be avoided that the applied current heats the system (2DEG), therefore the measured voltage should not exceed the thermal excitation $V < k_B T/e$.

Lock-In amplifiers are also known as phase sensitive detectors. The alternative currents (AC), especially in the mK-range, are in the order of 10 nA to 1.0 μA. To improve the SNR further, low-noise preamplifiers have been used.

In our measurements depending on the sample quality we have used different resistance from 100 kΩ to 1 MΩ and the excitation voltage, V_{AC}, between 1 to 2 V are used for most of our measurements.

Microwave measurements

Since we have carried out most part of our experiments in the presence of the MW irradiation, a brief description on techniques and necessary equipments are provided in the following. More details about microwave engineering can be found in (Pozar, 1998).

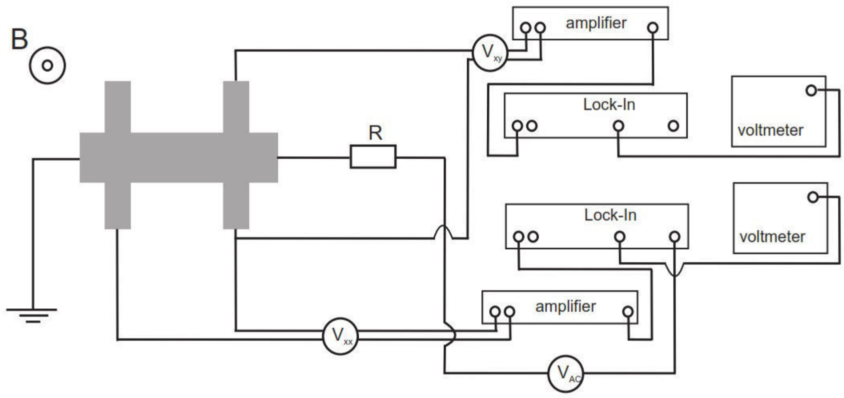

Figure 3.9: Sketch of a typical transport measurement presented in this thesis (Figure adapted from Wiedmann (2010))

Microwave generators

Microwaves are a form of electromagnetic radiation with wavelengths ranging from one meter to one millimeter with the frequencies between 300 MHz and 300 GHz. Our disposal frequency for the measurements of this thesis is from 110 GHz to 170 GHz. The MW sources are backward wave oscillators (BWO), also called carcinotron or backward wave tubes. In principle, this generator is a vacuum tube that is used to generate microwaves up to the THz range. Carcinotron generators belong to the traveling-wave tube family with a wide electronic tuning range.

The generator used in this thesis is G4402E Sweep Generators from Elmika equipped each with an attenuator (see Fig. 3.10) in order to change the MW power from no attenuation (0 dB, highest MW power) to full attenuation (-75 dB, no MW power).

(a) (b)

Figure 3.10: MW generatore Elmika G4402E (a) and MW attenuator (b) used in this thesis.

The technical data of the generator used during this thesis, the frequency range, power range and rectangular output are presented in Table 3.2.

Generator	Frequency range (GHz)	Power range (mW)	Output area (mm^2)
G4402E	110-170	10-35	WR-6 (1.62×0.82)

Table 3.2: Characteristics of the MW generator used in this thesis.

Microwave power and attenuation

In general, MW power (in mW) at the output of the waveguide can be calculated by taking into account the losses of attenuation and waveguide for each frequency. For our generator, we have a different MW power for each frequency without attenuation (0 dB). Tables, provided by Elmika can be used to estimate the MW power (in mW) at the end (output) of the waveguide.

Within this thesis, we use for power-dependent measurements in experiments the value of the attenuation (attenuator) in decibel (dB) which we translate in a MW electric field after our calculation or fitting procedure.

Experimental setup with MW irradiation

In order to deliver MW irradiation from the source down to the sample, we have used rectangular waveguide. The advantage of using a waveguide over coaxial cables is a high power handling capability and lower loss rate. An image of the experimental setup is presented in Fig. 3.11 starting from a MW source equipped with an attenuator. This construction provides a minimal damping of the MW power.

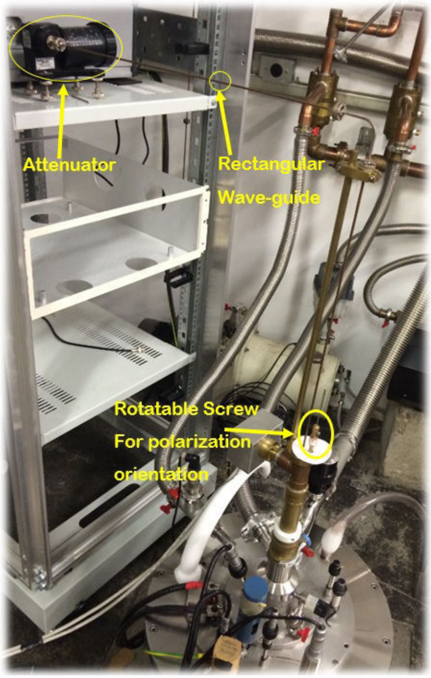

Figure 3.11: Setup for MW experiments MW generator, attenuator and waveguide.

We expose the samples to linear polarization using a special construction of a brass inset which is placed at the end of the waveguide. The possibility of linear polarization enables us to prove microwave effects which are sensitive to linear polarization. The sample for all measurements is placed 1-2 mm away from the end of the wave-guide (Faraday configuration).

For measurements with linear polarization, the orientation of the linear polarized MWs is kept constant while using a special probe (see Fig. 3.11) the orientation of the sample holder (with the sample) is changed from $\theta = 0^\circ$ to $\theta = 90^\circ$.

Moreover, since the output of wave-guide is rectangular, for measurements with linear polarization, the MW flux on the surface of the sample is different for different orientations. Thus, a constant MW electric field is controlled by a constant damping of Shubnikov-de Haas (SdH) oscillations.

3.4 What we have learned

This chapter have described the fundamentals necessary for subsequent experiments in the following chapters regarding the samples structure, processes to make them ready for measurements and techniques required for transport measurements. The essential techniques and facilities for measurements under microwave irradiation are also described.

Besides, some information related to the sample characteristics like electron density, mobility are also provided. Using FFT analysis the electron densities of the samples used for the following measurements are presented. The same method can be used to derive the electron energy in each sub-band for both 2D single layer and multilayer electron systems.

In the following chapters we are going to apply the methods to carry out our desired experiments. In some cases like studying the magneto-thermopower some part may need to be changed, however, the basics are already explained.

Chapter 4

Nonlinear transport & oscillating magnetoresistance in triple quantum wells

Contents

THE nonlinear behavior of low-dimensional electron systems attracts a great attention due to its fundamental interest as well as for potentially important applications in nano-electronics. In response to ac and dc bias, strongly nonlinear electron transport that gives rise to unusual electron states has been reported in two-dimensional systems of electrons in high magnetic fields. It is known that Ohm's law, ($R = V/I$), represents the linearity of transport where the current through a conductor, I, between two point is directly proportional to the voltage across the two points, V. When in a system this proportionality is not obeyed, it enters the nonlinear regime of transport.

The non-linearity of two dimensional electron systems under perpendicular magnetic field is studied extensively. The first studies are associated to breakdown of quantum Hall effect due to application of high current which increases the temperature of the lattice (Cage et al., 1983).

The principal results of the studies represent the appearance of new kind of oscillations after applying the magnetic field or electric current and the decrease in the resistance in the presence of applied electric current up to moderate currents. These are quantum phenomena, caused by the quantization of Landau levels of electronic states (Yang et al., 2002; Bykov et al., 2005).

The observed oscillation effects can be explained by the modification of electronic spectrum in the presence of Hall field (Yang et al., 2002; Zhang et al., 2007; Lei, 2007), while the resistance decrease is associated to the modification of electronic diffusion in energy space that leads to consideration of non-equilibrium part of distribution function. The both phenomena are described in a theory by Vavilov et al. (2007).

The present interest in studying nonlinear transport in 2D systems is stimulated by the observation of two important phenomena. First, there appear oscillations of the resistance as a function of either magnetic field or electric current (Yang et al., 2002; Zhang et al., 2007a,b; Bykov et al., 2005). Second, the current substantially reduces the resistance even at moderate applied voltages (Zhang et al., 2007a,b, 2009) .

The oscillating behavior is a consequence of the geometric resonance in the electron transitions between the tilted Landau levels when the diameter of the cyclotron orbit becomes commensurable with the spatial modulation of the density of states (Yang et al., 2002; Zhang et al., 2007; Lei, 2007). The decrease in the resistance is governed by modification of electron diffusion in the energy space, which leads to the oscillating non-equilibrium contribution to the distribution function of electrons (Dmitriev et al., 2005). A theory describing both these phenomena in a unified way (Vavilov et al., 2007; Khodas and Vavilov, 2008) shows that the existence of the oscillations requires the presence of a short range scattering potential to enable efficient back-scattering. The decrease in the resistance, in contrast, occurs for an arbitrary scattering potential. Experimental investigations of this phenomenon (Zhang et al., 2007, 2009) strongly support the theory (Dmitriev et al., 2005; Vavilov et al., 2007; Khodas and Vavilov, 2008) predicting nontrivial changes in the distribution function as a result of dc excitation under magnetic fields. Nevertheless, further studies are necessary for better understanding of the physical mechanisms of this nonlinear behavior.

In this chapter the results for samples of triple quantum well (TQW) are presented for the first time. After a brief introduction to samples which have been investigated, we present our results which exhibit current dependence and also temperature dependence of magneto-resistance. The comparisons between observed results and theory are also presented. Moreover, negative magneto-resistance behavior is also observed for sample of TQW and WTQW with mesoscopic Hall bar structure. Current dependence and also temperature dependence measurements have been carried out on the sample and the results are described according to the existing model.

4.1 What we want to know

- What are the manifestations of nonlinear transport in magneto-resistance of TQWs ?
- What are the differences of observed behavior for samples with different hall bar size ?
- How the generalized theoretical model for nonlinear transport can be applied to describe the observed experimental results ?

4.2 Triple Quantum wells: Samples and Properties

The samples used for the measurements are symmetric triple quantum wells of $GaAs$ with width of 10 nm of side wells and 22 nm of central well, separated by $Al_xGa_{1-x}As$ ($x = 0.3$) barriers of 2 nm width. Total electron density and mobility of samples at T = 1.5 K are $n_s = 6.4 \times 10^{11}\ cm^{-2}$ and $\mu \simeq 3.2 \times 10^5\ cm^2/V.s$, respectively. The electron densities in each sub-band and the sub-band separations are calculated according to FFT analysis of longitudinal magneto-resistance measurements, as depicted in Fig. 4.2 and the results of calculations for TQW and WTQW are summarized in Table 4.1. However, we have used the results of measurements related to TQW for nonlinear studies, since they show more pronounced MIS oscillations necessary to study the nonlinear effects in magneto-resistance.

Table 4.1: Extracted electron densities and energy gaps by FFT analysis of magneto-resistance oscillations at T=1.5 K

Sample	$n_1 \times 10^{11}(cm^{-2})$	$n_2 \times 10^{11}(cm^{-2})$	$n_3 \times 10^{11}(cm^{-2})$	$\triangle_{12}$ (meV)	$\triangle_{23}$ (meV)	$\triangle_{13}$ (meV)
TQW	2.64	2.06	1.71	2.1	1.2	3.3
WTQW	4.05	3.23	2.03	4.31	2.49	7.25

Moreover, two different types of Hall bar have been introduced to our samples. The one with dimensions of $l \times w = 500\,(\mu m) \times 200\,(\mu m)$, will be considered as macroscopic Hall bar and the other one with dimensions of $l \times w = 100\,(\mu m) \times 5\,(\mu m)$ will be called mesoscopic Hall bar in the following of this chapter. Comparing device size with the relevant length scales, here, mean free path of electrons (few microns) reveals the reason of calling the Hall bars in this way. In case of macroscopic Hall bar, device size is larger than the length scale so the transport can be explained classically, while for mesoscopic one, the two lengths are in the same order and transport is in both the diffusive and ballistic regimes.

4.3 Experimental method & observations

4.3.1 Magneto inter-subband oscillations in TQW

In this section the applicability of the generalized theory for N layer 2D systems presented in §. 2.4.2 is demonstrated for triple quantum wells with three occupied 2D subbands. Fig. 4.1 represents the symmetric triple well structure under investigation.

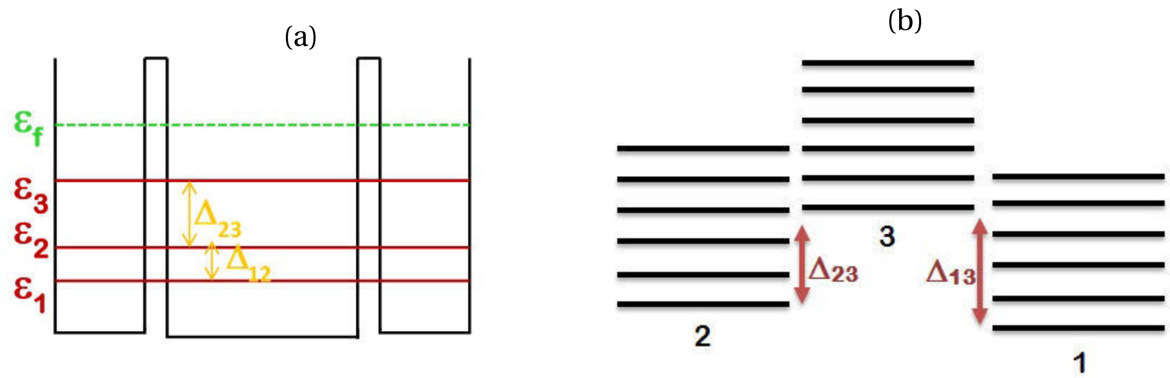

Figure 4.1: (a) TQW configuration for the samples used in this thesis with three 2D occupied subbands and (b) Landau level staircase with corresponding gaps.

Since the barrier between the wells are thin enough, there exist three subbands with different quantization energies of ε_j $(j = 1,2,3)$ due to strong tunnel hybridization.

As respects to the high electron densities in our samples, all sub-bands are occupied by electrons.

The electron densities and subband separation energies, $\triangle_{ij} = |\varepsilon_i - \varepsilon_j|$, derived from FFT analysis are presented in the inset of Fig. 4.2(a). It is also possible to derive the subband separation energies comparing the theoretical magneto-resistance in Eq. 4.5 with the experimental results.

Exploiting the tight-binding Hamiltonian (Hanna and MacDonald , 1982), electron wave-functions and energies, necessary to describe the scattering rates can be found. Expansion of the wave-function in the basis of single well orbitals $F_j(z)$ (i=1,2,3 corresponds to the left, center and right well respectively), leads to

$$\begin{pmatrix} \varepsilon_1^{(0)} - \varepsilon & -t_{12} & 0 \\ -t_{12} & \varepsilon_2^{(0)} - \varepsilon & -t_{23} \\ 0 & -t_{23} & \varepsilon_3^{(0)} - \varepsilon \end{pmatrix} \begin{pmatrix} \varphi_1 \\ \varphi_2 \\ \varphi_3 \end{pmatrix} = 0, \tag{4.1}$$

with $\varepsilon_i(0)$ the single-well quantization energies and $t_{ii'}$ the tunneling amplitudes. For symmetric TQW where $\varepsilon_1^{(0)} \equiv \varepsilon_3^{(0)} \equiv \varepsilon_s, \varepsilon_3^{(0)} \equiv \varepsilon_s$ the subband energies are given by (Hanna and MacDonald , 1982)

$$\begin{aligned} \varepsilon_1 &= \frac{\varepsilon_c + \varepsilon_s}{2} - \sqrt{(\frac{\varepsilon_c - \varepsilon_s}{2})^2 + 2t^2}, \\ \varepsilon_2 &= \varepsilon_s, \\ \varepsilon_1 &= \frac{\varepsilon_c + \varepsilon_s}{2} + \sqrt{(\frac{\varepsilon_c - \varepsilon_s}{2})^2 + 2t^2}, \end{aligned} \tag{4.2}$$

where the corresponding eigenstates in terms of single-well orbitals can be expressed as $\Psi_j(z) = \sum_j \chi_{ij} F_i(z)$. The matrix χ_{ij} is given by

$$\chi_{ij} = \begin{pmatrix} C_1 t/(\varepsilon_s - \varepsilon_1) & 1/\sqrt{2} & C_3 t/(\varepsilon_s - \varepsilon_3) \\ C_1 & 0 & C_3 \\ C_1 t/(\varepsilon_s - \varepsilon_1) & -1/\sqrt{2} & C_3 t/(\varepsilon_s - \varepsilon_3) \end{pmatrix}, \tag{4.3}$$

where $C_{1,3} = [1 + 2t^2/(\varepsilon_s - \varepsilon 1,3)^2]^{-1/2}$.

This matrix consists of the three columns of ϕ_i for the states $j = 1,2,3$. Exploiting the subband separation energies derived from experimental measurements, the parameters of the tight-binding model can be extracted. If ε_s be considered as the reference then one has:

$$\varepsilon_c = \triangle_{23} - \triangle_{12}, \quad t = \sqrt{\frac{\triangle_{23}\triangle_{12}}{2}}, \tag{4.4}$$

For our sample with $d_b = 20$ Å, we obtain $\varepsilon_c = 2.15 meV$ and $2t = 3.2 meV$. Also the total electron density and sub-band energies in are given by $n_s = 6.4 \times 10^{11}\ cm^{-1}$, $n_1 = 2.7 \times 10^{11}\ cm^{-1}$, $n_2 = 1.7 \times 10^{11}\ cm^{-1}$ and $n_3 = 2.1 \times 10^{11}\ cm^{-1}$.

According to the generalized theory of magneto-resistance oscillations for many sub-band systems, described in § 2.4.2, the results of the magneto-resistance for a trilayer electron systems considering the same assumption lead to magneto-resistance results in DQW in § 2.4.2 and by using the simple model of equal electron densities $n_j = n_s/N$, for a trilayer system, $N = 3$, neglecting the SdH oscillations, would be (Wiedmann et al., 2009)

$$\frac{\rho_d(B)}{\rho_d(0)} \simeq 1 + \frac{2}{3}d^2[1 + \frac{2}{3}\cos(\frac{2\pi\triangle_{12}}{\hbar\omega_c}) + \frac{2}{3}\cos(\frac{2\pi\triangle_{13}}{\hbar\omega_c}) + \frac{2}{3}\cos(\frac{2\pi\triangle_{23}}{\hbar\omega_c})]. \tag{4.5}$$

The MIS oscillations are represented as a superposition of three oscillating terms determined by relative positions of the sub-band energies. In Eq. 4.5 transport rates are only standing in Dingle factor d. Moreover, since the electron density in our samples have high total electron-sheet density and a strong tunnel coupling, the approximation in Eq. 4.5 is applicable for estimate to our system.

The results of magneto-resistance oscillations for TQW at T=1.5 K along with FFT analysis at different temperatures are presented in Fig. 4.2.

As mentioned in § 2.4.2, MIS oscillations are more persistent than SdH oscillations at high temperatures. This feature can be observed in amplitude of FFT analysis at different temperatures. While higher peaks associated with SdH oscillations vanish at temperature higher than T=3.6 K, the peaks related to MIS oscillations are still visible at temperatures as high as T=15 K.

(a)

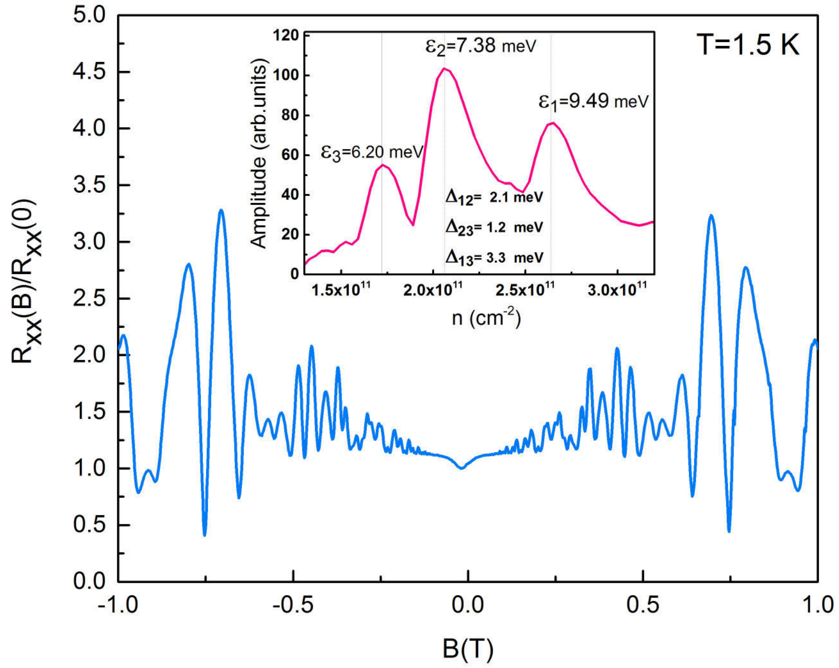

(b)

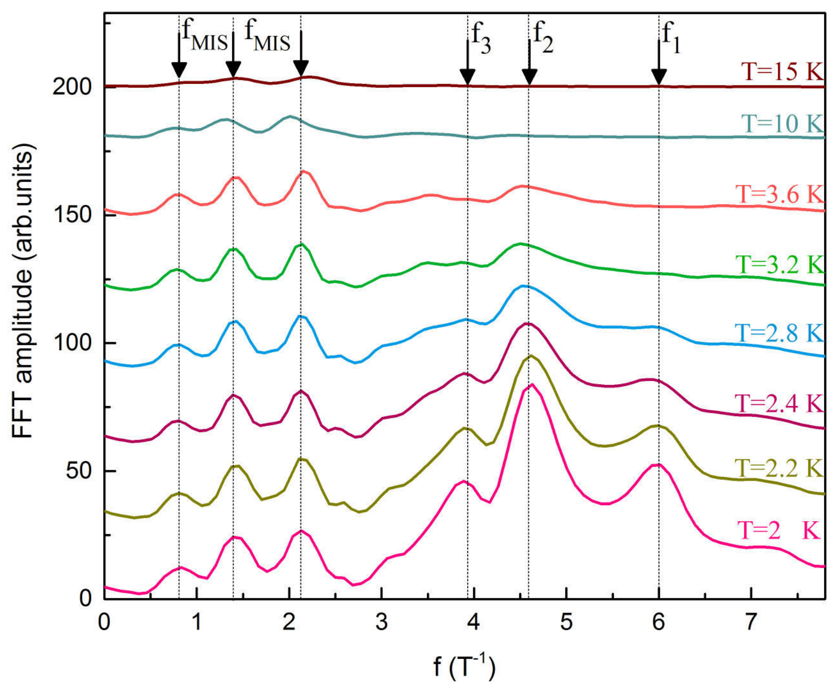

Figure 4.2: (a) Magnetoresistance oscillations of TQW at T=1.5 K. The inset shows FFT amplitude used for calculation of subband energies and electron densities, (b) FFT amplitudes at different temperatures.

The temperature dependence of MIS oscillations are presented in Fig. 4.3. The experiment shows a slow suppression of the MIS oscillations with temperature, which occurs owing to the contribution of electron-electron scattering into Landau-level broadening. Though the theory presented in § 2.4.2 does not take this effect into account explicitly, it can be improved by replacing the quantum relaxation rates according to

$$\nu_j \to \nu_j + \nu_{ee}, \quad \nu_{ee} = \frac{\lambda T^2}{\hbar \varepsilon_F} \tag{4.6}$$

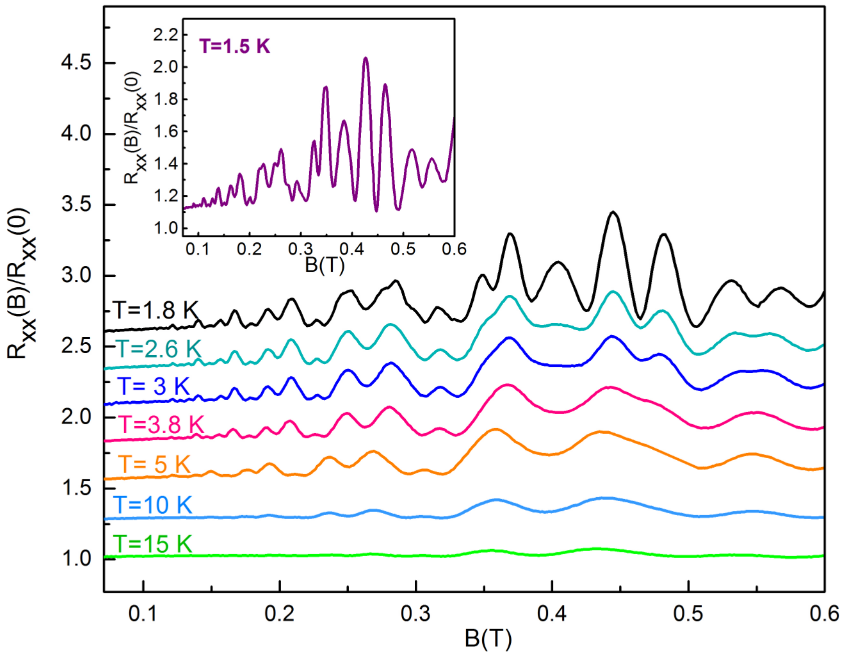

Figure 4.3: Temperature dependence of MIS oscillations in a TQW with $d_b = 2\ nm$ for 1.8, 2.6, 3, 3.8, 5, 10 and 15 K. The inset shows MIS oscillations at T=1.5 K superimposed on low field SdH oscillations.

with ν_{ee} the electron-electron scattering rate (Giuliani and Quinn, 1982; Berk et al. , 1995; Slutzky et al., 1996), ε_F the Fermi energy expressed through the averaged electron density as $\varepsilon = \hbar^2 \pi (n_s/3)/m$ and λ a numerical constant of order unity. In Fig. 4.4(a) a comparison of experiment and theory for two chosen temperatures, T=2.6 and 10 K. We have done this procedure for many temperatures from T=1.5 K up to 15 K, and estimated the ν_{ee} by fitting the amplitude of theoretical and experimental magneto-resistance.

(a)

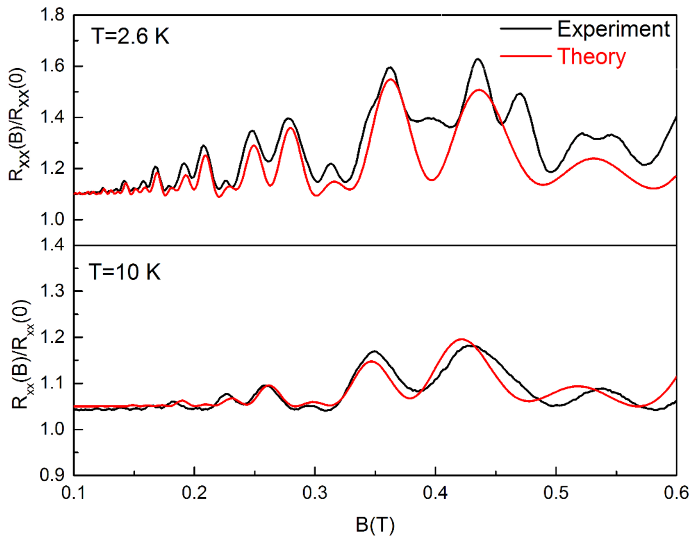

(b)

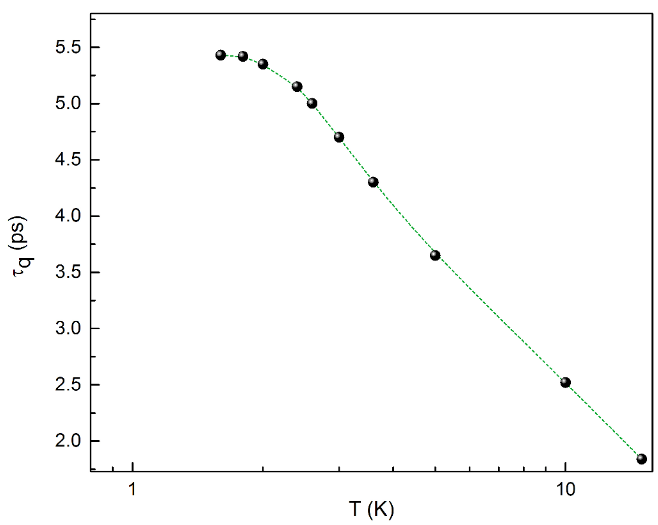

Figure 4.4: (a) Comparison of the experimental and theoretical traces for a TQW with $d_b = 2nm$ at T=2.6 K and T=10 K, (b) Temperature dependence of the quantum lifetime τ_q extracted from the amplitude of MIS oscillations. The green line is a guide to the eye.

From temperature dependence measurements of magneto-resistance between T=1.5 K to T=15 K, the quantum lifetime of electron is extracted by fitting the amplitude of MIS oscillations in Eq. 4.5. The result is shown in Fig. 4.4(b). The quantum lifetime is almost constant for T<2 K and decrease by increasing the temperature which is in agreement with the concept of electron-electron scattering contribution.

4.3.2 Nonlinear measurements results

The magneto-resistance, R_{xx} of samples is measured by using the standard lock-in technique for different applied AC currents with the frequency of 7.43 Hz, at temperatures T=1.5 K and T=4.2 K. The resistance of the samples as a function of magnetic field at different temperatures and currents, for samples with macroscopic Hall bars are presented in Fig. 4.5.

(a) (b)

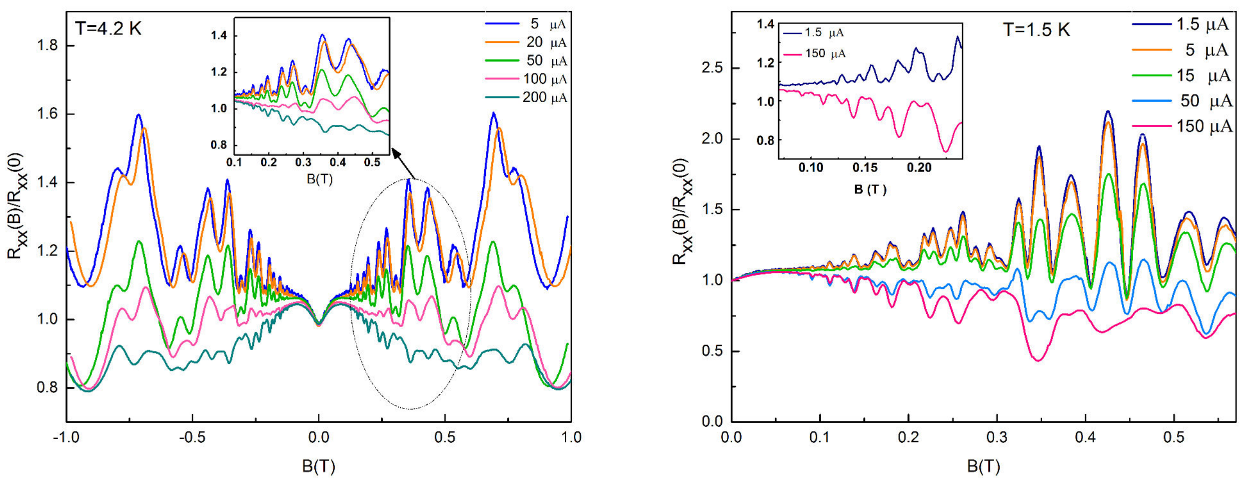

Figure 4.5: Magneto-resistance of TQW samples with macroscopic Hall bar structure for four different currents at (a) T=4 K and (b) T=1.5 K. The inset of figures represent the close look to the region where the linear and nonlinear magneto-resistance occur of both temperatures.

Notably, the magneto-resistance is positive at low currents while increasing the current I, lead to reduction in the amplitude of MIS oscillations until a flip of these oscillation occurs (see Fig. 4.5). This flip, which starts from the regions of lower magnetic fields and extends to higher fields by increasing the current, is related to the inversion of the quantum part of the magneto-resistance from positive to negative. Therefore, one can introduce a current dependent inversion magnetic field, B_{inv}, near which an additional feature that looks like the splitting of MIS oscillation peaks or appearance of the next harmonics of MIS oscillations is observed, however unlike DQW samples (Mamani et al., 2009), this feature is difficult to be recognized in our TQW samples.

Moreover, the amplitudes of inverted MIS oscillations increase with increment of the current and become larger than the MIS oscillation amplitudes in linear regime. Although if the current increases further, the amplitudes of inverted peaks start to decrease as shown in Fig. 4.6. This decrease is faster in regions of lower magnetic fields.

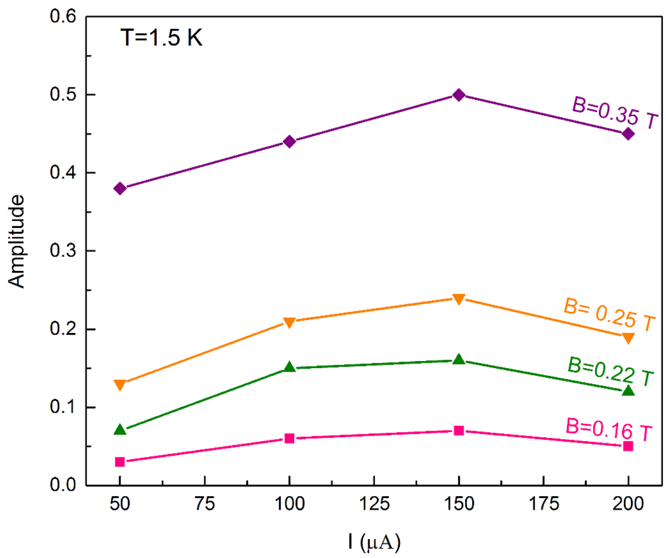

Figure 4.6: The amplitude of inverted peaks of MIS oscillations extrected from magnetoresistance oscillations at B=0.16 T, B=0.22 T, B=0.25 T and B=0.35 T

In contrast to MIS oscillations, the peak inversion does not occur for SdH oscillations, however, due to electron heating by current the amplitudes of these oscillations decrease as the current increases until the SdH oscillations completely disappear in the low field region.

4.4 Theoretical model

The theoretical model describing the application of DC current to two dimensional electronic systems with one sub-band occupied is presented by Dmitriev et al. (2005) in which an oscillatory term is considered in distribution function of electrons. This model is then generalized by Raichev and Vasko (2006) for systems with more than one sub-band occupied.

According to this model, the current changes the isotropic part of electron distribution function, f_ε, whose first derivative enters the expression for conductivity

$$\sigma_d = \int d\varepsilon(-\frac{\partial f_\varepsilon}{\partial \varepsilon})\sigma_d(\varepsilon), \tag{4.7}$$

The quantity $\sigma_d(\varepsilon)$, which is proportional to the squared density of electron states, describes the contribution for electrons with a fixed energy ε. Moreover, the flow of current through the sample effectively develops a diffusion of electrons in the energy space which is reflected by the kinetic equation

$$\frac{P}{D_\varepsilon \sigma_d}\frac{\partial}{\partial \varepsilon}\sigma_d(\varepsilon)\frac{\partial}{\partial \varepsilon} f_\varepsilon = -J_\varepsilon(f), \tag{4.8}$$

where $P = j^2\rho_d$ is the power of Joule heating (the energy absorbed per unit time over a unit square of electron system), j is the current density, ρ_d and D_ε are the resistivity and the density of electron states respectively, and J_ε is the collision integral.

The Eq. 4.7 is solved using a distribution function, $f_\varepsilon = f_\varepsilon^0 + \delta f_\varepsilon$, with the first term varies slowly and the second one rapidly oscillates on the scale of cyclotron energy. The first and second terms satisfy the following equations

$$\kappa\frac{\partial^2}{\partial \varepsilon^2} f_\varepsilon^0 = -J_\varepsilon(f^0), \quad \kappa = \frac{\pi \hbar^2 j^2 \rho_0}{2m} \tag{4.9}$$

where its solution can be satisfactory approximated by a heated Fermi distribution if the electron-electron scattering dominates over the electron-phonon and over the electric field effect described by the left-hand side of Eq. 4.9 and

$$\mathscr{D}_\varepsilon \frac{\partial^2}{\partial \varepsilon^2}\delta f_\varepsilon + 2\frac{\partial \mathscr{D}_\varepsilon}{\partial \varepsilon}\frac{\partial}{\partial \varepsilon}\delta f_\varepsilon + \kappa^{-1} J_\varepsilon(\delta f) = -2\frac{\partial \mathscr{D}_\varepsilon}{\partial \varepsilon}\frac{\partial f^0_\varepsilon}{\partial \varepsilon}, \tag{4.10}$$

that we search for $\delta f_\varepsilon = (\frac{\partial f^0_\varepsilon}{\partial \varepsilon})\varphi_\varepsilon$ with φ_ε periodic function of energy. The dimensionless function $\mathscr{D}_\varepsilon = 1+\gamma_\varepsilon$ is the density of states normalized to its zero filed value, containing an oscillating part, γ_ε, which is periodic in $\hbar\omega_c$. Taking into account that the main mechanism of relaxation of the distribution δf_ε is the electron-electron scattering, the generalized result of Ref. (Dmitriev et al., 2005)obtained by Raichev can be expressed as:

$$J_\varepsilon(\delta f) = -\frac{1}{\tau_{in}}\frac{\partial f^0_\varepsilon}{\partial \varepsilon}\frac{1}{\mathscr{N}\mathscr{D}_\varepsilon}\sum_{jj',j_1j_1'} M_{jj',j_1j_1'}\langle \mathscr{D}_{j\varepsilon}\mathscr{D}_{j_1\varepsilon+\delta\varepsilon}\mathscr{D}_{j'\varepsilon'}\mathscr{D}_{j_1'\varepsilon'-\delta\varepsilon} \times [\varphi_\varepsilon + \varphi_{\varepsilon'} - \varphi_{\varepsilon+\delta\varepsilon} - \varphi_{\varepsilon-\delta\varepsilon}]\rangle_{\varepsilon',\delta\varepsilon}, \quad \mathscr{N} = \sum_{jj',j_1j_1'} M_{jj',j_1j_1'} \tag{4.11}$$

where $\delta\varepsilon$ is the energy in electron-electron collision, $M_{jj',j_1j_1'}$ is the probability of scattering of electrons from the states j and j' to the states j_1 and j_1', $\mathscr{N}$ is the normalization constant and the angular brackets $\langle ...\rangle_{\varepsilon',\delta\varepsilon}$ denote the averaging over the energies ε' and $\delta\varepsilon$.

When the inelastic relaxation time, τ_{in}, describes the relaxation at low magnetic fields, $\mathscr{D}_\varepsilon$ is close to unity and no longer depends on oscillatory term (γ_ε). In this case the relaxation time approximation is justified and the collision integral acquires the simplest form $J_\varepsilon(\delta f) = -\delta f_\varepsilon/\tau_{in}$. The resistivity $\rho_d = \sigma^{(0)}_d/\sigma^2_\perp$, according to Eq. 4.7, is written in the form

$$\rho_d = \rho_0 \int d\varepsilon \mathscr{D}^2_\varepsilon (-\frac{\partial f^0_\varepsilon}{\partial \varepsilon})(1+\frac{\partial \varphi_\varepsilon}{\partial \varepsilon}), \tag{4.12}$$

where it is taken into account that $\frac{\partial f_\varepsilon}{\partial \varepsilon} \simeq \left(\frac{\partial f^0_\varepsilon}{\partial \varepsilon}\right)\left[1+\frac{\partial \varphi_\varepsilon}{\partial \varepsilon}\right]$. Therefore, in order to calculate the resistivity, it is necessary to find ϕ_ε functions that determine the oscillatory part of distribution function and can be expanded in series of harmonics, $\varphi_\varepsilon = \sum_k \varphi_k \exp(2\pi i k\varepsilon/\hbar\omega_c)$. The Eq. 4.10, thus can be represented as a system of linear equations

$$(Q^{-1}+k^2)\varphi_k + \sum_{k'=-\infty}^{\infty}[(2kk'-k'^2)\gamma_{k-k'} + Q^{-1}C_{kk'}]\varphi_{k'} = 2ik\frac{\hbar\omega_c}{2\pi}\gamma_k, \tag{4.13}$$

where

$$Q = \frac{4\pi^3 j^2}{3e^2 n_s \omega_c^2} \frac{\tau_{in}}{\tau_{tr}}, \tag{4.14}$$

is a dimensionless parameter characterizing the nonlinear effect of the current on the transport in triple quantum wells. The matrix $C_{kk'}$ describes the effect of electron-electron scattering beyond the relaxation time approximation and its explicit form is not shown here. At low magnetic fields when $\exp(-\pi/\omega_c\tau)$ is small, one can take into account only a single harmonic ($k = \pm 1$) in the coefficients φ_k which leads to a simple solution $\varphi_{\pm 1} = \pm i\gamma_{\pm 1}(\hbar\omega_c/\pi)Q/(1+Q)$.

Then the Eq. 4.12 for resistivity, ignoring the SdH oscillations, is reduced to

$$\frac{\rho_d}{\rho_0} = 1 + \frac{2}{3}\exp(-2\pi/\omega_c\tau)\frac{1-3Q}{1+Q}\left(1 + \frac{2}{3}\cos(\frac{2\pi\triangle_{12}}{\hbar\omega_c}) + \frac{2}{3}\cos(\frac{2\pi\triangle_{13}}{\hbar\omega_c}) + \frac{2}{3}\cos(\frac{2\pi\triangle_{23}}{\hbar\omega_c})\right) \tag{4.15}$$

The second term in this expression, which is proportional to $\exp(-2\pi/\omega_c\tau)$, differs from a similar terms of the single sub-band theory (Dmitriev et al., 2005) and the double sub-band theory (Mamani et al., 2009) describing the MIS oscillations. The Fermi energy ε_F is expressed as $\varepsilon_F = \hbar^2\pi(n_s/3)/2m$ and is proportional to the total electron density.

4.4.1 MIS peak inversion and inelastic scattering time

The basic features of our experimental findings can be understood within Eq. 4.15. When the parameter Q is small we are in the linear regime and according to this equation we have a good description of MIS oscillation experimentally investigated in Ref. (Wiedmann et al., 2009).

When the current increases, the amplitude of MIS oscillations decreases and the inversion of MIS oscillation peaks occurs. While the amplitude of SdH oscillations are not affected directly by current. However, they start to decrease due to heating effects of current. The flip of the MIS oscillations corresponds to $Q = 1/3$. Since Q is inversely proportional to the square of the magnetic field, there exists the inversion field B determined from the equation $Q = 1/3$, where Q is given by Eq. 4.14.

We have extracted B_{inv} values of different currents and the results are shown in Fig. 4.7.

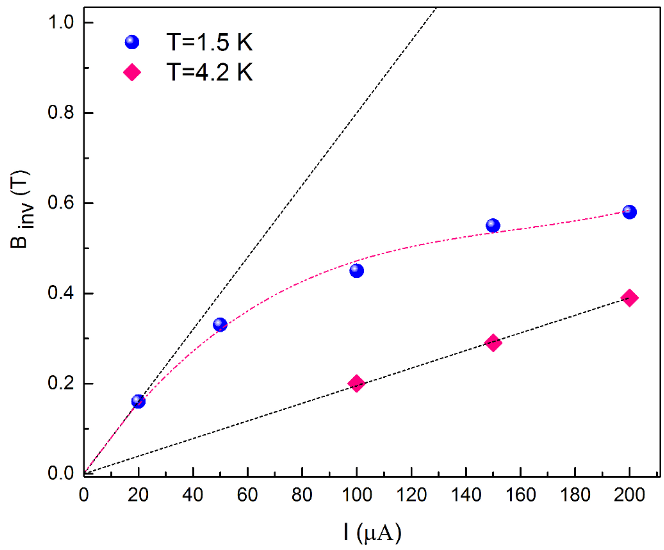

Figure 4.7: Dependence of the inversion magnetic field on the current for TQW sample at T= 1.5 K and T=4.2 K. The dashed lines correspond to a linear $B_{inv}(I)$ dependence assuming $\tau_{in} = 37\ ps$ at T=4.2 K and $\hbar/\tau_{in} = 1.2mK$ at T=1 K. The black dashed lines corresponds to the linear $B_{inv}(I)$ dependence. The red dashed line is for eye guide.

Our findings, resemble the observations in Ref. (Mamani et al., 2009). At 4.2 K the experimental points follow the linear $B_{inv(I)}$ dependence predicted by Eq. 4.14. In Eq. 4.14, the only unknown parameter is the inelastic relaxation time which can be derived from the slope of the experimental data in Fig. 4.7 as $\tau_{in} \simeq 37\ ps$ at T=4.2 K. Assuming the T^{-2} scaling of this time (Dmitriev et al., 2005) , we obtain $\hbar/\tau_{in} = 1.2mK$ at T=1 K. At T=1.5 K, the position of experimental point can be fitted with this picture if the electron heating is taken into account. The current increase lead to increment of electron temperature due to heating effect. If the temperature dependence of τ_{in} be considered, the deviation from the linearity can be explained. When the current becomes high enough ($Q \gg 1$), Eq. 4.15 predicts saturation of the resistance, when the amplitudes of inverted MIS peaks are larger than the amplitudes of the MIS peaks in the linear regime($Q \ll 1$).

However, in our experiments, since we could increase the AC current up to 200 μA, we could not see the features as clear as what observed in case of DQW by Mamani et al. (2009). The saturation effects, can be explained by the effect of heating on the characteristic times. Although the resistivity in the high-current regime ($Q \gg 1$) no longer depends on τ_{in}, there is a sizable decrease in the quantum lifetime τ with increasing temperature (Mamani et al., 2008), which takes place because the electron-electron scattering contributes into τ. As a result, the Dingle factor decreases and the quantum contribution to the resistance becomes smaller as the electrons are heated.

4.5 Negative magneto-resistance in two dimension

The first observation of negative magneto-resistance with parabolic magnetic field dependence for a two dimensional electron gas at low temperature was by Paalanen et al. (1983) which its temperature dependence described theoretically by the electron-electron interaction correction to the conductivity (Houghton et al., 1982; Girvin et al., 1982).

High quality of samples allows one to observe a more pronounced negative magneto-resistance, called huge magneto-resistance (Dai et al., 2010; Bockhorn et al., 2011; Hatke et al., 2012). Moreover, in high mobility 2DEG, beside the huge magneto-resistance, a peak around zero magnetic field is also examined due to an interplay of smooth disorder and macroscopic defects (Bockhorn et al., 2014; Mirlin et al., 2001; Polyakov et al., 2001).

However, the origin of the huge magneto-resistance for high mobility 2DEGs are not fully understood and different scattering event like interface roughness, background and remote ionized impurities affect the huge magneto-resistance and make the theoretical description more complex.

Here, we present the results of current and temperature dependence of negative magneto-resistance for samples of TQW with a Hall bar structure of $l \times w = 100(\mu m) \times 5(\mu m)$.

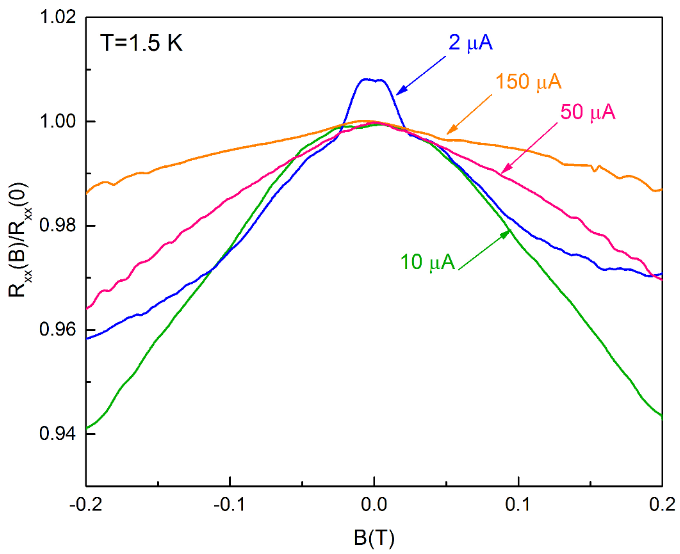

Figure 4.8: The normalized longitudinal magneto-resistance of WTQW for different currens I of 2 μA, 10 μA, 50 μA, 150 μA.

The measurement result of current dependence of longitudinal magneto-resistance around zero field for WTQW samples with mesoscopic Hall bar, are presented in Fig. 4.8 for different current values. According to this figure we observe a huge negative magneto-resistance around zero field in which by increasing current the negative magneto-resistance decreases. Moreover, at small current values (2 μA in this figure) another peak at zero magnetic field, which decreases significantly by increasing the current. Note that the small peak at zero magnetic field is not caused by the interaction between different 2D sub-bands and it also appears for single layer quantum wells.

We also have studied the temperature dependence of TQW samples with mesoscopic Hall bar around zero magnetic field and the results are demonstrated in Fig. 4.9

The negative magneto resistance decreases by increasing the temperature. The small peak at zero magnetic field also observed which is almost independent of temperature. The temperature independence at $B = 0$ is a sign for the absence of weak localization in our sample (Bockhorn et al., 2011).

Furthermore, for low current and low temperature the longitudinal MR becomes nearly

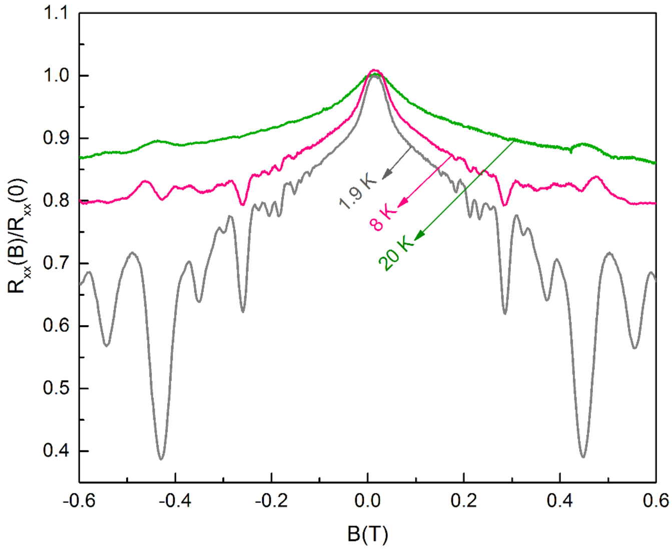

Figure 4.9: The normalized longitudinal magneto-resistance of TQW sample with mesoscopic Hall bar for different temperatures of T=1.9 K, T=8 K and T=20 K.

bell shaped. Also, the strong negative magneto-resistance crosses over to positive magneto-resistance at about 0.6 T for 8 K in TQW samples and 0.2 T for I=2 μA for WTQW samples.

The observed effect can be attributed to the influence of ballistic transport since the mean free path of electrons are comparable with the Hall bar dimension. The zero field peak can be attributed to the scattering at the edges of the geometry of the Hall bars in the ballistic transport regime comparable to the observed in the so called quenching of the Hall effect (Roukes et al., 1987; Thornton et al., 1989). According to the above observations the astonishing huge magneto-resistance is attributed to the high mobility of the 2DEG, the corresponding mean-free path and interaction effects neither weak localization nor the interaction between different 2D sub-bands. However, further investigation is needed to fully understand the origin of the negative magneto-resistance in two dimensional electron systems. Our experimental results are in agreement with the result of experimental work reported in articles (Bockhorn et al., 2011, 2015).

4.6 What we have learned

In this chapter we provide the results of our studies on TQW samples. The first part of the chapter we begin with the MIS oscillations in this system and have tried to extract related parameters like electron densities, energies of each sub-band according to generalized formula for magneto-resistance and FFT analysis of the experimental data.

In the next part we have reported the results of nonlinear magneto-resistance in the presence of AC current. Comparing our observation with the case of DQW (Mamani et al., 2009), we have found similar effects in TQW samples as well. Moreover, the related formula for magneto-resistance in the presence of applied current have been developed for TQW samples according to the generalization of the existing formula for single and bilayer electron systems.

Finally, We have reported our observations of nonlinear effects around zero magnetic field and for the samples with mesoscopic structures. We observed a huge negative magneto-resistance in different applied AC currents and also for different temperatures. Although, the area is still an open field of research and the origin of the observed negative magneto-resistance is still under question, we have tried to describe the observed effects according to some existing models and theories.

Chapter 5

MW-induced nonlocal transport in two dimensional electron systems

Contents

THE experimental observation of microwave induced zero-resistance states (ZRS) in high mobility two dimensional electron systems attracted significant experimental and theoretical interests. The most developed theoretical explanations like *displacement* and *inelastic* mechanisms (see § 2.5.2), rely on scattering mechanisms inside the bulk of 2DEG. Although these theories reproduce certain experimental features, the physical origin of ZRS is still not captured.

Moreover, a striking similarity has been emphasized between the quantum Hall effect (QHE) and ZRS: both effects exhibit vanishing longitudinal resistance, R_{xx}, when the propagation along the sample edge is ballistic. It occurs when the mean free path of electrons, l_e, is much larger than the cyclotron radius, $R_c = v_F / \omega_c$. In 2DEG samples with lower mobility this regime corresponds to strong magnetic fields and therefore the quantum Hall effect is robust against disorder (Buttiker, 1986).

However, microwave radiation stabilizes guiding along sample edges in the presence of a relatively weak magnetic field leading to a ballistic dissipationless transport regime, which also results in vanishing R_{xx} (Chepelianskii& Shepelyansky, 2009; Zhirov et al., 2013). Indeed such transport is much less robust than those in the QHE regime and requires samples with ultrahigh electron mobility.

Since the edge channels play a crucial role for electron transport, we probe the property of the edge states via the method of nonlocal electrical measurement. We attribute the observed non-locality to the existence of edge states stabilized by microwave irradiation in a weak magnetic field and provide a model taking into account the edge and bulk contributions to the total current in the local and nonlocal geometries.

In this chapter, first, the experimental results of non-local measurements is presented. We find a relatively large ($\sim 0.05 \times R_{xx}$) nonlocal resistance in the vicinity of the ratio $j \approx \omega/\omega_c \approx 3.15/4$, with ω the radiation angular frequency, $\omega_c = eB/m^*$ the cyclotron angular frequency and m^* the effective mass of the electrons. The observed non-locality is attributed to the existence of edge states stabilized by microwave irradiation and a weak magnetic field.

In the second part, we provide a model taking into account the edge and bulk contributions to the total current in the local and nonlocal geometries and finally, we discuss on the results derived from the comparison of our measurements and the transport model.

5.1 What we want to know

- How the properties of edge states under MW irradiation can be probed experimentally?
- Which state, bulk or edge, does have the main contribution in ZRS?

5.2 Experimental investigations

For our experimental studies, samples of both narrow (14 nm) and wide (45 nm) quantum wells with high electron density of $n_s \simeq 1.0 \times 10^{12}\ cm^{-2}$ and mobility of $\mu \simeq 1.7 - 3.2 \times 10^6\ cm^2/Vs$ at $T = 1.4\ K$ and after a brief illumination with a red diode, have been used.

We have exploited several devices from the same wafers in our measurements.

As mentioned in § 2.4.1 owing to charge redistribution, WQWs with high electron density form a bilayer configuration in which two wells near the interfaces are separated by an electrostatic potential barrier and two sub-bands appear as a result of tunnel hybridization of 2D symmetric and anti-symmetric electron states, separated in energy by $\triangle_{SAS}$. We have extracted the value of $\triangle_{SAS} = 1.40\ meV$ from the periodicity of low-field MIS oscillation.

In NQW, after illumination, electrons also occupy two sub-bands, however the carrier density of the second sub-band is much smaller than the density of the lower sub-band.

We have measured resistance on two different types of the devices. Device A is a conventional Hall bar patterned structure ($l \times w = 500\ \mu m \times 200 \mu m$) with six contacts for identifying nonlocal transport over macroscopic distances and Device B which is designed for multi-terminal measurements and consist of three 5 μm wide consecutive segments of different length ($5\mu, 15\mu, 5\mu m$), and eight voltage probes. The top view of both devices are shown in Fig. 5.1.

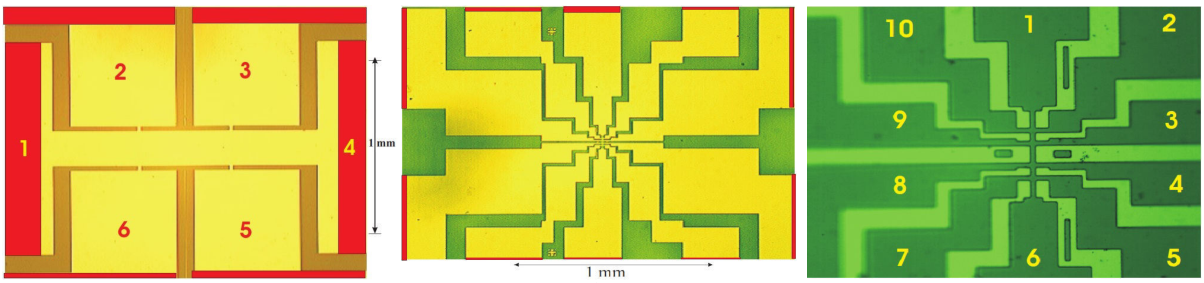

(a) (b) (c)

Figure 5.1: Top view of the central part (yellow region) of (a) device A, (b) device B. The metallic contacts, where the mixing of the electrochemical potential occurs, are shown by the red squares. (c) Zoom of the central part of the device B (dark green region) (Figure adapted from (Levin et al., 2014)).

The formation of edge channels which are isolated from the bulk states lead to observation of nonlocal effects in electronic devices. In order to probe the properties of the edge states, it is necessary to do nonlocal measurements beyond the convention local measurements.

Applying current between a pair of the probes creates a net current along the sample edge which can be detected by another pair of voltage probes away from the dissipative bulk current path (see Fig. 5.2).

The observation of nonlocal transport in quantum Hall systems in the presence of the magnetic field, have confirmed it as a constituting definitive experimental evidence for the existence of edge states in the QH regime. The origin of nonlocal resistance in quantum Hall systems arises from the suppression of electron scattering between the edge channels and the bulk states.

The multi-probe configuration on our sample allows us to study the scale of the observed non-locality and understand better the physics of this phenomenon .

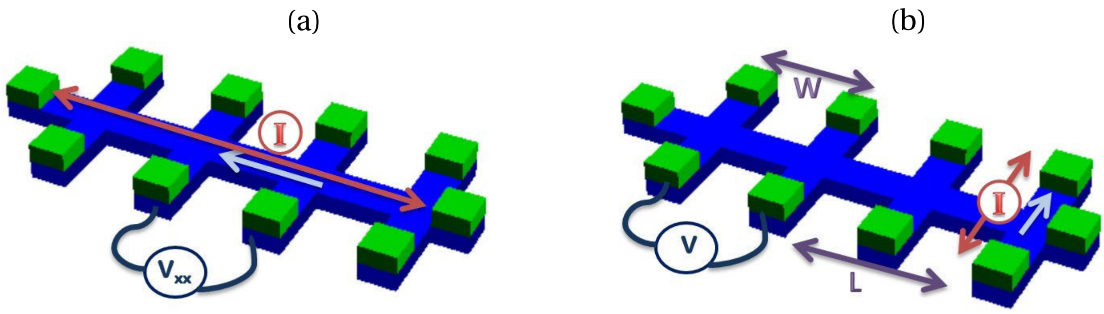

Figure 5.2: Schematic of measurement configurations for (a) local and (b) nonlocal measurements.

A VTI cryostat with a waveguide to deliver the MW irradiation with frequency, 110 GHz$\leqslant f_{MW} \leqslant$ 170 GHz), down to the sample have been used for the measurements.
The results of dark resistance and a ZRS (marked with arrow) for MW irradiation at frequency 144.6 GHz, at T = 1.5 K for both single layer and bilayer Hall bar devices, are presented in Fig 5.3.

In the presence of the microwave irradiation, MIRO appear in NQW and one of the minimums develops into ZRS. Note that the specific MW frequency in which the ZRS developed from the

(a)

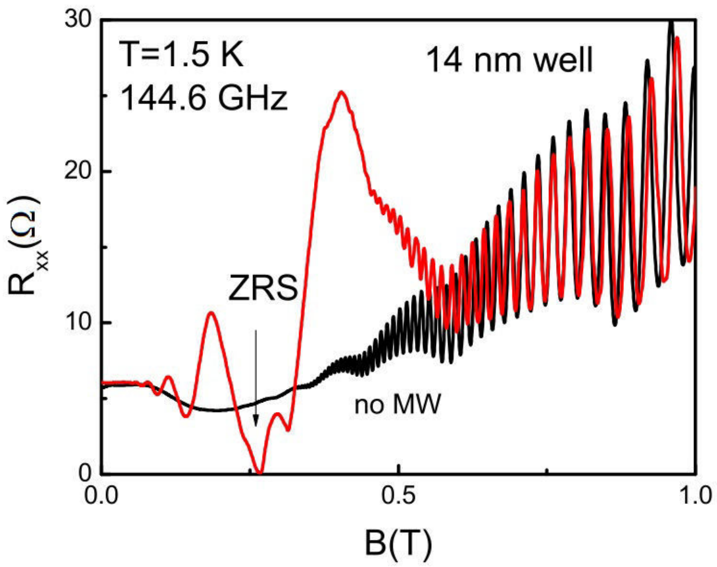

(b)

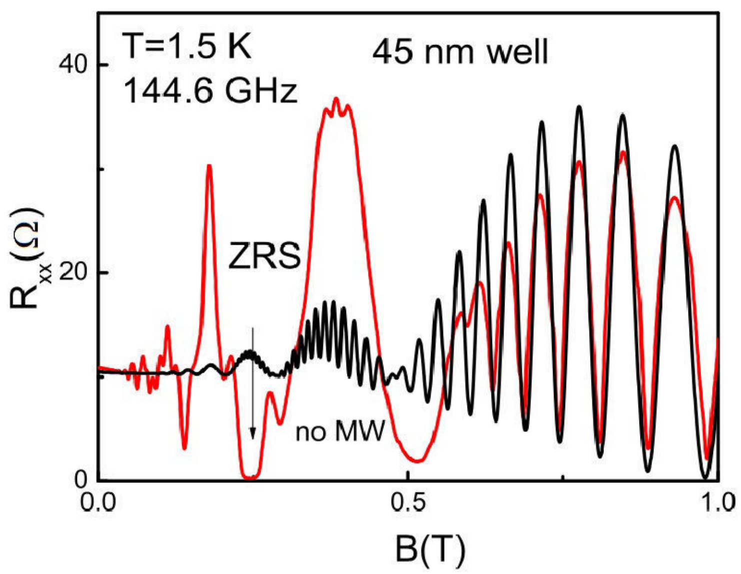

Figure 5.3: Longitudinal resistance, R_{xx} ($I = 1,4; V = 2,3$) without (no MW) and with microwave irradiation (144,6 GHz) in (a) a narrow (14 nm) and (b) a wide (45 nm) quantum well. Arrows indicate the regions of vanishing resistance (Figure adapted from (Levin et al., 2014)).

minima of the MIRO oscillations, have been found by carrying out frequency sweep measurements of magneto-resistance from $110GHz$ to $170GHz$. Moreover, in both quantum wells magneto intersubband (MIS) oscillations, due to the periodic modulation of the probability of intersubband transitions by the magnetic field, is observed in the magneto-resistance (Mamani et al., 2008). However, in NQW due to the low electron density in the second sub-band, these oscillations are observed at a relatively high magnetic field regions. Therefore, they are almost unaffected by MW radiation. In contrast, the interference of the MIRO and MIS oscillations in a bilayer system exposing to MW, lead to suppression or inversion of MIS peak, correlated with MW frequency (Wiedmann et al., 2008) and a ZRS develops from the MIS maximum (Wiedmann et al., 2010).

We have also measured the microwave power dependence of magneto-resistance oscillations for wide quantum well and the results are presented in Fig. 5.4. The observed behavior of the oscillations are in agreement with previous measurements reported in (Wiedmann et al., 2010).

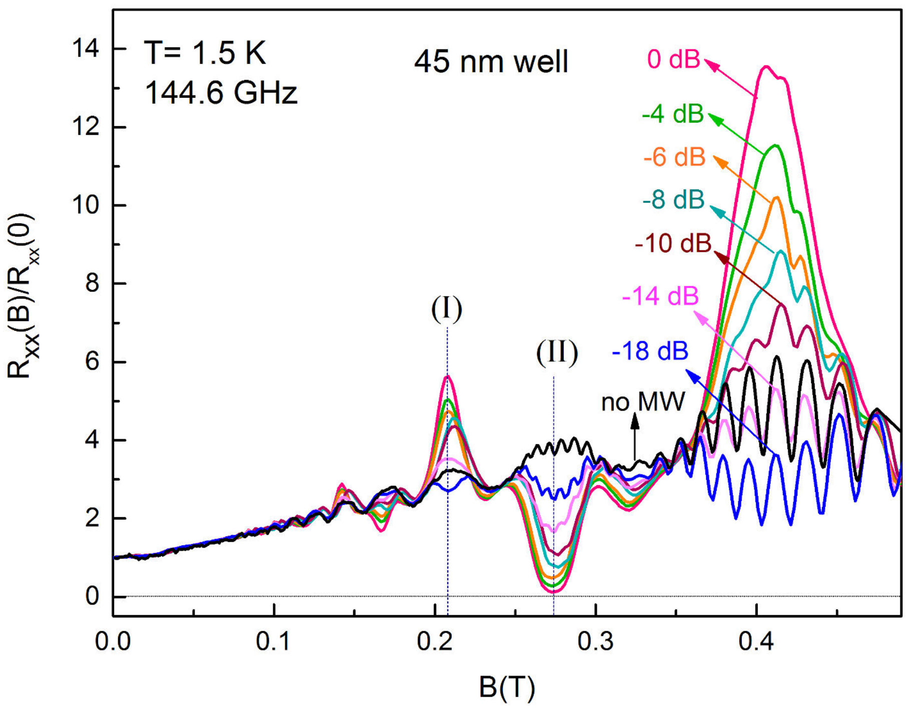

Figure 5.4: The power dependence of MIRO and ZRS to radiation power at T=1.5 K. Similar power dependence behavior observed in (Wiedmann et al., 2010) for peak (I) and ZRS at (II).

The nonlocal resistance $R_{NL} = R_{26,35}$, for device A and for both types of quantum wells, NQW and WQW, in the presence of MW irradiation and for different intensities of the radiation are presented in Fig. 5.5(b).

(a)

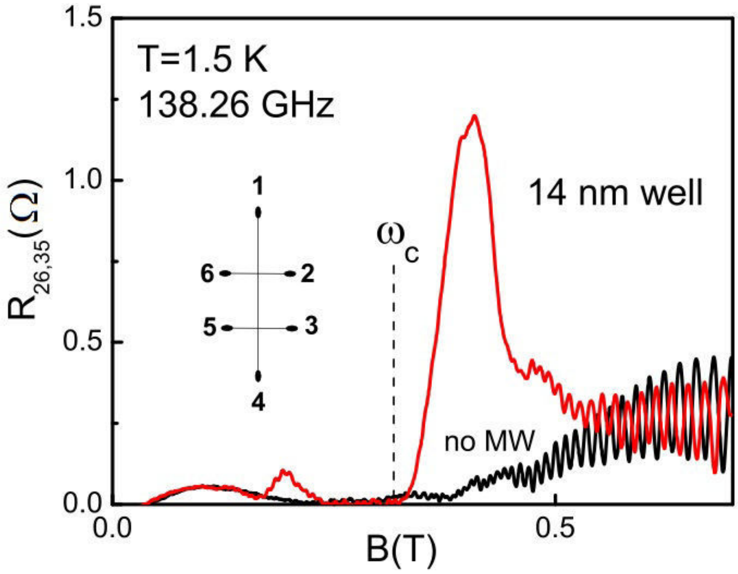

(b)

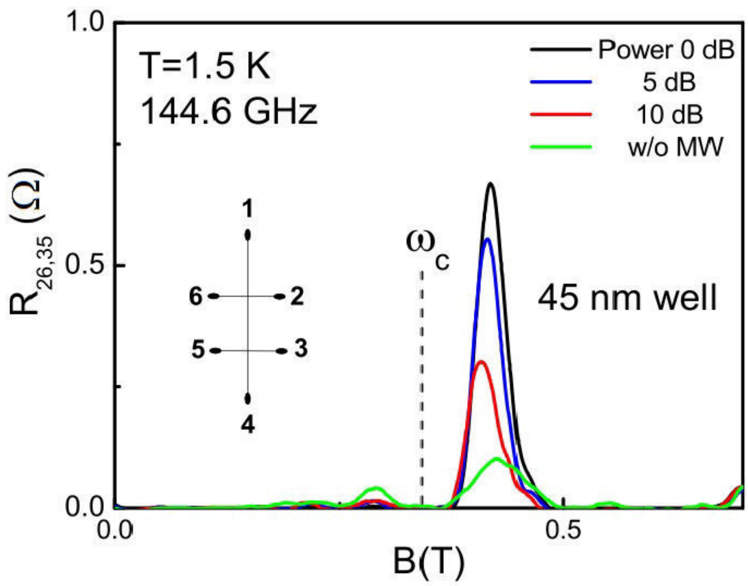

Figure 5.5: (a) Nonlocal resistance $R_{26,35}$, ($I = 2,6; V = 3,5$) without (no MW) and under microwave irradiation (138.26 GHz) in a narrow (14 nm) quantum well, (b) Nonlocal resistance $R_{26,35}$, ($I = 2,6; V = 3,5$) under microwave irradiation (144,6 GHz) in wide (45 nm) quantum well with decreasing microwave power. Insets show the measurement configuration (Figure adapted from (Levin et al., 2014)).

Note that, for measuring the nonlocal resistance, the current is passed through contacts 2 and 6 while the voltage is measured between contacts 3 and 5 ($I = 2,6; V = 3,5$). A prominent peak in nonlocal resistance corresponding to a peak in R_{xx} around $j \approx 3.15/4$, is observed for both samples. However, there is a drastic difference between local and nonlocal effects. In particular, the second peak at $B \approx 0.18\ T$ in local resistance, which has almost the same amplitude as the peak near $0.4T$, vanishes in the nonlocal resistance for WQW.

Moreover, for investigating the dependence of the nonlocal response with and without microwaves on the separation between the current and the voltage probes, measurements on device B, the WQW samples with multi-terminal hall bar, have been carried out. The results are shown in Fig. 5.6 in which the nonlocal resistance R_{NL} is measured in a different configuration, i.e. where the current flows between contacts 10 and 2 and the voltage is measured between contacts 3 and 9 (Fig. 5.6(a)), contacts 4 and 8 (Fig. 5.6(b)) and contacts 7 and 5 (Fig. 5.6(c)).

The origin of this resistance, as in the conventional quantum Hall effect, is the processes in the contacts regions. The contacts are assumed to be thermal reservoirs, where the mixing of electron states with different chemical potential will occur. The magnitudes of the peaks in devices A and B has a comparable value, which justifies the assumption that the length of the edge states is determined by the perimeter of the lateral arms rather than by the length of the bar itself. It implies that dissipation-less edge state transport persists over macroscopic distances because the length of the edge channels are determined by the distance between the metallic contacts ($1 \sim\ mm$) (Fig. 5.1).

The dependence of the nonlocal response, $\triangle R_{NL} = R_{NL}(E) - R_{NL}(0)$ on the current and voltage probes separation for device B is presented in Fig. 5.7, where $R_{NL}(0)$ and $R_{NL}(E)$ are nonlocal responses without and with MW, respectively. The signal decays as a function of length with a behavior that could be fitted with the exponential law $\triangle R_{NL} = R_0 \exp(-L/l)$, where R_0 is a exponential prefactor and l is the decay length. We find that the profile of $\triangle R_{NL}$ distance dependence fits to the exponential decay with parameters $R = 1\ Ohm$ and $l = 3.0\ mm$. These data offer evidence that, in a low magnetic field, MW induced edge-state transport really extends over a macroscopic distance of $1 \sim mm$. We have also studied the frequency dependence of microwave-induced nonlocal resistance and the results of measurements for three

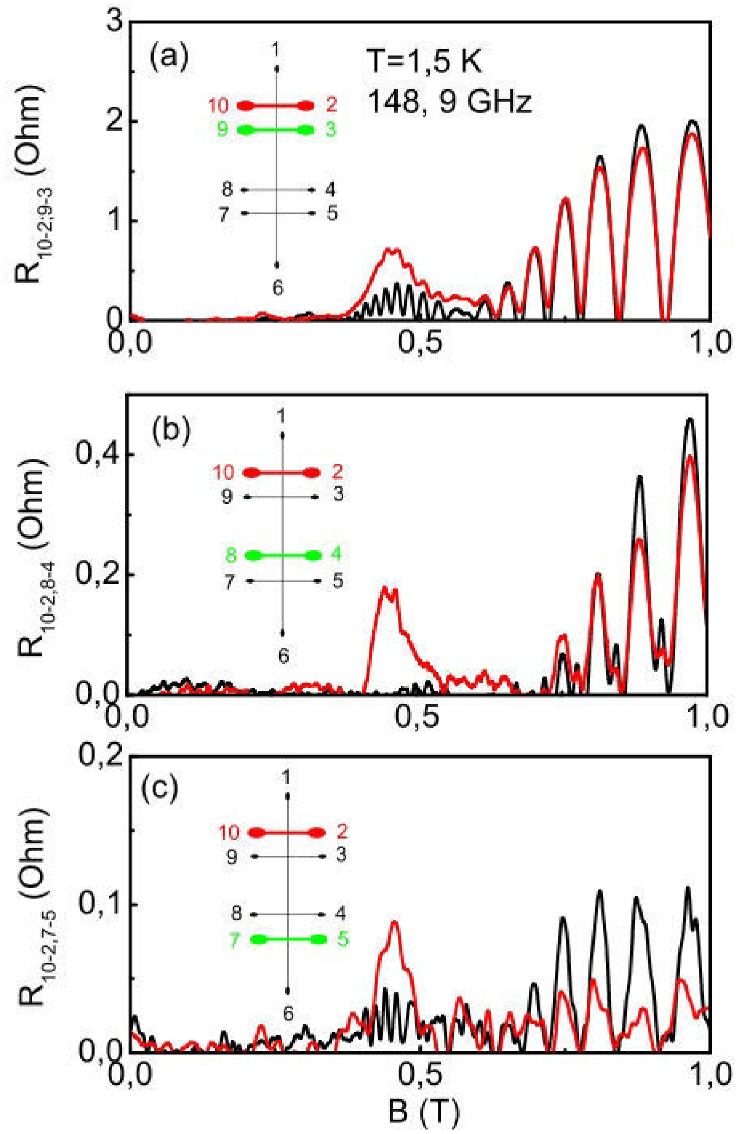

Figure 5.6: Nonlocal resistance R_{NL} without (black traces) and with microwave irradiation (148.9 GHz,red traces) in a wide (45 nm) quantum well (Device B) as a function of contact separation. Insets show the measurement configuration (Figure adapted from (Levin et al., 2014)).

chosen frequencies in device A are presented in Fig.5.8.

One can see only one dominant peak near $B \approx 0.4$ T. The magnitude of the peak varies with frequency due to the variation in microwave power. The position of the peak in NQW is correlated with frequency, while, in the bilayer system, peaks developed from combined

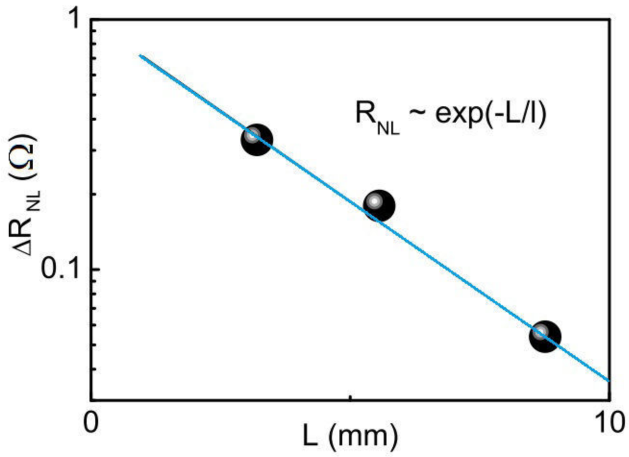

Figure 5.7: Nonlocal resistance for device B as a function of contact separation, the data are taken using various measurement configurations. The solid line is fitted to an exponential dependence with parameter $l = 3.0\ mm$ (Figure adapted from (Levin et al., 2014)).

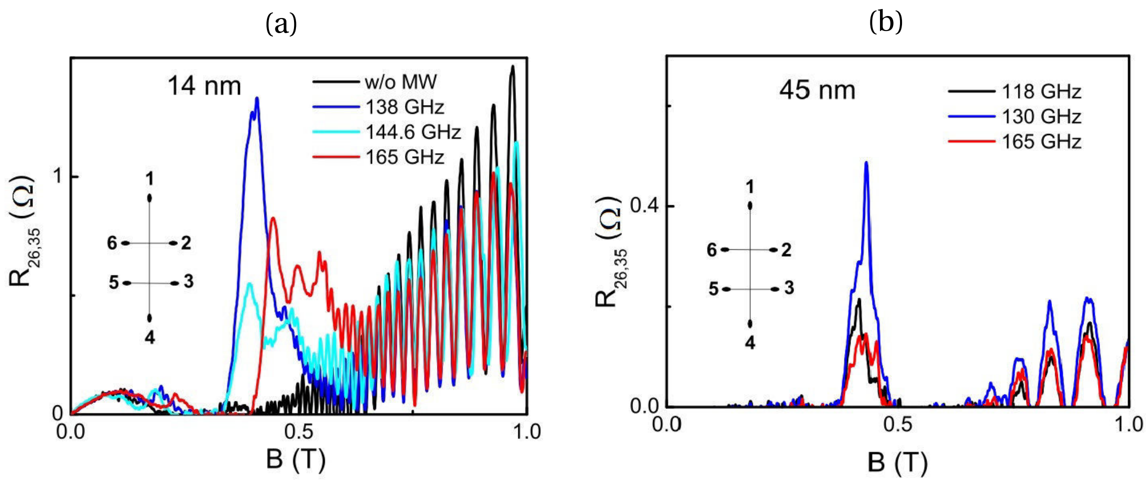

Figure 5.8: Nonlocal $R_{26,35}$ (I = 2,6; V = 3,5) resistances for narrow (a) and wide (b) quantum wells and for different microwave frequencies. Insets show the measurement configuration (Figure adapted from (Levin et al., 2014)).

MIS-MIR oscillations and, therefore, their location depends on sub-band splitting and is less sensitive to frequency (Wiedmann et al., 2010).

Besides, in order to increase the mobility of the samples due to its crucial role for ZRS evolution, samples of NQW are illuminated by LED, as mentioned before. After illumination the density increases and second sub-band becomes to be occupied. However, we verified, whether second sub-band is the origin of the nonlocal effect. The Fig. 5.9 shows the local (a) and nonlocal (c) resistances in narrow quantum well before LED illumination and compare them to corresponding resistances after LED illumination (b) and (d).

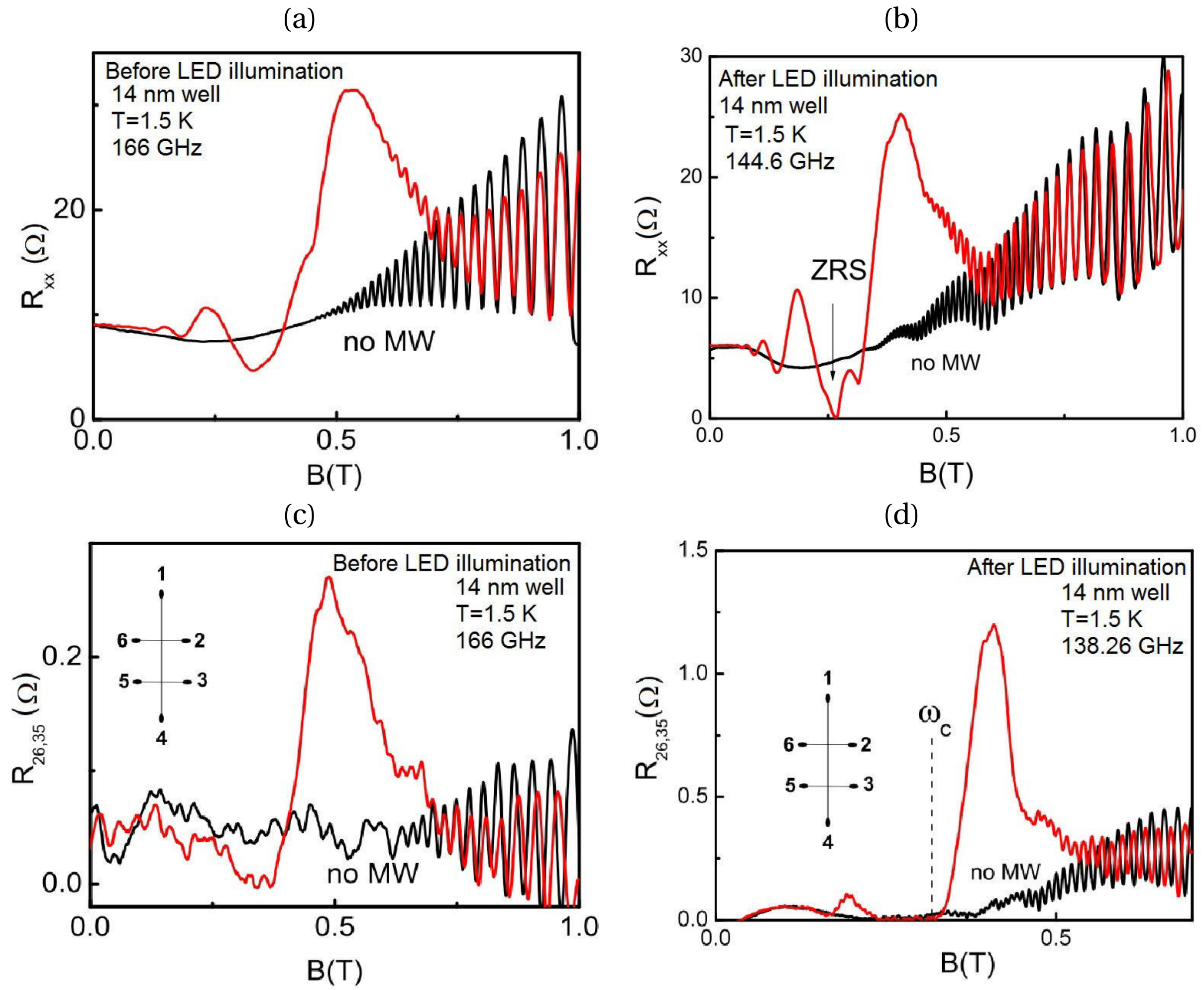

Figure 5.9: Comparision between longitudinal resistances, R_{xx} $(I = 1,4; V = 2,3)$(a, b) and nonlocal resistances, $R_{26;35}$ (c, d), before (a, c) and after (b, d) LED illumination without (no MW) and with microwave irradiation in a narrow (14 nm) quantum well(Figure adapted from Ref. (Levin et al., 2014)).

The Fig. 5.9 presents deep MIRO resistance minimum which is not developed into ZRS due to relatively smaller electron mobility ($\mu = 1.7 \times 10^6\ cm^2/Vs$). The magneto-intersubband oscillations are not observed at this density ($9.3 \times 10^{11} cm^{-2}$), and we may conclude that only one electron sub-band is occupied. Nonlocal resistance peak still persists (Fig.5.9(c)), although the value of the peak is much smaller, which we attribute to the effect of mobility. This experiment rules out the interpretation that second sub-band is responsible for MW induced nonlocal effect.

The classical ohmic contribution to the nonlocal effect is given by $R_{NL}^{classical} = \exp(-\pi L/w)$ for narrow strip geometry, where L is the distance between the voltage probes and w is the strip width (see Fig. 5.2(b)) (Van der Pauw, 1958). For our geometry and at zero magnetic field, we estimate $R_{NL}^{classical}/R_{xx} \approx 3 \times 10^{-4}$. In the QHE regime, the nonlocal resistance, R_{NL} arises from the suppression of electron scattering between the outermost edge channels and the back-scattering of the innermost channel via the bulk states (Buttiker, 1986; McEuen et al., 1990; Dolgopolov et al., 1991b). It appears only when the topmost Landau level is partially occupied and scattering via bulk states is allowed.

These measurements provide evidence for microwave-induced edge-state transport in the low magnetic field regime. Nonzero nonlocal resistance implies that the dissipationless edge-state transport persists over macroscopic distances because the length of the edge channels are determined by the distance between the metallic contacts ($\sim 1\ mm$) or, at least, by the distance between potential probes ($\sim 0.5\ mm$).

5.3 Theoretical model

The observed non-local effect can be understood within a theoretical approach based on nonlinear dynamics. It is shown in description of ZRS in semi-classical regime, edge trajectories become dominant for transport. Guiding along sample edges can lead to a significant decrease of R_{xx} with magnetic fields giving a negative magneto-resistance and singularities in R_{xy} (Roukes et al., 1987; Beenakker and van Houten, 1989). The theoretical understanding of this behavior is possible by considering the transmission probability T between voltage probes in a Hall bar geometry (Beenakker and van Houten, 1989) where the drop in R_{xx} is linked to increased T, however transmission remains smaller than unity due to disorder and R_{xx} remains finite.

In this model the impact of microwaves on stability of edge channels is considered and it is shown that microwave radiation can stabilize edge trajectories against small angle disorder scattering leading to a ballistic transport regime with vanishing R_{xx} and transmission exponentially close to unity (Chepelianskii& Shepelyansky, 2009).

The microwave field creates a nonlinear resonance described by the standard map, known as the Chirikov Taylor map or as the Chirikov standard map. It is constructed by a Poincare's surface of the section for electrons moving in the vicinity of the sample edge for the case of full specular reflection, from the wall in the presence of the microwave driving field.

Dissipative processes lead to trapping of particle inside the resonance. Depending on the position of the resonance center with respect to the edge, the channeling of particles can be enhanced or weakened providing a physical explanation of ZRS dependence on the ratio between microwave and cyclotron frequencies. In the trapping case, transmission along the edges is exponentially close to unity, naturally leading to an exponential drop in R_{xx} with microwave power (Chepelianskii& Shepelyansky, 2009).

In the following more details of the model, extended to our experimental conditions are described and the results of the model applied to our system are presented.

5.4 Analysis & discussion

5.4.1 Nonlinear resonance model for our samples

In order to compare the theory with our experiments, Levin et al. 2014 extend the results of the model based on nonlinear dynamics and show that we are able to completely reproduce the results published in the paper (Chepelianskii& Shepelyansky, 2009) and can extend the results of this model to our specific sample parameters and experimental conditions.

In this way, we solve classical dynamics for electrons in the proximity of the Fermi surface moving along the sample edge in the presence of magnetic field and AC microwave field which is linearly polarized in y direction. The motion is described by Newton's equation

$$\frac{d\mathbf{v}}{dt} = \boldsymbol{\omega}_{\mathbf{c}} \times \mathbf{v} + \omega \boldsymbol{\epsilon} \cos \omega t + \mathbf{I}_{ec}, \tag{5.1}$$

where the amplitude of the microwave field $\mathbf{E}$ is normalized according to

$$\boldsymbol{\epsilon} = \frac{e\mathbf{E}}{m\omega v_F}$$

where v_F is the Fermi velocity and $\mathbf{I}_{ec}$ represents the elastic collisions with the wall.
The solution for the equation 5.1 is calculated numerically using the Runge-Kutta method. Based on the calculated solution, we construct the Poincare section of velocity coordinate v_y versus the microwave phase $\phi = \omega t$ for the moments of collision with the sample edge. Poincare sections are done for different scattering angles maintaining the same coordinate of initial velocity in the x direction. The phase space in Fig. 5.10 has a characteristic resonance at a certain v_y/v_0 for which position depends on j.

We are mostly interested in the dynamics of electrons in the vicinity of the ratio $j = 3.15/4$, where the microwave-induced peak in the nonlocal response is observed in our experiments (Figs. 5.5 and 5.8). The electron trajectories for different values of the ratio j in the edge vicinity, are presented in Fig. 5.11.

One can see that the microwave field strongly modifies the dynamics along the edge. Figures 5.11(b)- 5.11(d) show Poincare sections for the wall model and different values of the magnetic field corresponding to the peak R_{NL} around $B = 0.42T$ ($j = 3.15/4$), on the high-field side of the peak ($j = 2.8/4$) and on the resistance minima ($j = 5/4$). For $j = 5/4$ Poincare sections exhibit periodic and quasi-periodic trajectories surrounded by a chaotic sea. For $j = 2.8/4$ and $j = 3.15/4$ Poincare sections exhibit less stable dynamics, however a periodic component remains present.

The existence of the periodic orbits plays a fundamental role in the local and nonlocal resistivity of a 2D gas. The truly dissipationless edge channels may carry the same electrochemical potential μ over a macroscopic distance to the different voltage probes. Hence, $\triangle\mu = 0$, which results in vanishing longitudinal (R_{xx}) and nonlocal (R_{NL}) resistivity. If a certain fraction of the edge states are scattered into the bulk, it leads to different local chemical potentials, finite $\triangle\mu$, and resistivity. This situation closely resembles the QHE, when it is possible to treat the

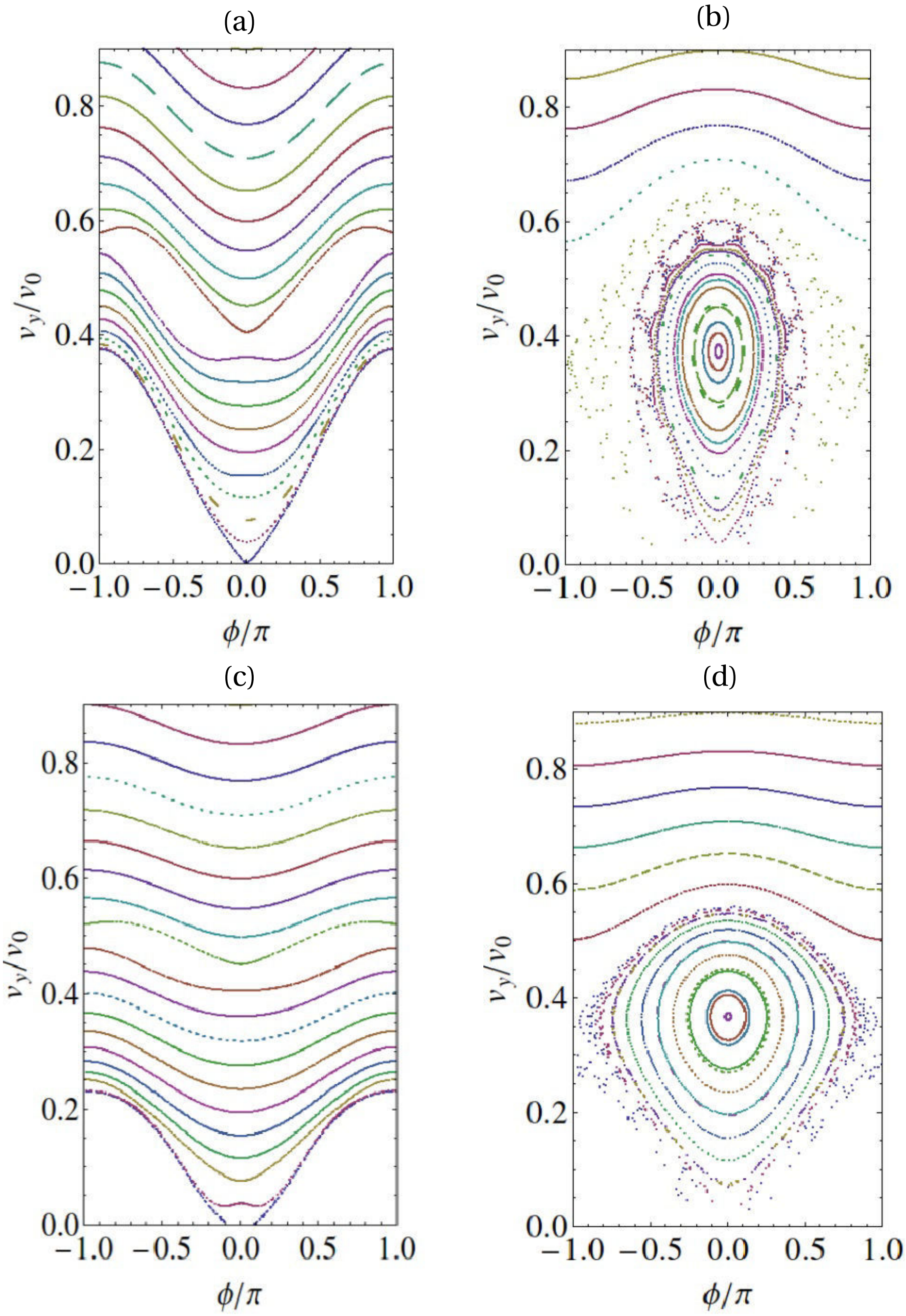

Figure 5.10: Poincare section for $j = 7/4$ (a, c) and $j = 9/4$ (b, d) at y-polarized field with $\varepsilon = 0.02$ (c, d) and $\varepsilon = 0.05$ (a, b) (Figure adapted from (Levin et al., 2014)).

edge and bulk conducting pathways separately. This may lead to nonlocal resistivity. For example,in the QHE regime, the nonlocal resistance, R_{NL}, arises from the suppression of electron scattering between the outermost edge channels and back-scattering of the innermost

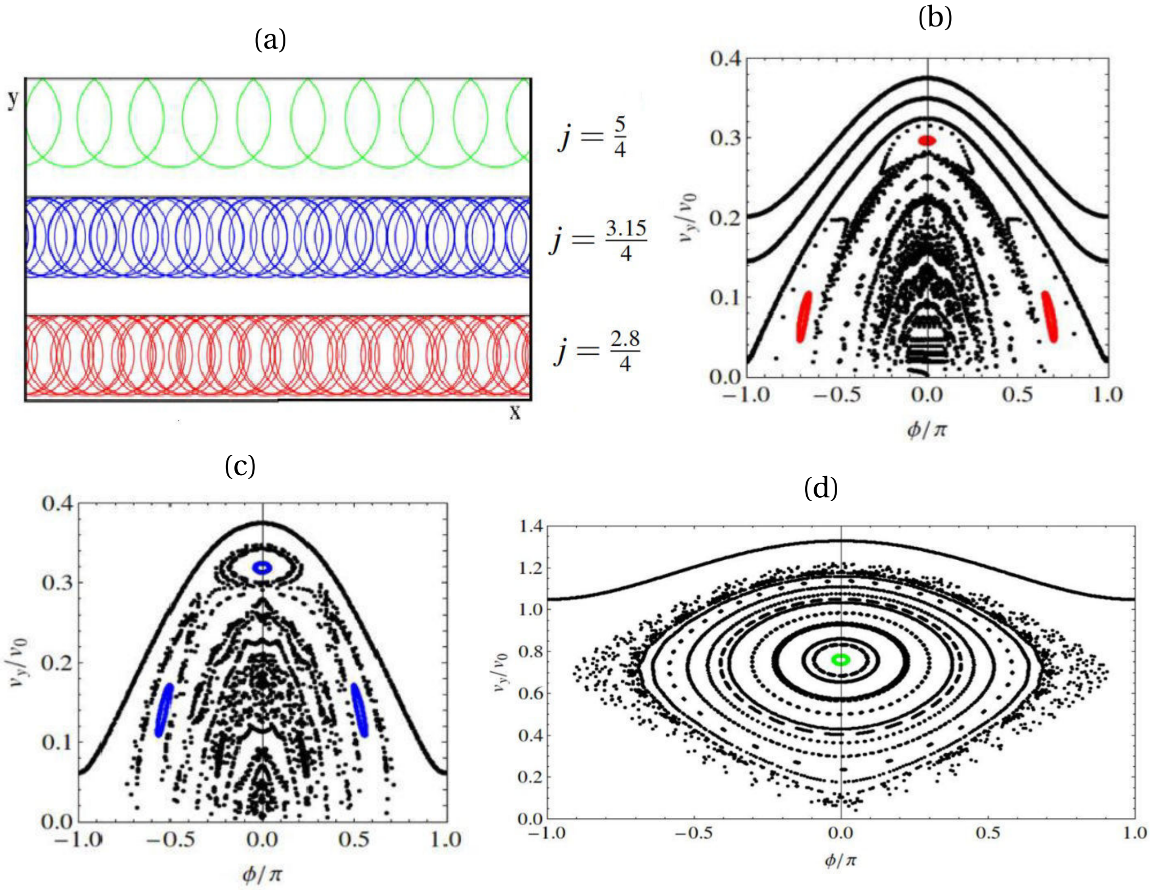

Figure 5.11: (a) Electron trajectories along the sample edge for several values of $j = 5/4$, $j = 3.15/4$ and $j = 2.8/4$; (b) Poincare sections for $j = 2.8/4$, (c) $j = 3.15/4$ and (d) $j = 5/4$ at y-polarized field with $\varepsilon = 0.02$ (Figure adapted from (Levin et al., 2014)).

channel via the bulk states (Buttiker, 1986; McEuen et al., 1990; Dolgopolov et al., 1991b). It is worth noting that the actual shape of the wall potential is parabolic rather than a hard wall. We have compared nonlinear resonance and Poincare sections for both potentials. We estimate the steepness of the potential from the assumption, that the width of the region where the potential increases from the bottom to the Fermi energy is of the same order as the Fermi wavelength for typical electron concentrations (Ando and Uryu, 2000) . We would like to emphasize that in our experiments, samples with high electron density corresponding to the steeper potential, are used. Assuming confinement edge potential $U = ky^2/2$ $(y > y_0)$, where y_0 is the edge of the sample, we estimate $k = 0.008$ $meV/\text{Å}^2$. The comparison of the trajectories and Poincare sections for both potentials are presented in Fig. 5.12.

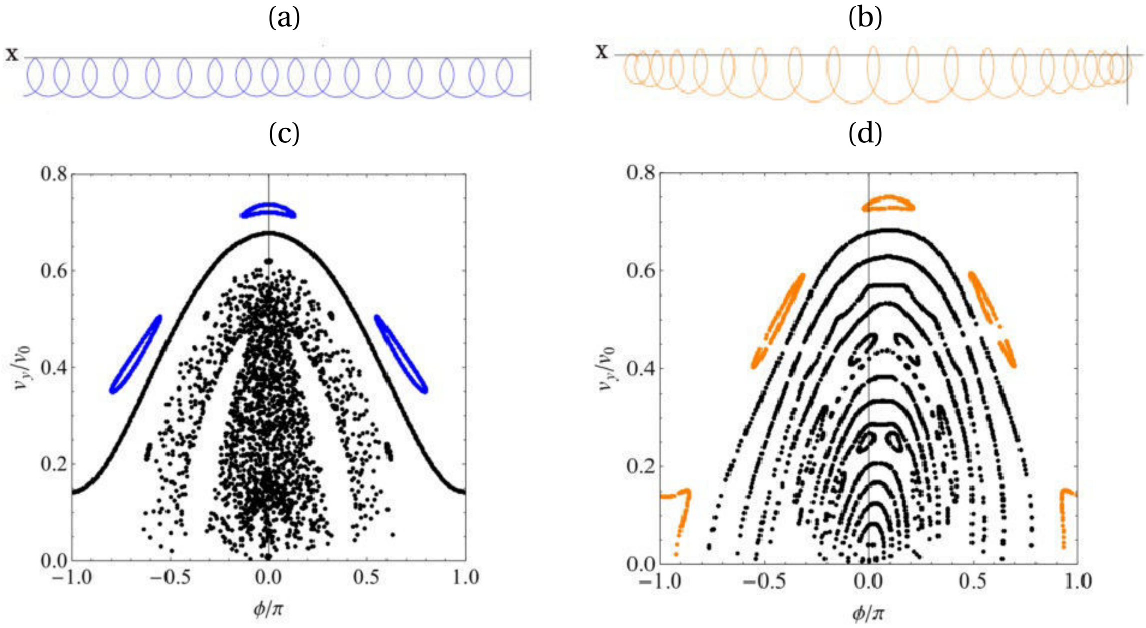

Figure 5.12: (Examples of electron trajectories along sample edge for values of $j = 3.15/4$: (a) hard wall potential,(b) parabolic wall potential and y-polarized field $\epsilon = 0.07$. Corresponding Poincare sections are presented below (c) and (d)) (Figure adapted from (Levin et al., 2014)).

One can see the running electron trajectories stabilized by MW field and similarity between both cases. The Poincare sections for both potentials exhibit periodic and quasi-periodic trajectories surrounded by a chaotic sea. Therefore, we may conclude here, that there is no significant difference between hard and soft wall potentials for realistic parameters.

However, demonstration of the existence of the periodic orbits stabilized by the MW field is not enough to justify the nonlocal response and some further qualitative analysis might be required to compare the magnitude of R_{Nl} with calculations using a simple model. Therefore, we provide a model describing the edge and bulk contribution to local and nonlocal resistance by taking into account the edge and bulk contribution to the total current. The transport properties in the bulk can be described by the current-potential relation

$$\mathbf{j} = -\hat{\sigma}\nabla\psi, \qquad \hat{\sigma} = \begin{pmatrix} \sigma_{xx} & \sigma_{xy} \\ -\sigma_{xy} & \sigma_{xx} \end{pmatrix}, \tag{5.2}$$

where ψ is electrochemical potential for electrons. Since the charge conservation continuity condition requires that $\nabla j = 0$, we can solve the problem by solving the 2D Laplace equation, $\nabla^2\psi = 0$, for the electrochemical potential, ψ across a rectangular Hall bar, with boundary conditions supplied by current continuity at the boundaries:

$$\sigma_{xx} n\nabla\psi + \sigma_{xy} n\nabla\psi + g(\varphi - \psi) = 0, \tag{5.3}$$

where φ describes the edge state and satisfies a phenomenological model (Abanin et al., 2007; Dolgopolov et al., 1991a)describing the edge-to-bulk leakage:

$$\frac{d\varphi}{dx'} = \pm g(\varphi - \psi), \tag{5.4}$$

where sign $+/-$ corresponds to the top/bottom edge of the sample (high potential applied to the right-side contact), x' is the distance along an edge, and g is the phenomenological constant, which represent scattering between φ and ψ modes.

For simplicity, our sample, device A is modeled by a rectangle with dimensions $1500 \times 200\ \mu m^2$ The Dirichlet boundary condition are set at the 200 μm wide metal contacts located at the left and right sides of the bar for the local case or at the 10 μm wide contacts around $y = 500\ \mu m$ at the left and right edge of the bar for the nonlocal case (see fig. 5.1(a) and inserts to Fig. 5.13).

To describe the DC current through the sample, we solve numerically the 2D Laplaces equation auto consistently with Eqs. 5.3 and 5.4 for all the sample edges. The numerical results for ψ and φ are presented in Fig. 5.13 for two experimental configurations.

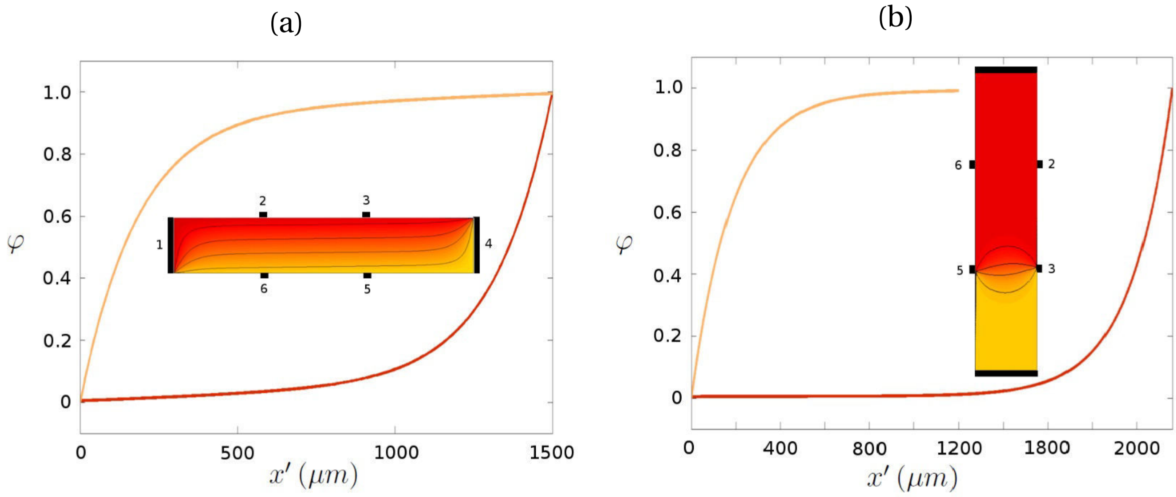

Figure 5.13: Numerical simulation results for electrochemical potentials φ (in arb. units) along top (orange) and bottom (red) edges of the sample and ψ (in arb. units) across the Hall bar in the (a) local and (b) non-local configurations.

The total current is calculated as the sum of the bulk and edge currents, where

$$\begin{aligned} I_{bulk} &= \int_0^w \sigma_{xx}\frac{\partial\psi}{\partial x}dy + \sigma_{xy}(\psi_{top} - \psi_{bot}); \\ \sigma_{xx,xy} &= \frac{\rho_{xx,xy}}{\rho_{xx}^2 + \rho_{xy}^2}, \rho_{xx} = \frac{1}{n_s e\mu}, \rho_{xy} = \frac{B}{n_s e}, \\ I_{edge} &= \frac{Me^2}{h}(\varphi_{top} - \varphi_{bot}); \end{aligned} \tag{5.5}$$

and the resistance is given by:

$$R_{xx} = \frac{\varphi_{cont1} - \varphi_{cont2}}{I_{total}}, \tag{5.6}$$

It is important to mention that more precise calculations require exact knowledge of the fractions of electrons channeling along the wall $P = M/N$, with N the total number of the Landau levels. Taking into account $N \approx 120$, the total number of the Landau levels near $B \approx 0.42\ T$, we may choose $M = P \times N \approx 1$–3 and a current carried by edge channels $I \sim Me^2\varphi/h$. The model reproduces the experimental values of the local $R_{14,23} \approx 40\Omega$ and nonlocal $R_{26,35} \approx 1.2\Omega$ resistances with adjustable parameter $g = 0.005\ \mu m^{-1}$ and $M = 3$.

5.5 What we have learned

The results of our findings may indicate that MIRO and ZRS are very rich physical phenomena, which result from a combination of both bulk and edge-state contributions. We believe that the ZRS phenomenon is somewhat like the quantum Hall effect, although not exactly the same, which can be described as a bulk or/and edge phenomenon (e.g., (Kao & Lee, 1999)).

Indeed both descriptions are experimentally supported by measurements: observations of the nonlocal effects clearly demonstrate edge-state conduction (McEuen et al., 1990), and observations of the charge transfer in Corbino geometry, where the edge transport is shunted via concentric contacts, show that the quantum Hall effect, as a consequence of pure bulk transport, is possible (Dolgopolov et al., 1992).

From the results of our experiment in this chapter, we may conclude that the edge-state effect is dominant or comparable with the bulk contribution near $\omega/\omega_c \approx 3.15/4$. Note, however, that our results do not explicitly rule out the bulk mechanism near minimum j = 5/4 and, therefore, do not contradict previous investigations.

This data offers evidence that, in a low magnetic field, MW-induced edge-state transport really extends over a macroscopic distance of ~ 1 mm. We compare our results to a transport model that takes into account the combination of the edge-state and the bulk transport contributions and the back-scattering within the bulk-edge coupling.

Chapter 6

Magneto thermopower with MW

Contents

MOTIVATIONS for measurements of thermo-electric properties of low dimensional systems mostly come from the complementary information to those obtained from ordinary charge transport. As an example in an ordinary Drude model the electrical conductivity σ is simply proportional to the scattering time τ, while diffusion thermopower depends on τ and its derivative $\frac{d\tau}{dE}$ (Zhang et al., 2007). Moreover, in low dimensional system there is close connection between thermopower and the entropy per particle which is hold for non interacting and interacting free disorder electron systems at high magnetic fields (Dmitriev et al., 2005).

On the other hand, in spite of attention to the MIRO and ZRS phenomena, most of the related experimental studies are almost entirely based on the measurements of electrical resistance or conductance under dc driving. The observation of MW-induced photovoltaic oscillations (Bykov, 2008; Dorozhkin et al., 2009; Dmitriev et al., 2009) is an exception which occur in the samples with built-in spatial variation of electron density because the MW irradiation strongly modifies the conductivity while leaving the diffusion coefficient unaffected (Dmitriev et al., 2009).

In this thesis, we suggest that when temperature T varies across the sample, the MW irradiation creates conditions which allow one to observe, without any external DC driving, an oscillating thermo-induced voltage proportional to the resistance and closely resembling a MIRO signal.

In this chapter, we provide the experimental results of our measurements. The analysis of our experiments according to the theoretical model proposed by Prof. Raichev is presented afterward.

6.1 What we want to know

- How do the phonon-drag voltage oscillations correlate with the resistance oscillations under MW irradiation?
- What are the manifestations of ZRS in phonon drag voltage oscillations?
- How can the results of our experiments be explained theoretically?

6.2 Experimental methods & observations

For experimental measurements, we have exploited narrow (14 nm) quantum wells with electron density of $n \simeq 10^{12}\ cm^{-2}$ and the mobility of $\mu \simeq 2 \times 10^{6}\ cm^{2}/Vs$, at $T = 1.5$ K. The sample consists of circular central part (diameter 1 mm) with four long (length 5 mm, width 0.1 mm) arms ending with the voltage probes. The unconventional design, Fig. 6.1, has been proposed to study the polarization dependence in the microwave region in order to reduce the influence of the metal contacts on electric field polarization.

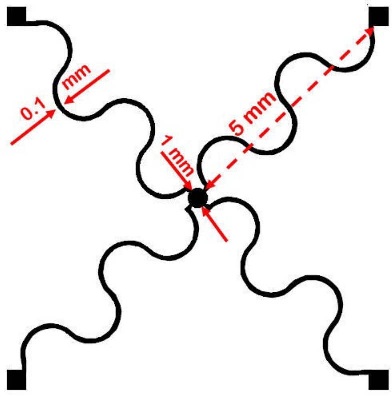

Figure 6.1: Schematic of the unconventional design introduced to sample via photo-lithography process and wet etching.

First of all, we have measured the magneto-resistance oscillations under MW irradiation to check if ZRS are developed. We observed ZRS developed from the minima of MIRO oscillation and measured the frequency dependence of ZRS and MIRO at different MW frequency. The results of our measurement in Fig. 6.2, show the well developed ZRS at $f = 130GHz$. Decreasing the MW frequency leads to reduction of the width of ZRS until it disappears. Moreover, we have observed that the peaks of MIRO are shifted to lower magnetic filed as the radiation frequency decreases. The width dependence of ZRS to MW frequency is shown in the inset of Fig. 6.2.

In order to provide the heater for our samples, we have used Silver-ink as presented in Fig. 6.3(b). We put a specific amount of the ink on the sample and wait till the ink becomes dry. When the ink is dried the resistance of this part can be used to produce the high temperature needed in a heater. To have the desired temperature gradient along the sample, a small piece of Copper bar is attached on the opposite side, operating as a heat sink.
The measurements have been carried out in a VTI cryostat with a waveguide to deliver MW irradiation (frequency range 110 to 170 GHz) down to the sample. The heater is placed symmetrically between the arms 1 and 2 at a distance of 4.1 mm from the center, generates phonon flux (see Fig. 6.3).

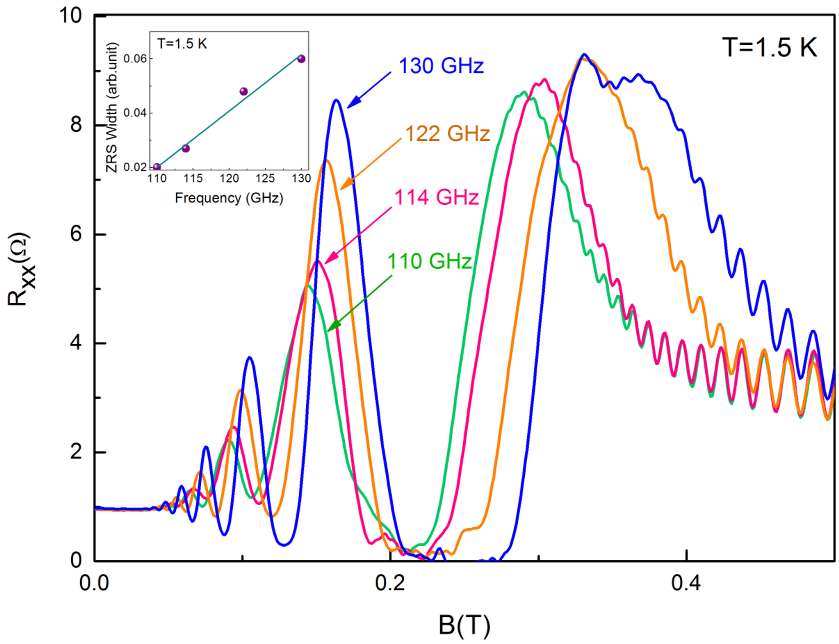

Figure 6.2: The frequency dependence of MIRO and ZRS at $T = 1.5$ K. The inset represent the width of ZRS vs radiation frequency of 110 GHz, 114 GHz, 122 GHz and 130 GHz.

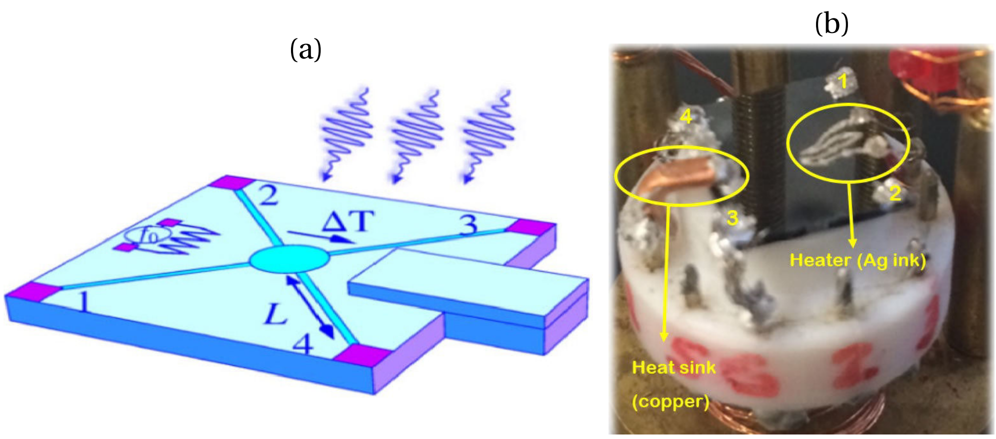

Figure 6.3: (a) Schematic of sample with heater and heat sink under MW irradiation, (b) The real sample used for the measurements, heater , heat sink and contacts are detemined with yellow marks.

The induced voltages by this flux are measured using a lock-in method at the frequency of $2f_0 = 54$ GHz, both in the longitudinal, V_{14} and V_{23}, and in the transverse, V_{12} (hot side) and V_{43} (cold side), configurations. Measuring the thermo-voltage at different applied heating voltage both without and with MW irradiation have been carried out, to be sure that the measured signal is thermo-voltage as a result of temperature gradient. We have carried out several measurements on different prepared samples. Fig. 6.4 shows the results of the measured thermo-voltage for different applied heating voltage.

(a)

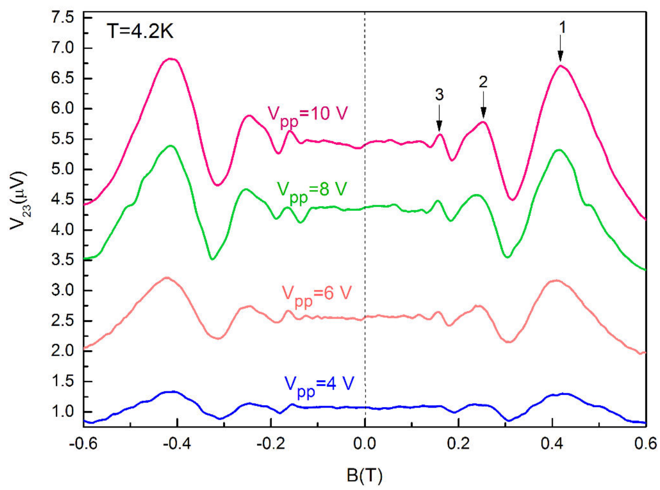

(b)

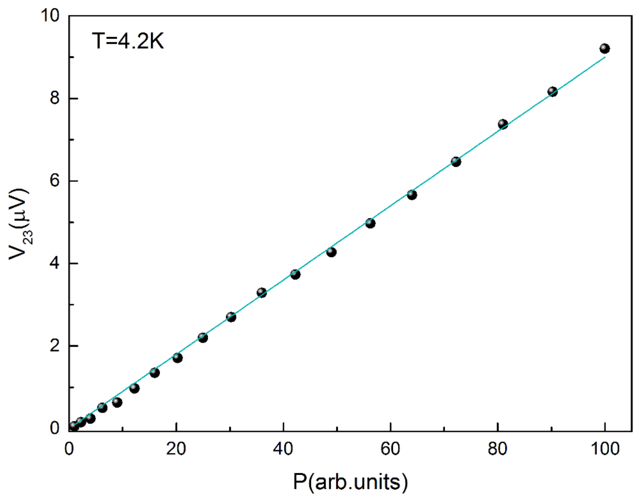

Figure 6.4: (a)The measured thermo-voltage vs different applied voltage of heater without MW irradiation; arrows indicate the maxima for $l = 1, 2, 3$ in magneto-thermovoltage oscillations.(b) The dependence of thermo-voltage to heating power at T=4.2 K.

Furthermore, we observe that without powering the heater no photo-voltage was observed. The thermo-voltage increases linearly with heater power as is shown in Fig. 6.5.

(a)

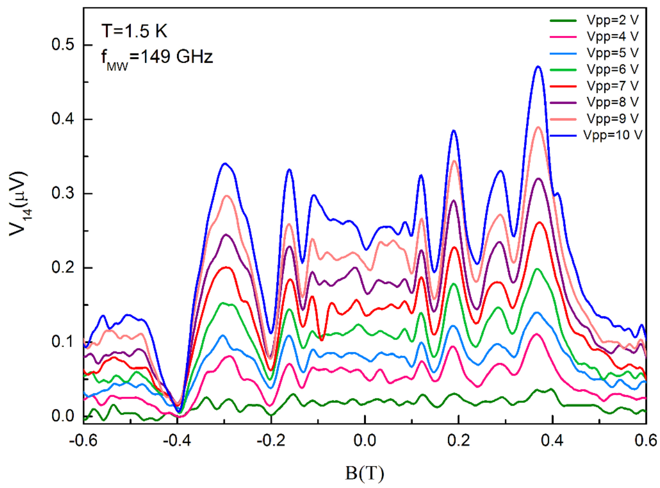

(b)

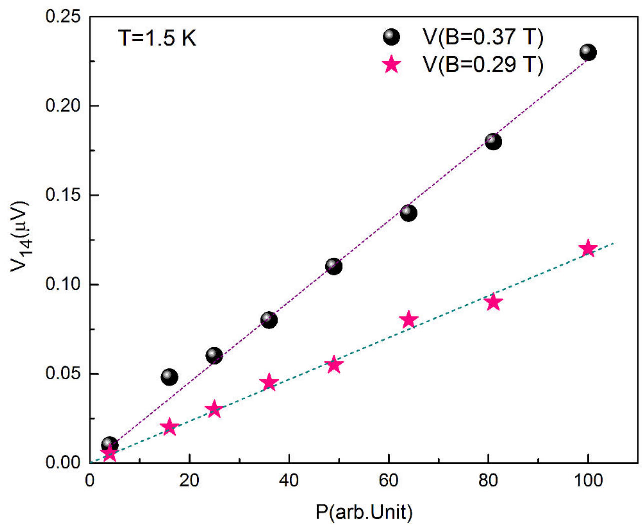

Figure 6.5: (a) The measured photo-voltage for different applied heating voltage, (b) Amplitude of photo-voltage at two different magnetic field B=0.29 T and B=0.37 T vs heating power.

We have shown here the linear dependence of the amplitudes of measured photo-voltage at two specific magnetic field values of $B = 0.37T$ and $B = 0.29T$. However, similar linear dependence exist for the peaks of measured photo-voltage at corresponding magnetic fields.

Moreover, in order to determine the temperature gradient along the samples, we have carried out the two probe measurements (contacts 1–2 and 3–4) for a specific heating voltage at hot side and cold side of the samples. The results of our measurements are presented in Fig. 6.6. Exploiting the amplitude of the Shubnikov–de Haas (SdH) oscillation, we have found that the difference in the electron temperature between hot and cold sides is found $\triangle T \simeq 0.3$ K at the lattice temperature $T = 1.5$ K.

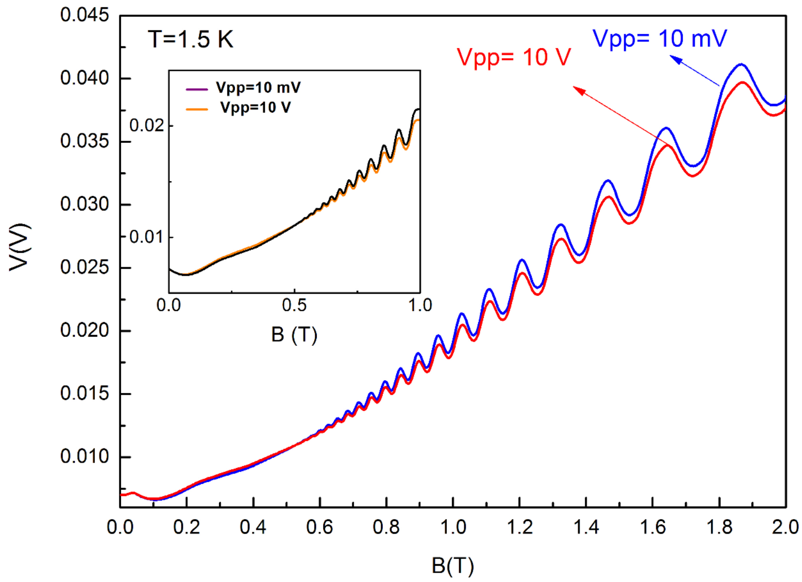

Figure 6.6: The measured voltage on the hot side and cold side (the inset) of the sample using the two probe measurement at $T = 1.5$ K and for heating voltage $V_{pp} = 10mV$ and $10V$.

The dependence of the measured MW induced thermo-voltage to the MW power is presented in Fig. 6.7. With increasing the MW power the amplitude of the signal increases.

Several devices from the same wafer have been studied. The magneto-resistance (Fig. 6.8) was measured as a response V_{14} to the current injected through the contacts 2 and 3. The ZRS is observed at T below 4.2 K. Similar results are obtained for the other contacts. The magneto-oscillations of V_{23} and V_{12}, both with and without MW (dark signal), are presented

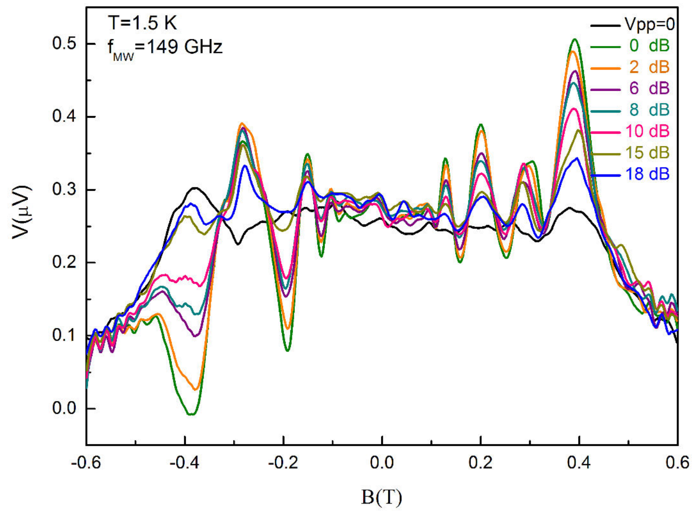

Figure 6.7: Dependency of measured phonon drag signals to MW power at T=1.5 K and MW frequency of 149 GHz for Vpp=10 V.

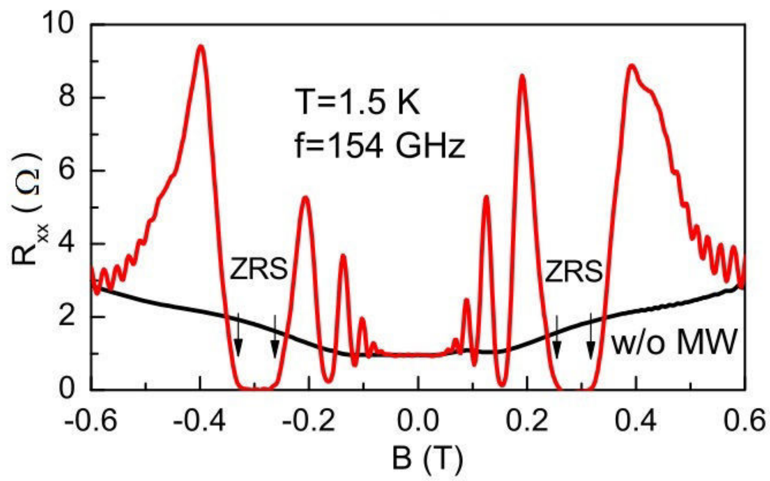

Figure 6.8: longitudinal resistance without and with MW irradiation (154 GHz) as a function of magnetic field. Arrows show the ZRS region (Figure adapted from (Levin et al., 2015)).

in Figs. 6.9 and 6.10. The transverse voltage V_{43} in cold side is much weaker than V_{12} in hot side,however, both have the same periodicity. Moreover, the dark voltages V_{23} and V_{12} demonstrate acoustic magneto-phonon oscillations whose period is determined by the ratio $2k_f s_\lambda/\omega_c$, with $k_F = \sqrt{2\pi n_s}$ the Fermi wave number and s_λ, the sound velocity for phonon mode λ. These oscillations due to resonant phonon-assisted back-scattering of electrons were observed previously (Zhang et al., 2004).

(a)

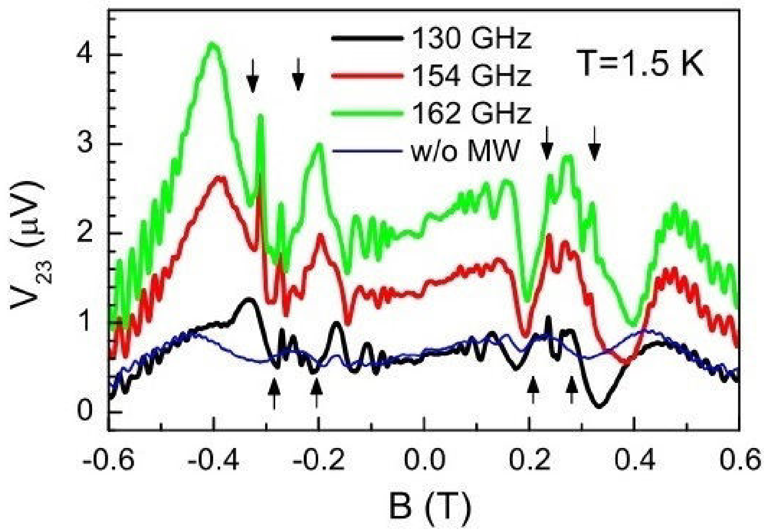

(b)

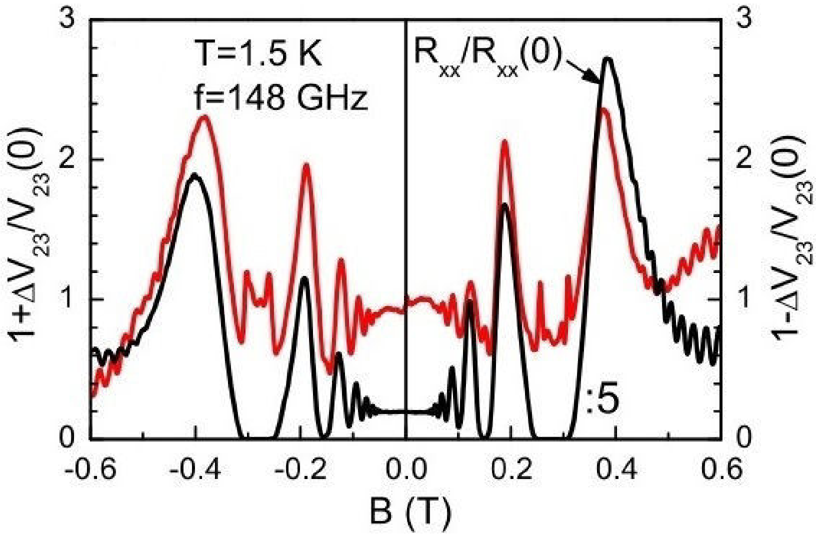

Figure 6.9: (a) Magnetic-field dependence of the longitudinal phonon-drag voltage (PDV), V_{23}, without and under MW irradiation for different microwave frequencies (shifted up for higher frequencies). Arrows show the ZRS region. (b) PDV oscillations vs MIRO at 148 GHz. For clarity of the comparison, the sign of $\triangle V_{23} \equiv V_{23}(B) - V_{23}(0)$ is inverted at B>0 and the resistance is scaled down by the factor of 5 (Figure adapted from (Levin et al., 2015)).

The MW irradiation enhances both V_{12} and V_{23} by adding oscillating contributions odd in B. The positions of the peaks and minima of these phonon-drag voltage (PDV) oscillations coincide with those of MIRO. The MW-induced contributions to V_{23} and V_{14} have opposite signs.

(a)

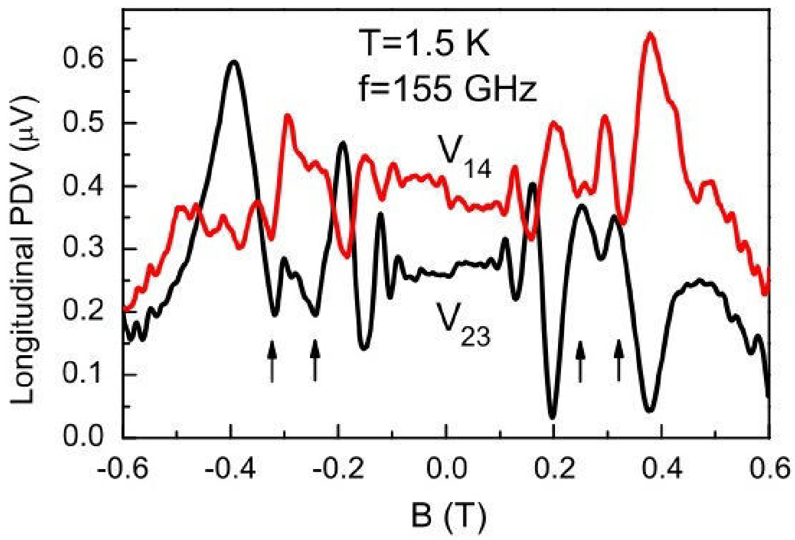

(b)

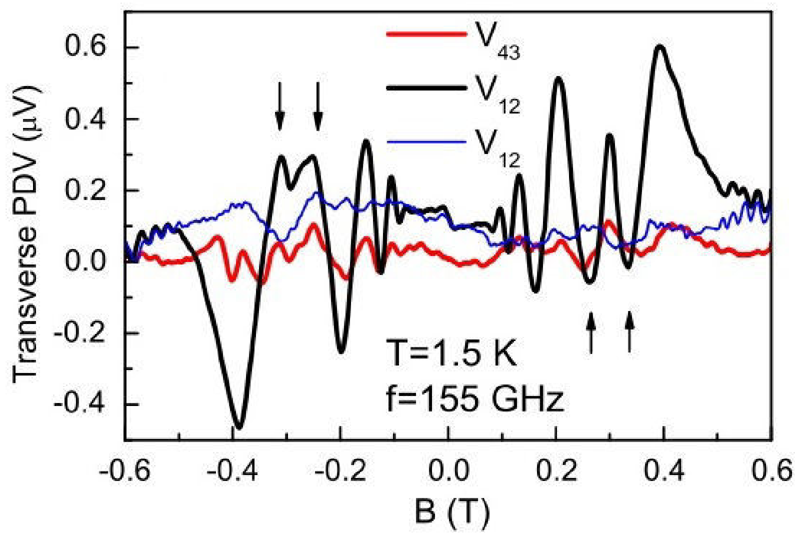

Figure 6.10: (a) Magnetic-field dependence of V_{23} and V_{14} under MW irradiation. The MW-induced contributions to these voltages have opposite signs. (b) Transverse phonon-drag voltage (PDV) V_{12} (high amplitude) and V_{43} (low amplitude) under MW irradiation. Thin line: V_{12} without MW irradiation (Figure adapted from (Levin et al., 2015)).

According to the general symmetry properties of thermo-electric coefficients, the odd in B voltages develop in the direction perpendicular to the temperature gradient or phonon flux. Thus, the odd in B behavior of V_{12} is expectable, while the appearance of odd in B contributions to V_{23} and V_{14} may look surprising. However, the explanation of this fact, is straightforward.

Due to the the position of the heater between the long radial arms of the device (see Fig. 6.3(a)), there is no homogeneous unidirectional phonon flux in the 2D area of the device. The phonons coming from the heater cross the arms attached to probes 1 and 2 in the directions perpendicular to these arms, so the voltages V_{23} and V_{14} , besides the longitudinal (even in B)phonon-drag contributions, contain significant transverse (odd in B) contributions. Since the phonons come to the arms 1 and 2 from different sides, the transverse contributions V_{23} and V_{14} should have different signs, in agreement with our observation.
Therefore, the observed MW-induced voltages is identified from our experiments as a result of the transverse phonon-drag effect (spatial redistribution of electrons in the direction perpendicular to the phonon flux), which is strongly enhanced because of the influence of microwaves on the resistance.

6.3 Theoretical model

The observations of surprisingly strong and anti-symmetric in magnetic field signal of phonon drag voltage under MW irradiation can be described by the following theory which is developed by Prof.Raichev.

The presence of magneto-phonon oscillations in the measured longitudinal voltage in the absence of MW suggests that the phonon drag mechanism is important. The periodicity of these oscillations occurred as a result of phonon assisted back-scattering of electrons is determined by the resonances $\omega_{ph} = n\omega_c$ where n is an integer and ω_{ph} is the resonant phonon frequency estimated as $2sk_f$ with s the phonon velocity and $k_f = \sqrt{2\pi n_s}$ is the Fermi wave-number of electrons.

Since the observed oscillations have large amplitude even at the temperatures as small as 1.5 K where the Bloch-Gruneisen regime, $T \ll \hbar s k_F$, is reached and so the back-scattering is exponentially suppressed. Thus in thermoelectric experiments, it is quite possible that a significant part of the phonons causing phonon drag effect,the drag of electrons due to electron-phonon interaction,may arrive to the 2D system directly from the heater, via ballistic propagation. This assumption is reasonable since the mean free path of acoustic phonons at low temperatures is very large, of 1 mm scale in GaAs , and can be comparable with the distance between the heater and the 2D system.

Regardless of the number of such phonons in comparison to the number of equilibrium phonons, they are still very important in the drag effect, since these are high-energy phonons whose energy is determined by the heater temperature T_{ph} rather than the temperature T of the 2D sample. Such phonons are able to cause a large change of electron momentum in the low-temperature (Bloch-Gruneisen) regime while equilibrium phonons can only assist a scattering with a small change of electron momentum.

The phonon-drag electric current density can be found using the formalism of the quantum Boltzmann equation accounting for interaction of electrons with phonons and impurities. In the case of degenerate electron gas, the components of the current density are given by

$$\begin{pmatrix} J_x^{ph} \\ J_y^{ph} \end{pmatrix} = \frac{ek_F}{2\pi\hbar} \int d\varepsilon D_\varepsilon \begin{pmatrix} (f_{\varepsilon+1} + f_{\varepsilon-1}) \\ i(f_{\varepsilon+1} - f_{\varepsilon-1}) \end{pmatrix}, \tag{6.1}$$

where k_F is the Fermi wave-number and D_ε is the density of electron states expressed in the units $m/\pi\hbar^2$, so that in non-quantizing magnetic field $D_\varepsilon = 1$. The first order angular harmonics of electron distribution function are $f_{\varepsilon\pm1}$,which in the perpendicular magnetic field to the sample are found from the following equation

$$(\pm i\omega_c + \nu_{tr} D_\varepsilon) f_{\varepsilon\pm1} = \delta J^{ph}_{\varepsilon\pm1}, \tag{6.2}$$

where ν_{tr} is the transport scattering rate (inverse to the transport time τ_{tr} and $\omega_c = |e|B/m$ is the cyclotron frequency. δJ^{ph} is the part of the electron-phonon collision integral caused by non-equilibrium phonons characterized by the mode index λ and three-dimensional wave vector $\mathbf{Q} = (\mathbf{q}, q_z)$:

$$\delta J^{ph}_{\varepsilon\pm1} = \frac{m}{\hbar 3}\sum_{\lambda}\int_{-\infty}^{\infty}\frac{dq_z}{2\pi}\int_0^{2\pi}\frac{d\varphi}{2\pi}\int_0^{2\pi}\frac{d\theta}{2\pi}\times C_{\lambda\mathbf{Q}} I_{qz} e^{\mp i\varphi}\sin\frac{\theta}{2}$$
$$[N_{\lambda\mathbf{Q}} D_{\varepsilon-\hbar\omega_{\lambda\mathbf{Q}}}(f_{\varepsilon-\hbar\omega_{\lambda\mathbf{Q}}} - f_\varepsilon) + N_{\lambda-\mathbf{Q}} D_{\varepsilon+\hbar\omega_{\lambda\mathbf{Q}}}(f_{\varepsilon+\hbar\omega_{\lambda\mathbf{Q}}} - f_\varepsilon)], \tag{6.3}$$

where f_ε is the energy distribution function of electrons reduced to the Fermi distribution in quasi-equilibrium conditions, θ is the scattering angle of electrons, $\omega_{\lambda\mathbf{Q}}$ and $N_{\lambda\mathbf{Q}}$ are the frequency and distribution function of phonons, respectively. The absolute value of the in-plane component of phonon wave vector, $\mathbf{q} = (q_x, q_y)$, in quasi-elastic approximation where phonon energies are much smaller than the Fermi energy, is given by $q = 2k_F\sin(\theta/2)$, while the direction of $\mathbf{q}$ is given by the polar angle φ, $\tan\varphi = q_y/q_x$.

The squared overlap integral I_{qz} is defined as $I_{qz} = |\int dz e^{iq_z z}F^2(z)|^2$, where $F(z)$ is the ground-state wave-function describing confinement of electrons in the quantum well. The function $C_{\lambda\mathbf{Q}}$ is the squared matrix element of the electron-phonon interaction potential in the bulk. The electron-phonon interaction occurs via deformation-potential and piezoelectric-potential mechanisms described by the interaction constants $\mathscr{D}$ and h_{14}, respectively. Considering the approximation of isotropic phonon spectrum, the longitudinal ($\lambda = l$) and transverse ($\lambda = t$) mode contributions are given by well-known (Zook, 1964) formulas

$$\begin{aligned} C_{l\mathbf{Q}} &= \frac{\hbar}{2\rho_M\omega_{l\mathbf{Q}}}[\mathscr{D}^2 Q^2 + 36(eh_{14})^2 q_x^2 q_y^2 q_z^2/Q^6], \\ C_{t\mathbf{Q}} &= \frac{2\hbar(eh_{14})^2}{\rho_M\omega_{t\mathbf{Q}}Q^4}[q_x^2 q_y^2 + q_x^2 q_z^2 + q_y^2 q_z^2 - 9q_x^2 q_y^2 q_z^2/Q^2], \end{aligned} \tag{6.4}$$

where ρ_M is the material density. The distribution function of the ballistic phonon can be approximated according to

$$N_{\lambda\mathbf{Q}} = N_{\omega\lambda\mathbf{Q}}\phi_{\mathbf{r}}(\varphi,\zeta), \tag{6.5}$$

where $N_{\omega\lambda\mathbf{Q}} = [\exp(\hbar\omega_{\lambda\mathbf{Q}}/k_B T_{ph}) - 1]^{-1}$ is the Planck distribution function and T_{ph} is the heater temperature. Since the phonon flux is different for different $\mathbf{r}$, the function $N_{\lambda\mathbf{Q}}$ depends on the coordinate **r** in the 2D plane. This dependence enters through the function $\phi_{\mathbf{r}}(\varphi,\zeta)$ describing distribution of the phonons over the polar angle ϕ and the inclination angle ζ which is defined according to $\cot\zeta = q_z/q$ in the point **r**. In the simplest approach, this function can be modeled as $\phi_{\mathbf{r}}(\varphi,\zeta) = 1$ within the region of angles $\triangle\varphi$ and $\triangle\zeta$ where the phonons from the heater can reach the point **r** and $\phi_{\mathbf{r}}(\varphi,\zeta) = 0$ outside this region. By substituting Eq. 6.5 into Eq. 6.3, the following result is obtained from Eqs. 6.1 to 6.3;

$$\mathbf{J}^{ph}(\mathbf{r}) = \int_0^{2\pi} d\varphi \int_0^{\pi} d\zeta \phi_{\mathbf{r}}(\varphi,\zeta)\mathbf{j}^{ph}(\varphi,\zeta), \tag{6.6}$$

where $\mathbf{j}^{ph}(\varphi,\zeta)$ is the differential current density induced by the phonons propagating at the fixed angles φ and ζ:

$$\begin{aligned}\begin{pmatrix} j_x^{ph}(\varphi,\zeta) \\ j_y^{ph}(\varphi,\zeta)\end{pmatrix} &= \frac{|e|k_F^2 m}{4\pi^3\hbar^4\sin^2\zeta(\omega_c^2+\nu_{tr}^2)}\sum_{\lambda=l,t}\int_0^{\pi}\frac{d\theta}{\pi} \\ &\times (1-\cos\theta)C_{\lambda\mathbf{Q}}I_{qz}N_{\omega_{\lambda\mathbf{Q}}}\int d\varepsilon D_\varepsilon \sum_{k=\pm1} kD_{\varepsilon-k\hbar\omega_{\lambda\mathbf{Q}}} \\ &\times (f_{\varepsilon-\hbar\omega_{\lambda\mathbf{Q}}} - f_\varepsilon)\begin{pmatrix} \nu_{tr}D_\varepsilon\cos\varphi - \omega_c\sin\varphi \\ \omega_c\cos\varphi + \nu_{tr}D_\varepsilon\sin\varphi\end{pmatrix},\end{aligned} \tag{6.7}$$

In the approximation of weak Landau quantization (overlapping Landau levels), when $D_\varepsilon \simeq 1 - 2d\cos(2\pi\varepsilon/\hbar\omega_c)$, where $d = \exp(-\pi/|\omega_c|\tau)$ is the dingle factor and τ is the quantum lifetime of electrons, the calculation of the integral over energy in Eq. 6.7 is considerably simplified. It is also assumed that $\hbar|\omega_c| \ll 2\pi^2 k_B T$, when the Shubnikov-de Haas oscillations are thermally suppressed. Moreover, it is taken into account that $\zeta \simeq \pi/2$ ($q_z \simeq 0$ and $I_{qz} \simeq 1$) and the approximation of isotropic electron-phonon scattering by averaging the piezoelectric-potential part of the functions C_{lQ} and C_{tq} from Eq. 6.4 over the polar angle φ, is also considered.

The current in each point of the 2D plane is a sum of the drag current $\mathbf{J}_{ph}(\mathbf{r})$ and the drift current $\hat{\sigma}\mathbf{E}(\mathbf{r})$. In the absence of external dc driving force , the local current is zero in the 2D plane , $\hat{\sigma}\mathbf{E}(\mathbf{r}) + \mathbf{J}_{ph}(\mathbf{r}) = 0$ and one can determine the local electric field as $\mathbf{E} = -\hat{\rho}\mathbf{J}_{ph}(\mathbf{r})$. The voltages between each two points in the 2D plane can be found by integrating this field . This leads to Eqs. 6.10 and 6.11 in the following section, where $F = F_l + F_t$ and $G = G_l + G_t$,

$$\begin{pmatrix} F_l \\ G_l \end{pmatrix} = \int_0^{\pi} \frac{d\theta}{\pi} \mathscr{E}_{\lambda\theta} N_{\omega\lambda\theta} \begin{pmatrix} 1 \\ \cos(2\pi\omega_{\lambda\theta}/\omega_c) \end{pmatrix}, \tag{6.8}$$

$\mathscr{E}_{t\theta} = m^2(eh_{14})^2(1-\cos\theta)/4\pi^2\hbar^2|e|\rho_M$, $\mathscr{E}_{l\theta} = (2\mathscr{D}k_F eh_{14})^2(1-\cos\theta)\mathscr{E}_{t\theta}$ and $\omega_{\lambda\theta} = 2s_\lambda k_F \sin(\theta/2)$. The sample-dependent coefficients γ_{ij}^L and γ_{ij}^T are given by the formula

$$\begin{pmatrix} \gamma_{ij}^L \\ \gamma_{ij}^T \end{pmatrix} = \int_0^{2\pi} d\varphi \int_i^j d\mathbf{l}. \begin{pmatrix} \mathbf{n}_\varphi \\ \tilde{\mathbf{n}}_\varphi \end{pmatrix} \int_0^{2\pi} d\xi \phi_{\mathbf{r}}(\varphi,\xi) \tag{6.9}$$

with $\mathbf{n}_\varphi = (\cos\varphi, \sin\varphi)$ and $\tilde{\mathbf{n}}_\varphi = (\sin\varphi, -\cos\varphi)$ and the integral $\int_i^j d\mathbf{l}...$ taken along a path inside the 2D gas area connecting the contacts i and j. The calculation of the lengths γ_{ij}^L and γ_{ij}^T, even within the simple model described above, is a complicated problem which is beyond the scope of the present work. Nevertheless, some rough estimates and symmetry relations can be presented.

Since the region of ζ contributing to the integral in Eq. 6.9 is narrow, both γ_{ij}^L and γ_{ij}^T are much smaller than the device size.

If the heater is placed symmetrically with respect to x axis, as shown in Fig. 6.11, one has $\gamma_{12}^L = \gamma_{34}^L = 0$, $\gamma_{23}^L = \gamma_{14}^L$ and $\gamma_{23}^T = -\gamma_{14}^T$. The last relation means that odd in B parts of V_{23} and V_{14} have different signs, which is actually observed in our experiments. The length γ_{12}^T is much larger than γ_{34}^T and γ_{23}^T is larger than γ_{23}^L. The fact that the observed V_{12} is not purely odd in B can be attributed to a slight asymmetry of the device, leading to nonzero γ_{21}^L.

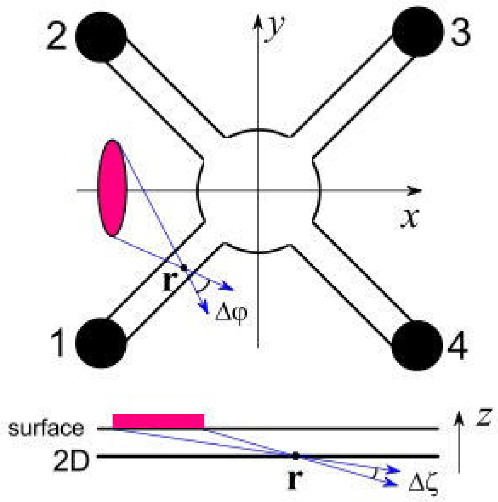

Figure 6.11: Picture of the ballistic phonon propagation (upper part - top view of the device, lower part schematic side view) indicating the regions of polar angles, $\triangle\varphi$, and inclination angles, $\triangle\varsigma$, within which the ballistic phonons from the heater (shown in red) can reach the point **r** in the 2D plane. The directions of phonon propagation are shown by blue arrows. The region $\triangle\varsigma$ is actually very narrow because the distance from the 2D plane to the surface is much smaller than the in-plane separation of the heater from any point in the 2D region. For the same reason, only the phonons propagating at the sliding angles (ς is only slightly larger than $\pi/2$) are essential.

6.4 Analysis & discussion

To get more insight into the physics of the observed phenomenon, here we apply the theoretical model developed in previous section to our experiment parameters. As mentioned in §.6.3, we believe that the drag in our experiment is mostly caused by high-energy ballistic phonons emitted from the heater in different directions , based on the following observations.

First, the voltage V_{43} measured far away from the heater is much smaller than the voltage V_{12}, so the proximity to the heater is essential for the phonon drag voltage (PDV) signal. Second, the amplitude of magneto-phonon oscillations of PDV in the absence of MW irradiation is much larger than expected for temperature T= 1.5 K in view of exponential suppression of back-scattering in the Bloch-Gruneisen regime, $k_B T \ll \hbar k_F s_\lambda$, so the effective phonon temperature T_{ph} must be considerably higher than T.

Using the basic formalism for calculation of thermo-electric response in quantizing magnetic field (Raichev, 2015) in application to the model, §.6.3 , one may represent the PDV between the contacts i and j in the form

$$V_{ij} = \gamma_{ij}^{L} E_L + \gamma_{ij}^{T} E_T, \tag{6.10}$$

where E_L and E_T are the electric fields developing as phonon-drag responses to a homogeneous unidirectional phonon flux in the directions along and perpendicular to this flux, respectively. The lengths γ_{ij}^{L} and γ_{ij}^{T} depend on the sample geometry.

The PDV are formed by mixing of the longitudinal (even in B) and transverse (odd in B)phonon-drag contributions described by the following expressions obtained in the regime of weak Landau quantization:

$$E_L = F + 2d^2 G, \qquad E_T = (2d^2 G - F\delta\rho_{xx}/\rho_0)/\omega_c \tau_{tr}, \tag{6.11}$$

where $\delta\rho_{xx} = \rho_{xx} - \rho_{xx}^{(0)}$, $\rho_{xx}^{(0)} = \rho_0(1+2d^2)$ is the resistivity in the absence of MW irradiation with $\rho_0 = m/e^2 n_s \tau_{tr}$, the dingle factor $\exp(-\pi/|\omega_c|\tau)$ and the quantum lifetime of electrons and transport time τ and τ_{tr}, respectively.

According to Eq. 6.8, it is clear that the quantity F does not depend on B while G is a function of B describing the magneto-phonon oscillations of PDV. In the absence of MW irradiation, $E_L \gg E_T$ in the relevant regime of classically strong magnetic fields, $|\omega_c|\tau_{tr} \gg 1$, so the dark PDV, V_{23}, is governed by E_L and is even in B. Under MW irradiation, E_T increases dramatically because of the large ratio $\delta\rho_{xx}/\rho_0$ and gives large, odd in B, contributions to all measured PDV.

The theoretical plots of E_L and E_T for our sample are shown in Fig. 6.12. The effective temperature of ballistic phonons, $T_{ph} \simeq 4$ K, is estimated from the amplitude of magneto-phonon oscillations in V_{23}.

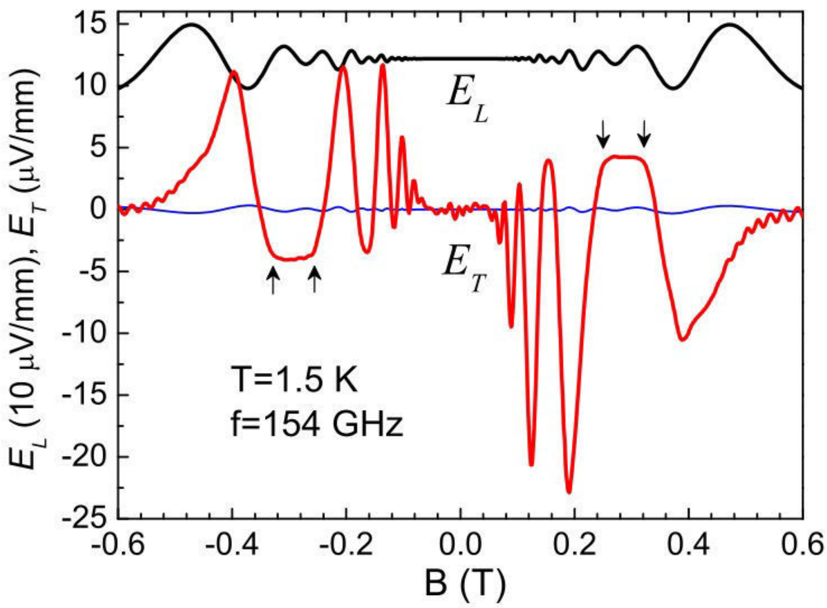

Figure 6.12: Calculated magnetic-field dependence of the fields E_L and E_T, the latter is plotted both with MW irradiation and without it (thin line). The function $\delta\rho_{xx}/\rho_0$ entering E_T is extracted from the experiment.

The magnetic-field dependence of E_T shows a strong oscillating enhancement under MW irradiation. To plot it, we substitute the experimental dependence of $\delta\rho_{xx}/\rho_0$ into Eq. 6.8. Similar results are obtained using theoretical dependence of $\delta\rho_{xx}/\rho_0$ (Dmitriev et al., 2005).

Our estimates of V_{23} and V_{12} based on the calculated E_L and E_T are in general agreement with experiment [note that in Eq. 6.10 one should take into account that both γ_{ij}^L and γ_{ij}^T are small compared to the device size (see §. 6.3)].

For numerical calculation of E_L and E_T we used the parameters of GaAs, $\rho_M = 5.317\ g/cm^3$, $\mathscr{D} = 7.17\ eV$, $h_{14} = 1.2\ V/nm$, $s_l = 5.14\ km/s$, $s_t = 3.04\ km/s$, as well as the electron density and mobility in our device. The quantum lifetime $\tau = 7\ ps$ was estimated from the ratio $\tau/\tau_{tr} \simeq 11$ which is typical for our samples fabricated according to the technology described in (Friedland et al., 1996).

Therefore, the theory confirms that the observed MW-induced changes of the PDV are caused by the effect of microwaves on the dissipative resistance.

In the ZRS regions, the experimental PDV shows a complex and diverse behavior that can not be explained within the theory given above. Our observations reveal abrupt changes of the drag voltages in obvious correlation with the ZRS in R_{xx} , see Fig. 6.9(b). Most often, the PDV, as a function of B, jumps at the beginning and at the end of the ZRS region, and more sharp features also appear within this region.

We attribute this behavior to a transition from the homogeneous transport picture to the domain structure specific for the ZRS, since such a transition is accompanied with switching between different distributions of the electric field in the 2D plane (Andreev , Aleiner and Millis, 2003; Dorozhkin et al., 2011). We emphasize that in our experiment this transition occurs in the unusual conditions, when external dc driving is absent. Nevertheless, this fact rests within the general theoretical picture of ZRS (Andreev , Aleiner and Millis, 2003), because the instability of the spatially homogeneous state is irrelevant to the presence of dc driving and requires only the negative conductivity created, for example, by MW irradiation. The resulting domains may carry electric currents, and the domain arrangement should provide zero currents through the contacts. The details of such domain structures are not clear and require further studies.

6.5 What we have learned

In summary, we observe MW-induced magneto-oscillations of the phonon-drag voltage in GaAs quantum wells, correlating with the behavior of electrical resistance. We have shown that the radiation creates the conditions which allow one to observe, without any external dc driving, an oscillating thermo-induced voltage proportional to the resistance and closely resembling a MIRO signal.

The effect is described in terms of the sensitivity of transverse drag voltage to the dissipative resistivity modified by microwaves. The behavior of phonon-drag voltage in the zero resistance regime can be viewed as a signature of current domain state. Such MW-induced thermo-electric phenomena may show up in other 2D systems. The magneto-thermo-electric measurements are therefore established as a tool to study the influence of MW radiation on the properties of 2D electrons and to gain complementary information about the MIRO and ZRS regime.

Chapter 7

Conclusion and outlook

In this research, we performed a systematic study of quantum transport phenomena in two dimensional electron systems with more than one sub-band occupied. The main objective of our studies have been obtaining new fundamental knowledge about the 2D electron transport properties in multilayer systems coupled via tunneling effects or interactions. In this way, we have tried to measure new effects in the oscillations, such as fluctuations in resonance magneto-inter-sub-band and magneto-phonon oscillations due to interaction with acoustic phonons. We have acquired new fundamental knowledge about the influence of the degree of freedom produced by the quantum coupling in tunneling magneto-transport phenomena.

This thesis presented the first experimental studies on nonlinear effect due to the AC current in multilayer electron systems, specifically triple quantum well of $GaAs$ at low magnetic fields. Since there are more than one sub-band occupied in these systems , magneto-resistance inter-subband oscillations which are a sign of coupling between the different layers, are observed with the picture that is more complex than the corresponding oscillations in bilayer systems formed in single and double quantum wells. Under the application of AC current the peculiar oscillation picture is strongly modified.

We explained the experimental results of our measurements based on a model by Dmitriev et al. (2005) generalized by Raichev and Vasko (2006) for multilayer systems. Moreover, we have studied the nonlinear effects of magneto-resistance around zero magnetic fields for different current and temperatures on sample of TQWs and WTQWs with mesoscopic Hall bar structures on them. We have observed the interesting picture of the huge negative magneto-resistance and studied the observed effect both in different current and temperatures. Our observations were in agreement with the observed effect reported by different groups, however, further investigations are necessary to understand the origin of this remarkable phenomenon.

Some existed theoretical model considering the electron-electron interactions and also scattering events within the Landau levels (Bockhorn et al., 2015, 2011) can be exploited for describing some feature. However, the main origin of negative magneto-resistance is an open research area and people in scientific community are interested to provide theoretical descriptions for the origin of the phenomena.

Within our thesis, we have also performed studies on nonlocal magneto-resistance of single and bilayer electron systems in the presence of microwave irradiation. Through our experiments in this part we shed more light on the properties of the edge states via nonlocal measurements and we have found evidences for stabilized edge-state current by microwave irradiation. We have compared the results of our experiments with a theoretical model based on modern nonlinear dynamics and it is demonstrated that the nonlinear resonance created by microwave field can be well described by the *Poincaré* surface of a section for electrons moving in the vicinity of the sample edge in case of our experiment. The results of the model extended to our specific sample parameters and experimental conditions. Our studied were more focused for the region where the microwave nonlocal response was observed. Within our investigations, we concluded that the contribution of the edge state effects in ZRS, are dominant or comparable with the bulk contribution.

Finally, in order to gain complementary information about the MIRO and ZRS regime, we have carried out magneto-thermo-electric measurements on two dimensional electron systems. Our observations of the phonon-drag voltage oscillations demonstrate the correlation of these

oscillations with the resistance oscillations under microwave irradiation in perpendicular magnetic field. Within the experiments we could observe for the first time the sharp features in the phonon-drag voltage, suggesting that current domains associated with ZRS states can exist in the absence of external dc driving. Within the theoretical estimation of phonon drag voltage , we described the observed effects in terms of the sensitivity of transverse drag voltage to the dissipative resistivity modified by microwaves.
Through our experimental data of PDV, a jump at the beginning and at the end of regions of ZRS have been observed beside the sharp features within the region which is attributed to the transition from the homogeneous transport picture to the domain structure specific for the ZRS. Note that in our experiment this transition occurs in the unusual conditions, when external dc driving is absent.

Through our studies we have demonstrated that the behavior of phonon-drag voltage in the zero resistance regime can be viewed as a signature of current domain state and we believe that similar MW-induced thermo-electric phenomena may show up in other 2D systems.

As far as fundamental experiments are concerned, the next consequent step is to study the response of thermodynamics properties of two dimensional electron systems like compressibility and entropy of these systems under microwave irradiation. These kind of measurements are difficult to be done comparing to conductance measurements, however , provide direct information about the the electronic density of states (DOS) and chemical potential of 2DES. For example, it is shown that quantum-capacitance measurements can provide significant insights into the ground state of low dimensional systems such as electron-electron interactions, quantum correlations, thermodynamic compressibility for 2D electron gas in GaAs heterostructures and many-body physics in carbon nano-tubes and graphene. In the presence of microwave irradiation these information can be used to shed more light on the origin of ZRS and the formation of current domains (Kuntsevich et al., 2015; Chepelianskii et al., 2015).

List of publications

Publications in international journals

2015

A. D. Levin, Z. S. Momtaz, G. M. Gusev, O. E. Raichev and A. K. Bakarov
"Microwave-Induced Magneto-Oscillations and Signatures of Zero-Resistance States in Phonon-Drag Voltage in Two-Dimensional Electron Systems"
Phys. Rev. Lett. **115**, 206801, (2015)

A. F. da Silva, A. Levine,Z.S. Momtaz, H. Boudinov and B. E. Sernelius,
"Magnetoresistance of doped silicon"
Phys. Rev. B **91**, 214414, (2015)

2014

A. D. Levin, Z. S. Momtaz, G. M. Gusev and A. K. Bakarov
"Microwave-induced nonlocal transport in a two-dimensional electron system"
Phys. Rev. B **89**, 161304, (2014)

Participation and presentation in international conferences and workshops

32nd International Conference on the Physics of Semiconductors (ICPS), Austin, Texas, USA, August 2014.

- "Microwave-induced nonlocal transport in a two-dimensional electron system", (*contributed poster presentation*)

21st International Conference on High Magnetic Fields in Semiconductor Physics (HMF-21), Panama city Beach, Florida, USA, August 2014.

- "Thermo-power magneto-intersubband oscillations in a double quantum wells", (*contributed poster presentation*)

20th International Conference on Electronic Properties of Two Dimensional Systems (EP2DS-20) and 16th International Conference on Modulated Semiconductor Structures (MSS-16), Wroclaw, Poland, July 2013.

- "Nonlinear transport and inverted magneto-intersubband oscillations in a triple quantum wells"(*contributed poster presentation*)

16th Brazilian Workshop on Semiconductor Physics (BWSP), Itirapina, SP, Brazil, May 2013.

- "Nonlinear Transport and Inverted magneto inter-subband oscillations in a Triple quantum wells" (*contributed oral presentation*)

Bibliography

Abanin, D. A., Novoselov, K. S., Zeitler, U., Lee, P. A., Geim, A. K. and Levitov, L. S., *Phys. Rev. Lett.* **98**, 196806 , (2007).

Ando, T. and Uryu, S., *J. Electron. Mater* **29**, 557, (2000).

Andreev, A. V., Aleiner, I. L. and Millis, A. J. , *Phys. Rev. Lett.* **91**, 56803 , (2003).

Andreev, I. V., Murav'ev, V. M., Kukushkin, I. V., Smet, J. H. , von Klitzing, K. and Umansky, V. , *JETP Lett.* **88**, 616, (2008).

Beenakker, C. W. J. and van Houten, H., *Phys. Rev. Lett.* **63**, 1857 , (1989).

Berk, Y., Kamenev, A., Palevski, A., Pfeiffer, L. N., and West, K. W., *Phys. Rev. B* **51**, 2604, (1995).

Bockhorn, L. , Barthold, P., Schuh, D., Wegscheider, W. and Haug, R. J., *Phys. Rev. B* **83**, 113301, (2011).

Bockhorn, L., Gornyi, I. V. , Schuh, D., Reichl, C. , Wegscheider, W. and Haug, R. J., *Phys. Rev. B* **90**, 165434, (2014).

Bockhorn, L., Inarrea, J. and Haug, R.J., *arXiv preprint arXiv:* **1504.00555**, (2015).

Buttiker, M , *Phys. Rev. Lett.* **57**, 1761 , (1986).

Buttiker, M., *Phys. Rev. B* **38**, 9375, (1988).

Bykov, A. A *JETP Lett.* **87**, 233, (2008).

Bykov, A. A., Zhang, J. Q., Vitkalov, S., Kalagin, A. K. and Bakarov, A. K, *Phys. Rev. B* **72**, 245307, (2005).

Cage, M. E., Dziuba, R. F., Field, B. F., Williams, E. R., Girvin, S. M., Gossard, A. C., Tsui, D. C. and Wagner, R. J., *Phys. Rev. Lett.* **51**, 1374 , (1983).

Cantrell, D. G. and Butcher, P. N., *J. Phys. C: Solid State Phys.* **20**, 1985, (1986).

Chepelianskii, A. D. and Shepelyansky, D. L. , *Phys. Rev. B* **80**, 241308 , (2009).

Chepelianskii, A. D., Watanabe, M., Nasyedkin, K., Kono, K. and Konstantinov, D., *Nat. commun.* **6**, (2015).

Chirikov, B. V.,*Phys. Rep.* **52**, 263 , (1979).

Chklovskii, D. B., Shklovskii, B. I., *Phys. Rev. B* **46**, 4026 , (1992).

Coleridge, P. T., Stone, R. and Fletcher, R., *Phys. Rev. B* **39**, 1120 , (1989).

Darwin, C. G., *Math. Proc. Cambridge Phil. Soc.* **27**, 86 , (1931).

Dai, Y., Du, R. R., Pfeifer, L. N. and West, K. W., *Phys. Rev. Lett.* **105**, 246802, (2010).

Davies, J. H , *The physics of low dimensional semiconductors,* Cambridge university press, (1998).

Dmitriev, I. A., Vavilov, M. G., Aleiner, I. L., Mirlin, A. D. and Polyakov, D. G , *Phys. Rev. B* **71**, 115316 , (2005).

Dmitriev, I. A., Dorozhkin, S. I., and Mirlin, A. D., *Phys. Rev. B* **80**, 125418, (2009).

Dolgopolov, V. T., Kravchenko, G. V. and Shaskin, A. A., *Solid State Commun.* **78**, 999 , (1991a).

Dolgopolov, V. T., Shashkin, A. A., Gusev, G. M., and Kvon, Z. D. , *JETP Lett.* **53**, 484 , (1991b).

Dolgopolov, V. T., Shashkin, A. A., Zhitenev, N. B., Dorozhkin, S. I. and Von Klitzing, K., *Phys.Rev. B* **46**, 12560 , (1992).

Dorozhkin, S. I., *JETP Lett.* **77**, 577 , (2003).

Dorozhkin, S. I., Pechenezhskiy, I. V., Pfeiffer, L. N. , West, K. W., Umansky, V., von Klitzing, K. and Smet, J. H. , *Phys. Rev. Lett.* **102**, 036602 , (2009).

Dorozhkin, S. I., Pfeiffer, L., West, K., von Klitzing, K. and Smet, J. H. , *Nat. Phys.* **7**, 336 , (2011).

Drude, P. , *Annalen der Physik* **308**, 369 , (1900).

Durst, A. C. , Sachdev, S. , Read, N. and Girvin, S. M., *Phys. Rev. Lett.* **91**, 086803, (2003).

Durst, A. C. and Steven Girvin, M., *science* **304**, 1752, (2004).

Enss, C. and Hunklinger, S. , *Low-TemperaturePhysics*, ISBN-10 3-540-23164-1 Springer Berlin Heidelberg New York , (2005).

Fletcher, R., Coleridge, P. T. and Feng, Y., *Phys. Rev. B* **52**, 2823 , (1995).

Fock, V., *Z. Phys.* **47**, 446 , (1928).

Fox, M., *Optical properties of solids* , Oxford University Press (2nd edition), (2010).

Freire, J. P., Egues, J. C *Braz. J. Phys.* **34**, 614 , (2004).

Friedland, K. J., Hey, R., Kostial, H., Klann, R. and Ploog, K. , *Phys. Rev. Lett.* **77**, 4616, (1996).

Girvin, S. M., Jonson, M. and Lee, P. A., *Phys. Rev. B* **26**, 1651, (1982).

Giuliani, G. F., Quinn, J. J., *Phys. Rev. B* **26**, 4421, (1982).

Halperin, B. I., *Phys. Rev. B* **25**, 2185 , (1982).

Hanna, C. B. and MacDonald, A. H., *Phys. Rev. B* **53**, 15981 , (1996).

Hatke, A. T., Zudov, M. A., Reno, J. L., Pfeifer, L. N., and West, K. W., *Phys. Rev. B* **85**, 081304, (2012).

Houghton, A., Senna, J. R., and Ying, S. C., *Phys. Rev. B* **25**, 2196, (1982).

Ihn, T., *Semiconductor Nanostructures: Quantum states and electronic transport,* Oxford University Press (2010).

Jeckelmann, B., Jeanneret, B., *Rep. Prog. Phys.* **64**, 1603 , (2001).

Kao, Y.C. and Lee, D.H., *Phys. Rev. B* **54**, 16903, (1996).

Kamerlingh Onnes, H. , *Comm. Phys. Lab. Univ. Leiden* **14**,(1911).

Kamerlingh Onnes, H. , *Comm. Phys. Lab. Univ. Leiden* **120**, 261, (1911).

Khodas, M. and Vavilov, M. G., *Phys. Rev. B* **78**, 245319 , (2008).

Kittel, C., *Quantum Theory of Solids,* John Willey & Sons , (1987).

Klitzing, K. V., *Seminaire Poincare* **2**,1 , (2004).

Klitzing, K. V. , Dorda, G. and Pepper, M. , *Phys. Rev. Lett.* **45**, 494 , (1980).

Kuntsevich, A. Y., Tupikov, Y. V., Pudalov, V. M. and Burmistrov, I. S. , *Nat. commun.* **6**, (2015).

Laikhtman, B. and Altshuler, E. L., *Ann. Phys.* **232**, 332 , (1994).

Landau, L., *Z. Phys.* **64**, 629 , (1930).

Laughlin, B., *Phys. Rev. B* **23**, 5632 , (1981).

Lei, X. L., *Appl. Phys. Lett.* **90**, 132119 , (2007).

Levin, A. D., Momtaz, Z. S., Gusev, G. M. and Bakarov, A. K., *Phys. Rev. B* **89**, 161304 , (2014).

Levin, A. D., Momtaz, Z. S., Gusev, G. M., Raichev, O. E. and Bakarov, A. K., *Phys. Rev. Lett.* **115**, 206801 , (2015).

Lifshits, I. M., Kosevich, A., *Sov. Phys. JETP* **2**, 636 , (1956).

Mamani, N. C., Magnetotransport em poços quânticos de AlGaAs/GaAs com diferentes formas de potencial, *PhD Thesis,* University of São Paulo, (2009).

Mamani, N. C., Gusev, G. M., Lamas, T. E., Bakarov, A. K. and Raichev, O. E., *Phys. Rev B* **77**, 205327, (2008).

Mamani, N. C., Gusev, G. M., Raichev, O. E., Lamas, T. E. and Bakarov, A. K. , *Phys. Rev. B* **80**, 075308 , (2009).

Mani, R. G., Smet,J. H., Klitzing, K. von, Narayanamurti, V., Johnson, W. B. and Umansky, V., *Nature* **420**, 646, (2002).

Marder, M. P., *Condensed Matter Physics*, John Willey & Sons, (2010).

McEuen, P. L., Szafer, A., Richter, C. A., Alphenaar, B. W., Jain, J. K., Stone, A. D., Wheeler, R. G. and Sacks, R. N., *Phys. Rev. Lett.* **64**, 2062 , (1990).

Mirlin, A. D., Polyakov, D. G., Evers, F. and Wolfle, P., *Phys. Rev. Lett.* **87**, 126805, (2001).

Mikhailov, S. A. and Savostianova, N. A., *Phys. Rev. B* **74**, 045325 , (2006).

Paalanen, M. A., Tsui, D. C., and Hwang,J. C. M., *Phys.Rev. Lett.* **51**, 2226, (1983).

Polyakov, D. G., Evers, F., Mirlin, A. D., and Wolfle, P., *Phys. Rev. B* **64**, 205306, (2001).

Pozar, D. M , *Microwave Engineering*, John Wiley and Sons, (1998).

Raichev, O. E., *Phys. Rev. B* **78**, 125304, (2008).

Raichev, O. E., *Phys. Rev. B* **91**, 235307, (2015).

Raichev, O. E. and Vasko, F. T., *Phys. Rev. B* **74**, 075309, (2006).

Roukes, M. L., Scherer, A., Allen Jr, S. J., Craighead, H. G., Ruthen, R. M., Beebe, E. D. and Harbison, J. P., *Phys. Rev. Lett.* **59**, 3011, (1987).

Ryzhii, V. I, *Sov. Phys. Solid State* **11**, 2078 , (1970).

Ryzhii, V. I., Suris, R. A. and Shchamkhalova, B. S., *Sov. Phys. Semicond.* **20**, 1299 , (1986).

Shubnikov, L. and de Haas, W. J., *Leiden Commun.* **207**, 3, (1930).

Smith, M. J. and Butcher, P. N., *J. Phys. C: Solid State Phys.* **20**, 1261, (1989).

Slutzky, M., EntinWohlman, O., Berk, Y., Palevski, A. and Shtrikman, H., *ibid.* **53**, 4065, (1996).

Stormer, H. L., Dingle, R., Gossard, A. C., Wiegmann, W., Sturge, M. D., *Solid State Commun.* **29**, 705 , (1979).

Suen, Y. W., Jo, J., Santos, M. B., Engel, L. W., Hwang, S. W. and Shayegan, M. , *Phys. Rev. B* **44**, 5947, (1991).

Thornton, T. J., Roukes, M. L., Scherer, A. and Van de Gaag, B. P., *Phys. Rev. Lett.* **63**, 2128, (1989).

Tsui,D. C., Stormer, H. L, Gossard, A. C., *Phys. Rev. B* **25**, 1405, (1982).

Tsui,D. C., Stormer, H. L, Gossard, A. C., *Phys. Rev. Lett.* **48**, 1559, (1983).

Van der Pauw, L. J., *Philips Tech. Rev.* **20**, 220, (1958).

Vavilov, M. G., Aleiner, I. L. and Glazman, L. I., *Phys. Rev. B* **76**, 115331, (2007)

Wiedmann, S., Gusev, G. M., Raichev, O. E., Lamas, T. E., Bakarov, A. K. and Portal, J. C., *Phys. Rev. B* **78**, 121301, (2008).

Wiedmann, S., Gusev, G. M., Raichev, O. E., Bakarov, A. K. and Portal, J. C., *Phys. Rev. Lett.* **105**, 026804, (2010).

Wiedmann, S, Novel transport properties in multi-layer electron systems *PhD Thesis*, University of Toulouse, (2010).

Wiedmann, S., Mamani, N. C., Gusev, G. M., Raichev, O. E., Bakarov, A. K. and Portal, J. C., *Phys. Rev. B* **80**, 245306, (2009).

Yang, C. L., Zhang, J., Du, R. R., Simmons, J. A. and Reno, J. L., *Phys. Rev. Lett.* **89**, 076801 , (2002).

Yoshioka, D., *The Quantum Hall Effect*, Springer, (2002).

Zaremba, E., *Phys. Rev. B* **45**, 14143 , (1992).

Zhang, W., Chiang, H. S., Zudov, M. A., Pfeiffer, L. N. and West, K. W., *Phys. Rev. B* **75**, 041304 , (2007).

Zhang, J., Lyo, S. K., Du, R. R., Simmons, J. A. and Reno, J. L., *Phys. Rev. Lett.* **92**, 156802 , (2004).

Zhang, J. Q., Vitkalov, S. and Bykov, A. A., *Phys. Rev. B* **80**, 045310 , (2009).

Zhang, J. Q., Vitkalov, S., Bykov, A. A., Kalagin, A. K. and Bakarov, A. K. *Phys. Rev. B* **75**, 081305 , (2007a).

Zhang, W., Chiang, H. S., Zudov, M. A., Pfeiffer, L. N. and West, K. W., *Phys. Rev. B* **75**, 041304, (2007b).

Zhang, J. Q., Vitkalov, S., Bykov, A. A., *Phys. Rev. B* **80**, 045310, (2009).

Zhang, J. Q., Vitkalov, S., Bykov, A. A., Kalagin, A. K. and Bakarov, A. K., *Phys. Rev. B* **75**, 081305, (2007).

Zhirov, O. V., Chepelianskii, A. D. and Shepelyansky, D. L., *Phys. Rev. B* **88**, 35410 , (2013).

Zook, J. D., *Phys. Rev.* **136**, 869 , (1964).

Zudov, M. A., Du, R. R., Simmons, J. A. and Reno, J. L., *arXiv preprint cond-mat/9711149*, (1997).

Zudov, M. A., Du, R. R. , Pfeiffer, L. N. and West, K. W., *Phys. Rev. Lett.* **90**, 046807 , (2003).

Zudov, M. A., Du, R. R., Simmons, J. A. and Reno, J. L., *Phys. Rev. B* **64**, 201311 , (2001).